

**Microfabrication of a microfluidic device for cell sorting: isolation of both circulating tumour cell (CTC) and giant cancer-associated macrophage-like cells (CAMLs)**



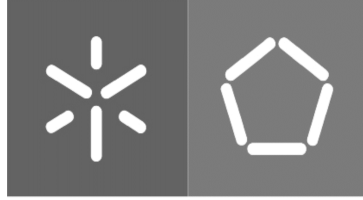
Luis Miguel Santos Dias

**Microfabrication of a microfluidic device for cell sorting: isolation of both circulating tumour cell (CTC) and giant cancer-associated macrophage-like cells (CAMLs)**

**Universidade do Minho**  
Escola de Engenharia







**Universidade do Minho**  
Escola de Engenharia

Luís Miguel Santos Dias

**Microfabrication of a microfluidic device for  
cell sorting: isolation of both circulating  
tumour cell (CTC) and giant cancer-  
associated macrophage-like cells (CAMLs)**

Dissertação de Mestrado

Mestrado Integrado em Engenharia Mecânica

Trabalho efetuado sob a orientação de:

**Professor Doutor Rui Alberto Lima**

**Doutora Diana Pinho**

dezembro de 2021

## **DIREITOS DE AUTOR E CONDIÇÕES DE UTILIZAÇÃO DO TRABALHO POR TERCEIROS**

Este é um trabalho académico que pode ser utilizado por terceiros desde que respeitadas as regras e boas práticas internacionalmente aceites, no que concerne aos direitos de autor e direitos conexos.

Assim, o presente trabalho pode ser utilizado nos termos previstos na licença indicada.

Caso o utilizador necessite de permissão para poder fazer um uso do trabalho em condições não previstas no licenciamento indicado, deverá contactar o autor, através do RepositóriUM da Universidade do Minho.



**Atribuição-NãoComercial-SemDerivações**

**CC BY-NC-ND**

<https://creativecommons.org/licenses/by-nc-nd/4.0/>

## **ACKNOWLEDGEMENTS**

This work results of the project InNPeC - Nano tools for rare giants: an innovative blood-based screening for prostate cancer (POCI-01-0145-FEDER-031442), funded by European Regional Development Found (ERDF) and by Fundação para Ciencia e Tecnologia (FCT).

First and foremost, I would like to thank my supervisors for their constant support throughout this project. To Diana Pinho, PhD, from the International Iberian Nanotechnology Laboratory (INL), for whom I have the uttermost gratitude, for receiving and welcoming me into her INL working group, for all the work and dedication that she put into the accompanying and revisioning my work and, most importantly, for her constant availability, generosity, kindness and preoccupation. To Professor Rui Lima, for giving me the chance to embrace this distinct project and for the willingness he demonstrated in assisting me and providing feedback. I would also like to leave a word of appreciation to all the professors and academic staff that contributed to my academic journey, in both Universidade do Minho and Universiteit Gent, as well as to the INL staff.

I would like to thank the ERASMUS+ program, for introducing me to a new world of possibilities, people and experiences, which played a pivotal role in moulding me into the person that I am today. Without the moments that I have experienced under its umbrella, life certainly would not be as colourful.

Moreover, I want to express my gratitude to my friends. To my ESCA friends, to my group of fellow Mechanical Engineering friends, to my lovely Savaanstraat 82, 9000 Gent family, to my Campo das Hortas folks, a huge, huge thank you for every remarkable moment that we have experienced together. And, especially, I would like to thank my ESN Minho family, as these two and half years with you have given me so much, and I just could not imagine a life without you all.

Finally, to my family, I cannot put into words how much I appreciate all that you have done for me. Luísa, Antonino and Lua, you are truly my lighthouse, always there to help me in the toughest moments and to cheer with me in the happiest occasions. Thank you for always believing in me and for your unconditional support no matter what. To the rest of my family, especially to Vó Prazeres and Vô Moisés, from the bottom of my heart, thank you for everything. And to you, Sofia, I am extremely grateful that we crossed paths, and for all the ensuing unforgettable moments that we have experienced together.

## **STATEMENT OF INTEGRITY**

I hereby declare having conducted this academic work with integrity. I confirm that I have not used plagiarism or any form of undue use of information or falsification of results along the process leading to its elaboration.

I further declare that I have fully acknowledged the Code of Ethical Conduct of the University of Minho.

## RESUMO

O cancro é a segunda maior causa de morte do mundo, tendo as mortes relacionadas com cancro vindo a aumentar. Entre os vários tipos de cancro, o cancro da próstata (PCa) é o segundo cancro masculino mais comum. Uma grande parte das mortes por cancro poderia ser evitada se os doentes fossem diagnosticados e tratados antes do desenvolvimento de metástases cancerígenas. A presença de células tumorais circulantes (CTC) e de macrófagos associados a tumores (CAML) na corrente sanguínea dos doentes com cancro é crucial para a deteção precoce da doença, já que estas desempenham um papel importante na disseminação do cancro. Assim, é importante desenvolver tecnologias capazes de detetar, quantificar e analisar estas células raras, pois isso permitiria um tratamento personalizado não invasivo, assim como um acompanhamento dos doentes em tempo real.

Portanto, este estudo centrou-se no desenvolvimento e otimização de um sistema microfluidico capaz de isolar eficazmente tanto as CTCs como as CAMLs do sangue periférico de pacientes com PCa. Assim sendo, foram concebidos dois dispositivos microfluidicos em espiral de *Dean Flow Fractionation* (DFF), tendo um dispositivo duas saídas e o outro quatro saídas. As forças inerciais inerentes que atuam sobre os microcanais permitem uma separação contínua das partículas de interesse, provocada pela diferença de tamanho entre as CTCs e CAMLs e o resto das células sanguíneas. As geometrias dos dispositivos foram desenvolvidas utilizando um *software* CAD, tendo estas sido otimizadas numericamente antes de os dispositivos serem fabricados. Ambos os dispositivos foram testados numérica e experimentalmente para assegurar que seriam capazes de isolar as células tumorais circulantes raras. O desempenho dos dispositivos foi experimentalmente otimizado utilizando amostras de suspensões celulares de linhas de células cancerosas da próstata (DU-145 e PC-3) e células gigantes geradas *in vitro*, tendo estas sido suspensas em sangue saudável e diluídas. Para os caudais ideais da amostra e do fluido *buffer* de 100 e 1000  $\mu\text{L}/\text{min}$ , respetivamente, a eficiência de isolamento do sistema microfluidico final foi de 85,28% para a linha de células PCa e 60,83% para as células gigantes geradas *in vitro*, tendo também sido alcançada uma elevada depleção do resto das células sanguíneas. Os resultados numéricos e experimentais foram semelhantes. Assim, os dispositivos microfluidicos propostos constituem um método viável para isolar células tumorais circulantes raras, potencialmente abrindo caminho para a deteção não-invasiva e para a monitorização do tratamento do cancro.

**PALAVRAS-CHAVE:** CAMLs, CTCs, Isolamento, Otimização, Cancro da Próstata

## ABSTRACT

Cancer is the world's second largest cause of death, with cancer-related fatalities growing over the years. Among the various cancer types, prostate cancer (PCa) is the second most common male cancer. However, a large portion of cancer fatalities might be avoided if patients were diagnosed and treated before the development of cancer metastases. The presence of rare circulating tumor cells (CTCs) and cancer-associated macrophage-like cells (CAMLs) in cancer patients' bloodstreams are crucial for early disease detection and treatment monitoring, as they play an important role in cancer dissemination, i.e. in the metastasis process. Thus, it is important to develop technologies capable of detecting, quantifying and analysing these rare cells, as that would allow for a personalized non-invasive treatment, as well as real time patient monitoring.

Therefore, this study focused on the development and optimization of a microfluidic system capable of efficiently isolate both CTCs and CAMLs from peripheral blood of PCa patients. As such, two spiral Dean Flow Fractionation (DFF) microfluidic devices were designed, a two-outlet and four-outlet device. The inherent inertial forces that act on the microchannels allow for a continuous, size-based separation of CTCs and CAMLs from blood. The devices geometries were developed using a CAD software, being numerically optimized prior to its fabrication. Both devices were tested numerically and experimentally to assure that they were capable of isolate rare circulating cancer-related cells. The devices' performances were experimentally optimized using samples of cell suspensions of prostate cancer cell lines (DU-145 and PC-3) and *in vitro* generated giant cells suspended in diluted healthy blood. For the optimal sample fluid and buffer fluid flow rates of 100 and 1000  $\mu\text{L}/\text{min}$ , respectively, the isolation efficiency of the final microfluidic system was 85.28% for the PCa cell line and 60.83% for the *in vitro* generated giant cells, while a high depletion of non-interest cells was achieved. The numerical and experimental results were similar. Thus, the proposed microfluidic devices constitute a viable method to isolate rare circulating cancer-related cells, potentially paving the way for personalized non-invasive detection and treatment monitoring of cancer.

**KEYWORDS:** CAMLs, CTCs, Isolation, Optimization, Prostate cancer



## TABLE OF CONTENTS

<b>Acknowledgements</b> .....	<b>iii</b>
<b>Resumo</b> .....	<b>v</b>
<b>Abstract</b> .....	<b>vi</b>
<b>Table of Contents</b> .....	<b>vii</b>
<b>List Of Figures</b> .....	<b>ix</b>
<b>List of Tables</b> .....	<b>xiv</b>
<b>Acronyms List</b> .....	<b>xv</b>
<b>Nomenclature</b> .....	<b>xvi</b>
<b>1. Introduction</b> .....	<b>1</b>
1.1 Motivation and Topic Overview .....	1
1.2 Objectives.....	3
1.3 Dissertation Outline .....	3
<b>2. Theoretical Background</b> .....	<b>5</b>
2.1 Blood Components and Flow Properties .....	5
2.1.1 Blood flow behaviour in microchannels.....	6
2.2 Prostate Cancer Circulating Biomarkers in the Bloodstream.....	8
2.3 Cell Separation Methods .....	12
2.3.1 Label-dependent and label-free cell separation techniques .....	13
2.3.2 Microfluidic lab-on-a-chip cell separation .....	16
2.4 Spiral Inertial Microfluidics .....	17
2.4.1 Classification of spiral devices .....	18
2.5 Flow characteristics .....	22
2.5.1 Fluid transport mechanics .....	26
2.6 Fabrication of DFF devices .....	31
2.6.1 Manufacturing Methods for PDMS-Based Microfluidics.....	33
<b>3. Numerical Methods</b> .....	<b>35</b>
3.1 Microfluidic Devices Geometries.....	35
3.1.1 Design of the DFF devices' geometries .....	36
3.2 Numerical Model .....	40
3.2.1 Initial conditions.....	41
3.2.2 Laminar flow.....	43
3.2.3 Particle tracing for fluid flow .....	44
3.2.4 Mesh properties.....	45
3.3 Numerical Simulations.....	46

3.4	Data Treatment .....	47
<b>4.</b>	<b>Experimental setup and procedures .....</b>	<b>49</b>
4.1	Microfluidic Devices Fabrication .....	49
4.2	Microfluidic Devices Priming and Tubing .....	52
4.3	Microfluidic Setup and Experimental Tests .....	52
4.4	Working Fluid Preparation and Handling.....	55
4.5	Sample Processing.....	57
4.6	Cell Counting Process and Data Treatment .....	59
<b>5.</b>	<b>Results and discussion .....</b>	<b>60</b>
5.2	Numerical Simulations.....	60
5.2.1	Numerical flow rates optimization.....	61
5.3	DFF Devices Fabrication and Working Principal .....	63
5.4	Experimental Flow Rates Optimization.....	65
<b>6.</b>	<b>Conclusions and Future Work .....</b>	<b>74</b>
6.1	Conclusions.....	74
6.2	Future Work .....	75
	<b>References .....</b>	<b>76</b>
	<b>Appendix A - Publications .....</b>	<b>87</b>
	<b>Appendix B – Poster submitted to the EuroNanoForum2021, 5-6 May 2021, Braga, Portugal .....</b>	<b>88</b>
	<b>Appendix C - Abstract of the poster submitted to the EuroNanoForum2021, 5-6 May 2021, Braga, Portugal .....</b>	<b>89</b>

## LIST OF FIGURES

Figure 2.1 - Blood constituents and conventional blood processing methods, adapted from [1].....	6
Figure 2.2 - Variation of shear stress with the shear rate for Newtonian and non-Newtonian fluids shear thickening and shear thinning, adapted from [21].....	7
Figure 2.3 - Representation of cancer cells (CTCs) being shed from a primary tumour into the peripheral bloodstream during metastasis [11]. .....	9
Figure 2.4 - Optical image (60× magnification) of an isolated CTC micro cluster (A), as well as the correspondent fluorescence image (B), including fluorescence images of the isolated CTC particles (C), with the sorted CTCs having been stained with stem cell marker CD133 (red), cytokeratin (green) and Hoechst (blue), adapted from [12]. .....	10
Figure 2.5 - Morphologies of different types of CAMLs (giant macrophages). From an origin standpoint, these can be classified as pancreatic cells (A, F, and G), breast cells (B, C, and D), prostate cells (E, H, and I) and typical WBCs (J); in regards to their morphology, they can be amorphous (A), oblong (B and G), spindle-shaped (C, F, and I), round (D), and tadpole-shaped (E and H). .....	12
Figure 2.6 - Examples of affinity-binding approaches procedures, as MACS uses magnetic beads coupled with antibodies that are introduced to a pool of cells and attached to the cells expressing the specific protein marker, while FACS makes use of antibodies labelled with fluorophores, adapted from [1].....	14
Figure 2.7 - Schematic representation of the separation principle for high-throughput CTCs separation using Dean Flow Fractionation (DFF): (A) inertial microfluidic design and (B) representation of the cells focusing considering the cross-section of the device, adapted from [12]. .....	21
Figure 2.8 - Bifurcation in a DFF device's microchannels, for which the continuity equation can be applied, adapted from [21].....	23
Figure 2.9 - Velocity profile in a fluid between two parallel plates demonstrating the no-slip condition, adapted from [21].....	24
Figure 2.10 - Schematic illustration of the wall induced lift force experienced by particles in inertial microfluidics, adapted from [42]. .....	27
Figure 2.11 - Schematic illustration of the shear gradient lift force experienced by particles in inertial microfluidics, adapted from [42]. .....	28
Figure 2.12 - Representation of a pair of Dean vortices within a spiral channel with a rectangular cross section, adapted from [42]. .....	29
Figure 2.13 - Schematic illustration of the shear gradient lift force experienced by particles in inertial microfluidics, adapted from [42]. .....	30

Figure 2.14 - Diagram depicting the relationship between several types of polymer materials and manufacturing methods for polymer-based microfluidics [13].	32
Figure 2.15 - Schematic illustration of the soft lithography procedure for the fabrication of PDMS microfluidic devices, which can be divided in two stages: (A) photolithography process and (B) soft lithography process, adapted from [22].	33
Figure 3.1 - Aspects, considerations and constraints that have to be examined in order to design an efficient passive microfluidic CTCs and CAMLs separation device, adapted from [19].	36
Figure 3.2 - Schematic representation of particle migration dynamics in a DFF device microchannels. Adapted from [49].	37
Figure 3.3 - Proposed DFF two-outlets (A) and four-outlets (B) devices for target cell isolation, which differentiate between themselves in the number of outlets and, consequently, on how the particles are isolated and categorized.	38
Figure 3.4 - Design in AutoCAD software of the proposed two-outlet DFF device with the respective lengths of inlets (A) and outlets (B).	40
Figure 3.5 - Design in <i>AutoCAD</i> software of the proposed four-outlet DFF device with the respective lengths of inlets (A) and outlets (B).	40
Figure 3.6 - 2D geometry imported to COMSOL of both two-outlet and four-outlet DFF devices that will be used to numerically study fluid flow behaviour and particles distribution.	42
Figure 3.7 - 3D model of the proposed four-outlet DFF device with a channel depth of 170 $\mu\text{m}$ , which was achieved by extruding the CAD geometry in the “Geometry” interface of COMSOL.	42
Figure 3.8 - Sidewalls’ parallel boundaries of the inner wall (in colour orange) and of the outer wall (in colour pink), which influence the wall induced lift force.	45
Figure 3.9 - Mesh configuration for the proposed four-outlet DFF device. Detailed view of the outlets region.	46
Figure 3.10 - Example of the velocity magnitude graphs that can be obtained by performing a stationary study in COMSOL using the proposed four-outlet DFF model.	47
Figure 3.11 - Example of the particle trajectories graphs that can be obtained by performing a time dependent study in COMSOL using the proposed four-outlet DFF model.	47
Figure 4.1 - Devices design being transferred to the wafer by photolithography.	50
Figure 4.2 - Microfluidic devices’ fabrication procedure: (I) PDMS mixture process, (II) PDMS casting over the Petri dish with the master mould and PDMS polymerization in the oven at 65 °C for two hours, (III)	

detachment of the PDMS replica from the Petri dish with the master mould, (IV) punching of inlet and outlet holes in the PDMS wafer, (V) bonding of the PDMS wafer and glass slide surfaces. ....	51
Figure 4.3 - Pumping of a filtered sample of Pluronic F-127 (Sigma Aldrich) at 1% (w/v) in PBS to the spiral chip at a flow rate of 250 $\mu$ L/min for around five minutes, in order to get rid of persisting air bubbles within the system and to guarantee that the device's channels are hydrophobic. ....	52
Figure 4.4 - Setup of the microfluidic system, with the syringes (B - buffer syringe, D - sample syringe) properly mounted on the syringe pumps (A and C), the tubing connected to the inlets and outlets of the biochip (E), and the sample collection conical tubes (F) set to receive the microchannels' outputs. ....	53
Figure 4.5 - Schematic representation of the experiments (A), as DU-145 and giant cells were suspended in diluted blood and run separately in the two-outlet and in the four-outlet devices, with the cells isolated in each outlet being counted under fluorescence microscope. ....	54
Figure 4.6 - Schematic representation of the experiments (B), as 50, 100, 1000 and 2000 DU-145 or/and giant cells suspended in diluted blood were run into both two-outlet and four-outlet devices, with an intermediate centrifugation stage, with the cells isolated in each outlet being counted under fluorescence microscope. ....	54
Figure 4.7 - Schematic representation of the experiments (C), as 100 PC-3 cells and giant cells suspended in diluted blood were run into both two-outlet and four-outlet devices, with an intermediate centrifugation stage, with the cells isolated in each outlet being counted under fluorescence microscope. ....	55
Figure 4.8 - For this study, a reliable sample consisted on a suspension of prostate cancer cell lines (B), <i>in vitro</i> generated giant cells (C) and healthy blood samples (A) was used, as their combination has characteristics that resemble those of a pathological sample. ....	55
Figure 4.9 - DU-145 cells (A) and PC-3 cells (B) observed via a microscope. Objective lens of 20x. ....	56
Figure 4.10 - Giant cells observed via an electronic inverted fluorescence microscope. Objective lens of 20x. ....	57
Figure 4.11 - Sample fluid consisting on a suspension of diluted healthy blood and a certain number of cancer cell lines suspension. ....	57
Figure 4.12 - 5 mL syringe containing the working fluid loaded into a syringe pump and connected to the biochip using tubing and a precision tip. ....	58
Figure 4.13 - Differentiated fluids collected in outlets 1 to 4 (from left to right, respectively) in one of the experimental runs performed with the four-outlet device. ....	58

Figure 4.14 - Parts of the cell counting process, namely the centrifugation of the collected fluid samples (A), the pellet containing the interest cancer cells (B), and the characterization and counting of the isolated cells using an electronic inverted fluorescence microscope (C)..... 59

Figure 5.1 - Average numerical isolation efficiency of cells > 20  $\mu\text{m}$  and depletion of cells < 20  $\mu\text{m}$  obtained for the two-outlet device model using different flow rates of sample/buffer ratio. .... 61

Figure 5.2 - Average numerical isolation efficiency of cells > 20  $\mu\text{m}$  and depletion of cells < 20  $\mu\text{m}$  obtained for the four-outlet device model using different flow rates of sample/buffer ratio..... 62

Figure 5.3 - Cells > 20  $\mu\text{m}$  (red and green, CAMLs and CTCs, respectively)  $\mu\text{m}$  isolated in the inner outlets of a four-outlet device after the execution of a numerical simulation on COMSOL using a flow rate ratio of 100/800  $\mu\text{L}/\text{min}$ ..... 62

Figure 5.4 - Velocity magnitude graphs obtained in COMSOL for the XY and YZ planes of the two-outlet device..... 63

Figure 5.5 - Velocity magnitude graphs obtained in COMSOL for the XY and YZ planes of the four-outlet device model. .... 63

Figure 5.6 - Images obtained from the recorded videos from the DFF devices. A to C for the two-outlet device (A) stabilized and well distributed flow of the sample; B and C the larger particles been focus to the outlet 2. D to F the four-outlet device, D the flow of stabilized and well distributed sample; E and F observation of the focusing of the larger particles to the inner outlet. Objective lens of 20x. .... 65

Figure 5.7 - Size distribution of (A) DU-145 cells (min = 11.008  $\mu\text{m}$ , max = 21.075  $\mu\text{m}$ , mean = 15.1974  $\mu\text{m}$ , SD = 2.954  $\mu\text{m}$ ), (B) giant cells (min = 23.766  $\mu\text{m}$ , max = 58.137  $\mu\text{m}$ , mean = 34.821  $\mu\text{m}$ , SD = 7.938  $\mu\text{m}$ ) and (C) PC-3 cells (min = 12.625  $\mu\text{m}$ , max = 22.093  $\mu\text{m}$ , mean = 15.1974  $\mu\text{m}$ , SD = 5.033  $\mu\text{m}$ )..... 66

Figure 5.8 - Average isolation efficiency of cells > 20  $\mu\text{m}$  (giant cells suspended into PBS) and depletion of cells < 20  $\mu\text{m}$  (DU-145 cells suspended into PBS) obtained for the two-outlet device using different flow rates of sample/buffer ratio. Results are displayed as Mean + SD of 3 independent experiments. 67

Figure 5.9 - Average isolation efficiency of cells > 20  $\mu\text{m}$  (giant cells suspended into PBS) and depletion of cells < 20  $\mu\text{m}$  (DU-145 cells suspended into PBS) obtained for the four-outlet device using different flow rates of sample/buffer ratio. Results are described as Mean + SD of 3 independent experiments. 68

Figure 5.10 - Average depletion of cells < 20  $\mu\text{m}$  of three different experiments, where 50, 100, 1000 and 2000 DU-145 cells were suspended in diluted blood (A) and average recovery rate of cells >20  $\mu\text{m}$  of three distinct experiments, where 50, 100, 1000 and 2000 giant cells were suspended in diluted blood. These were processed by the two-outlet device at flow rates of sample/buffer of 100/1000

$\mu\text{L}/\text{min}$ . The recovered outlet 2 fluid was then centrifuged, reduced to 1000  $\mu\text{L}$  and run in the four-outlet device with flow rates of sample/buffer of 100/1000  $\mu\text{L}/\text{min}$ . Results are described as Mean +SD of 3 independent experiments.....69

Figure 5.11 - Average recovery rate of cells  $> 20 \mu\text{m}$  and average depletion efficiency of cells  $< 20 \mu\text{m}$  of three different experiments, where 50, 100, 1000 and 2000 DU-145 cells and giant cells were suspended in diluted blood and processed by the two-outlet device at flow rates of sample/buffer of 100/1000  $\mu\text{L}/\text{min}$ . The recovered outlet 2 fluid was then centrifuged, reduced to 1000  $\mu\text{L}$  and run in the four-outlet device with flow rates of sample/buffer of 100/1000  $\mu\text{L}/\text{min}$ . Results are described as Mean +SD of 3 independent experiments. ....71

Figure 5.12 - Average recovery rate of cells  $> 20 \mu\text{m}$  (A) and average recovery rate of PC-3 and giant cells per outlet of the four-outlet device (B) of four different experiments, where 100 cells of both PC-3 cells and giant cells were suspended in diluted blood and processed by the two-outlet device at flow rates of sample/buffer of 100/1000  $\mu\text{L}/\text{min}$ . The recovered outlet 2 fluid was then centrifuged, reduced to 1000  $\mu\text{L}$  and run in the four-outlet device with flow rates of sample/buffer of 100/1000  $\mu\text{L}/\text{min}$ . Results are described as Mean +SD of 3 independent experiments.....72

Figure 5.13 - Average recovery of cells  $> 20 \mu\text{m}$  obtained for the combination of the two-outlet device model with the four-outlet device model device at flow rates of 100/1000  $\mu\text{L}/\text{min}$  for the sample and buffer, respectively.....73

## LIST OF TABLES

Table 2.1 - Comparison of various microfluidic passive separation techniques, adapted from [49].	17
Table 2.2 - Comparison of different spiral devices configuration and sorting, adapted from [49].	19
Table 3.1 - Defined dimensions for the main design features of the DFF microfluidic devices that will be used for numerical and experimental trials.	39
Table 3.2 - Parameters used in all the simulations performed within this study.	41
Table 3.3 – Mesh conditions for the four-outlet DFF model.	46
Table 5.1 - Comparison between the design features dimensions of the fabricated wafers and the PDMS devices depth of the proposed geometries defined on <i>AutoCAD</i> for both devices.	64



## ACRONYMS LIST

<b>CAD</b>	Computer-Aided Design
<b>CAMLs</b>	Cancer-Associated Macrophages Like Cells
<b>CFL</b>	Cell-Free Layer
<b>COMSOL</b>	<i>COMSOL Multiphysics.</i>
<b>CTCs</b>	Circulating Tumour Cells
<b>DC</b>	Dean Cycle
<b>DFF</b>	Dean Flow Fractionation
<b>EMT</b>	Epithelial-To-Mesenchymal Transition
<b>EpCAM</b>	Epithelial Cell Adhesion Molecule
<b>FACS</b>	Fluorescence-Activated Cell Sorting
<b>FDA</b>	US Food and Drug Administration
<b>HiDFF</b>	High-Resolution Dean Flow Fractionation
<b>LOC</b>	Lab-On-A-Chip
<b>MACS</b>	Magnetic-Activated Cell Sorting
<b>PBS</b>	Phosphate Buffered Saline
<b>PCa</b>	Prostate cancer
<b>PDMS</b>	Polydimethylsiloxane
<b>PSA</b>	Prostate-specific Antigen
<b>RBCs</b>	Red Blood Cells
<b>SD</b>	Standard Deviation
<b>WBCs</b>	White Blood Cells
<b>WHO</b>	World Health Organization
<b>UV</b>	Ultraviolet

## NOMENCLATURE

Symbol	Designation	Unit of Measurement
$A$	Area of the fluid surface	$m^2$
$A_{CS}$	Cross-sectional area	$m^2$
$A_1$	Area across which the fluid enters the control volume	$m^2$
$A_2$	Area across which the fluid leaves the control volume	$m^2$
$a$	Particle Size	$m$
$De$	Dean number	-
$D_h$	Characteristic linear dimension of the system	$m$
$F$	External force	$N$
$F_d$	Dean drag force	$N$
$F_l$	Inertial lift force	$N$
$F_{SL}$	Shear gradient lift force	$N$
$F_{WL}$	Wall induced lift force	$N$
$F_{\Omega}$	Rotational-induced lift force	$N$
$f$	Vector field of external body forces imparting on fluid elements	$N$
$h$	Microchannel height	$m$
$L$	Film thickness	$m$
$L_{dc}$	Complete Dean cycle migration length	
$P$	Fluid pressure	$Pa$
$P_{wet}$	Perimeter that is in contact with the liquid in a microchannel	$m$
$p$	Fluid pressure field	$Pa$
$Q$	Volume flow rate	$m^3/s$
$Q_1$	Volume flow rate that traverses the control volume at point 1	$m^3/s$
$Q_2$	Volume flow rate that traverses the control volume at point 2	$m^3/s$
$Q_3$	Volume flow rate that traverses the control volume at point 3	$m^3/s$

<b>Symbol</b>	<b>Designation</b>	<b>Unit of Measurement</b>
$R$	Average radius of curvature of the channel	m
$R_f$	Ratio of shear gradient lift force to Dean drag force	-
$Re$	Reynolds number	-
$Re_c$	Channel Reynolds number	-
$Re_p$	Particle Reynolds number	-
$w$	Microchannel width	m
$U_{De}$	Average transverse Dean velocity	m/s
$U_m$	Maximum velocity of the fluid flow	m/s
$v$	Velocity of the moving plate	m/s
$v_1$	Average velocity of the fluid across $A_1$	m/s
$v_2$	Average velocity of the fluid across $A_2$	m/s
$x$	Particle position within the channel	-
$\delta$	Curvature ratio	-
$\Delta x$	Displacement of the fluid at the moving plate	m
$\rho$	Fluid density	kg/m <sup>3</sup>
$\rho_1$	Fluid density at point 1	kg/m <sup>3</sup>
$\rho_2$	Fluid density at point 2	kg/m <sup>3</sup>
$\tau$	Shear stress	N/m <sup>2</sup>
$\mu$	Fluid dynamic viscosity	Pa.s
$\mu_{sp}$	Fluid apparent viscosity	Pa.s
$\gamma$	Shear strain	s <sup>-1</sup>

## 1. INTRODUCTION

In order to contextualize this study in the scientific community, this chapter introduces the current work by describing its motivation and a summary of the respective topic. The objectives are then outlined, followed by a description of the document's structure.

### 1.1 Motivation and Topic Overview

Blood is fundamental for life, as it is responsible to deliver the nutrients and oxygen to the cells, while also being tasked with transporting metabolic waste products away from those same cells. It is also, the most valuable biospecimens and research resource used in medicine [1].

While water makes up the bulk of blood, it is also multidimensional, including a diverse range of cells, like red blood cells (RBCs), white blood cells (WBCs) and platelets, and molecules. There also exist other groups of cells, the rare cells, within the circulatory system that are extremely clinically relevant. For example, in a case of a solid tumour, circulating cancer-related biomarkers, such as Circulating Tumour Cells (CTCs) that originate from the tumour or circulating stromal cells the Cancer-associated Macrophage-Like cells (CAMLs), can be seen and detected in the circulating blood, as well as other cancer-related cells [1].

Cancer is the world's second largest cause of death, with cancer-related fatalities being expected to exceed 13 million annually by 2030 [2]. Among the various cancer diseases, prostate cancer (PCa) is the most frequent non-cutaneous male cancer and the second most prevalent cancer, being the fifth greatest cause of cancer-related fatalities globally [3]. It is a multifactorial disease in which genetics, environmental factors, age, family health history, and ethnicity may combine to boost tumour growth, and its diagnostic tends to occur at an average age of 72-74 years, with 85 % of patients diagnosed at the age of 65 or older [4], [5].

The identification of prostate cancer-specific biomarkers in body fluids is the most often applied technique used for PCa diagnosis and to eliminate the need of biopsies. However, due to prostate-specific antigen (PSA) techniques' lack of specificity, its use can also lead to episodes of over-diagnosis and overtreatment of a low risk PCa [6]. Besides that, tumour biopsies, which are invasive and dependent on tumour heterogeneity and genetic alterations, leads to clinical decisions based on historical biopsies and not on real-time patient monitoring, leaving a chance for the tumour to spread, while also not offering proper conditions for a personalized disease treatment in accordance to the patient's specific needs [7].

The World Health Organization (WHO) estimates that at least 30% of the above-mentioned fatalities might be avoided if patients were diagnosed and treated before the development of cancer metastases, which are thought to be responsible for 90% of cancer-related deaths [8]. In the case of PCa-related fatalities, these are generally caused by the onset of metastatic illness, with 80 % of cases mostly localized in the bones [9]. The cancer cells that are shed from primary tumours into the peripheral bloodstream during metastasis are known as circulating tumour cells (CTCs) [10]. They are very rare in number (around 1-10 CTCs/billion of blood cells), thus its potential effective isolation from blood for downstream molecular and cellular analysis has attracted researchers' interest for both improving cancer prognosis and better understanding the metastatic process [10]. Cancer-associated macrophages-like cells (CAMLs), other uncommon cell population recently detected in the peripheral circulation, have also been linked to interacting with the CTC population, which also suggests a role in cancer cell dissemination [11].

With this in mind, liquid biopsy has recently emerged as a potentially viable non-invasive approach for molecular profiling of circulating cancer-related cells (such as CTCs and CAMLs) in different biological fluids, with the goal of enabling early cancer detection and real-time patient monitoring [7]. Circulating cancer related-cells detection, quantification and molecular analysis can provide powerful insights in individual prognosis, and personalized treatment by taking in account the number of cells in the bloodstream.

Microfluidic technologies have demonstrated unique benefits in functional analytical procedures, in particular for cell separation [12]. Since microfluidic rare cells isolation allows for single-cell analysis, it is possible to obtain more specific and accurate information about certain cellular processes, making this a viable approach for studies of cellular signal transmission, physiological pathology, and early diagnosis of serious diseases; as such, microfluidics has become a significant driving force for discovery and advancement in pharmacology, pathology, and cell biology [13].

Thus, microfluidics outperforms many approaches in terms of early diagnostic procedures, and polymer-based microfluidics have the potential to make very complex procedures such as liquid biopsy and early cancer detection something rather efficient, simple and inexpensive. With this in mind, the intention and motivation of this study is to develop and analysed if a microfluidic isolation system would constitute a viable solution for early detection and diagnosis of PCa, while also being commercially available and easy to use.

## 1.2 Objectives

The main objective of this work is to design microfluidic devices based in passive separation methods (size based) that are capable to efficiently isolate and detect a desired population of rare blood cells, namely the CTCs and CAMLs, from the blood of prostate cancer patients, which is the most common neoplasia among men.

At first, the fabricated devices will be tested and validated by numerical simulations and experimental tests. The simulations will be carried out by using the COMSOL software and corroborated with experimental tests. Control samples, such as healthy human blood and suspensions of prostate cancer cell lines, will be used, in order to optimize several parameters (flow rates, sample dilution, devices geometry) for an efficient cell isolation from pathological samples.

The work has been developed using state-of-the-art facilities and techniques for soft-lithography, microfluidic techniques and high-speed video microscope system, with this dissertation having the following aims to:

- Design and optimization of size based microfluidic devices for rare cells isolation;
- Numerical simulations to optimize the working flow rates of the developed microfluidic devices;
- Experimental tests with healthy blood samples and suspension of prostate cancer cell lines;
- Development of a microfluidic system composed of microfluidic devices in sequence in order to improve the rare cell isolation with high purity;
- Validation of the final microfluidic system with prostate blood analogue samples, i.e., healthy blood with suspension of prostate cancer cells (CTCs) and *in vitro* generated giant cells (CAMLs).

## 1.3 Dissertation Outline

The dissertation is divided into six sections, one of which is this introduction, which contains the motivation for the study as well as an overview of the subject. The objectives of the project are also listed in this chapter.

The second chapter contains a literature review on the essential theoretical contents that are required to develop and test the proposed microfluidic devices, as well as to comprehend the results acquired at the end of this study. The literature review on blood components and flow properties, prostate cancer circulating biomarkers in the bloodstream, cell-separation methods, and spiral inertial microfluidics working principal are the four primary subtopics of this chapter.

The numerical methods employed in this dissertation are discussed in the third chapter. The microfluidic devices geometries are described, and the numerical models and simulations are also discussed.

In the fourth chapter the experimental setup and procedures are thoroughly presented, as the microfluidic devices fabrication, microfluidic devices priming and tubing, microfluidic setup and experimental tests, working fluid preparation and handling, sample processing, cell counting process and data treatment stages are detailed.

The findings of the numerical simulations as well as the experimental tests are presented in the fifth chapter. The results are analysed and discussed throughout this section.

The key conclusions drawn from this thesis are provided in the last chapter, along with suggestions for further research in this subject.

## 2. THEORETICAL BACKGROUND

This chapter provides a theoretical backdrop from the concepts required to understand the blood particles motion and separation phenomena, which will allow for a critical discussion of the outcomes of this work. It is separated into three sections, one dealing with the theory behind blood components and its flow properties, followed by a contextualization about prostate cancer circulating biomarkers in the bloodstream. A detailing section of cell separation methods, and finally a section about spiral inertial microfluidics.

### 2.1 Blood Components and Flow Properties

Blood is a non-homogeneous fluid made of cells, proteins, and ions suspended in a viscous fluid called plasma, with red blood cells (RBCs), white blood cells (WBCs), and platelets constituting the cell suspension, as can be observed in Figure 2.1. These cells make about 46% of whole blood volume (with RBCs being in majority, about 45% of the total volume), and have different profiles and sizes, as RBCs have a biconcave shape (7-8  $\mu\text{m}$ ), WBCs have a roughly spherical configuration (7-12  $\mu\text{m}$ ) and platelets are either round or oval (1-4  $\mu\text{m}$ ) [14]. By flowing via a variety of complicated circulatory system networks, besides being tasked with carrying the aforementioned particles throughout the human body, blood also ensures the supply of oxygen and eliminates metabolic waste [15]. Given its components, blood ends up playing an essential role in body homeostatic regulation, while at the same time providing a valuable source of useful biomarkers for clinical diagnosis [1]. It can be found examples of these biomarkers in the detection of multiple diseases such as leukaemia or anaemia where platelet concentration is often used as a biomarker when concentrations outside of its usual range (between  $1.5 \times 10^5$  and  $4.5 \times 10^5$  cells/ $\mu\text{L}$ ) are found [16]; or when WBCs aren't present in its normal range of concentration values (between  $4 \times 10^3$  and  $11 \times 10^3$  cells /L), then their important function of eliciting immunological responses to foreign pathogens in order to prevent and combat infections might be affected [16].



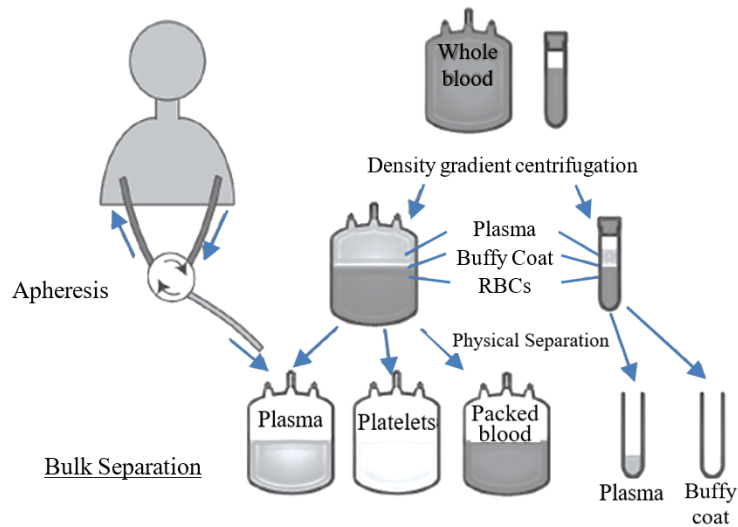


Figure 2.1 - Blood constituents and conventional blood processing methods, adapted from [1].

There has been a substantial growth of interest in developing microdevices that replicate the microcirculatory system in order to study and modulate biochemical and biomechanical blood cell behaviour *in vitro*. With the purpose of fabricating these sorts of clinically-relevant devices it is crucial to take into consideration some technical concepts of biofluids.

### 2.1.1 Blood flow behaviour in microchannels

The human circulatory system consists of a complex network of blood vessels that interact between each other in order to transport blood. At the microscale level, the rich and intricate interactions between blood cells, blood plasma, and confining blood arteries enable the development of distinct blood flow properties [1].

Blood circulation is caused by a pressure gradient that can be verified inside the blood vessels, with this pressure decreasing as blood travels away from the heart. However, this constitutes just a fraction of the blood circulation phenomena that for years researchers have been studying. In terms of composition and flow behaviour in microvessels, there still many things to figure out, such as the flow behaviour of blood with high hematocrit (Hct) [17]. Blood has several unique features, behaving as a single-phase homogeneous fluid or a multi-phase nonhomogeneous fluid depending on the diameter of the channel in which it flows [14].

In vessels with large diameters blood may be considered of as homogenous and handled as a single-phase fluid, and their flow analysis can be conducted adequately based on this assumption. However, in vessels with a reduced diameter ( $< 100 \mu\text{m}$ ), blood begins to display multi-phase, non-

homogeneous, and non-Newtonian properties, such as the local apparent viscosity (i.e., viscosity dependent on the local shear stress), with this being mostly attributable to the RBCs' deformable nature [17], [18].

Plasma, which by itself is blood without the presence of cells, might be regarded as a Newtonian fluid (exhibiting a viscosity in the range of 1.1 cP–1.35 cP at 37 °C) but, with the increase of cellular components, its non-Newtonian behaviour became more evident [19]. The precise value of a blood sample apparent viscosity ( $\mu_{ap}$ ) is determined by a number of variables, including hematocrit, plasma viscosity, RBC aggregation, and RBC mechanical characteristics, while also strongly depending on the shear rate (viscosity values range from 100 cP at a low shear rate of 0.1 s<sup>-1</sup> to 4–5 cP at high shear rates of 100 to 200 s<sup>-1</sup> at 37 °C, which means that blood acts as a shear thinning fluid), as demonstrated in Figure 2.2 [19], [20].

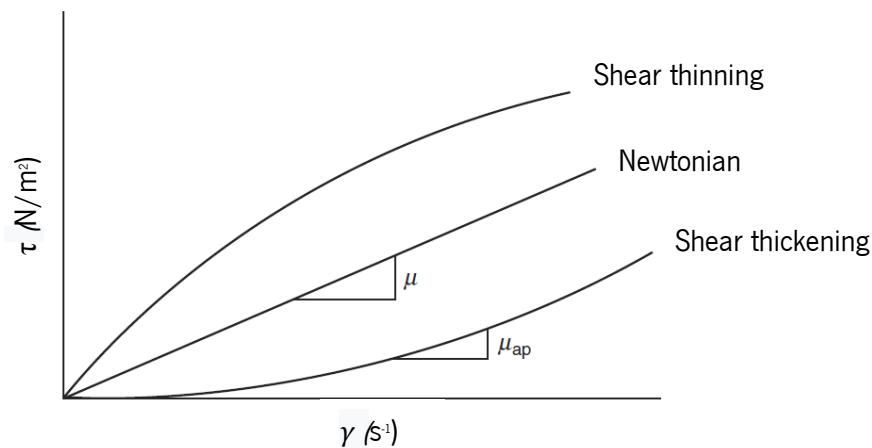


Figure 2.2 - Variation of shear stress with the shear rate for Newtonian and non-Newtonian fluids shear thickening and shear thinning, adapted from [21].

The presence in blood of RBCs, its concentration and structure deeply influence the rheological behaviour of blood [14]. They have a unique structure and due to its deformable nature, RBCs can pass through narrow vessels that are significantly smaller than their size [14], [17]. While circulating in microchannels such as blood vessels, RBCs have a propensity to move towards the channel axis, and as a result it is possible to verify an increase in cell concentration in the centre of the microchannel, while also leaving a zone devoid of cells near its side walls, designated as the cell-free layer (CFL) [21]. This axial migration of cells occurs because of various reasons, namely due to the deformable nature of the RBCs and to the occurrence of high-shear zones near to the channel's wall, as this results in an increase of velocity of RBCs compared to that of plasma [21]. However, it should also be of note that the high

deformability of RBCs also makes it tougher to achieve a mathematical model that describes correctly the cells mechanics, thanks to its high degree of properties variations [17].

Cell concentration, deformability, vessel diameter, cell aggregation, and flow rate all influence the thickness of the cell-free layer, as it decreases with an increase in tube diameter and with an increase in hematocrit level, while an increment in flow rate results in a thicker CFL at the microchannel periphery [22]. Lastly, the effect that cell aggregation on the CFL thickness is rather intricate, since the cell-free layer, as it is less viscous, ends up acting like a lubrication zone, while the RBCs aggregated core has a high viscosity, which means these wind up counteracting each other [23].

Besides cells trajectories, understanding the velocity profile of blood flow in microchannels or micro passageways is another key issue. According to some studies, the velocity profile for low blood hematocrit can be deemed parabolic, with its behaviour following Poiseuille's law, being dependent on factors such as hematocrit level, shear rate, flow rate, aggregation, and the diluting medium, as all of these affect the exact velocity profile characteristics [14], [24]. For example, RBCs flow behaviour is markedly different in a high hematocrit environment, according to some studies [25]. When these conditions occur, blood flow can lead to episodes of cell crowding, which results in erratic displacements owing to constant contact of cells with their neighbouring cells. For high hematocrit levels, measurements reveal a non-parabolic velocity profile with bluntness at the centre, adding even more complexity to the process of comprehending the blood flow phenomena [17].

There is still a gap in the scientific community to understanding of RBC flow behaviour, which has been a constant hindrance in the development of a device capable of separating 100 % plasma from undiluted blood.

## **2.2 Prostate Cancer Circulating Biomarkers in the Bloodstream**

Adenocarcinoma is the most common type of prostate cancer (PCa). It is possible to divide it into subtypes according to its cell of origin, with the acini of the prostatic ducts being the most common location for development of malignant illness in the prostate (about 95 % of cases). This development from healthy prostate to invasive carcinoma occurs due to a series of genetic and epigenetic alterations, and it is possible to observe three distinct development stages, namely proliferative inflammatory atrophy, low-grade prostatic intraepithelial neoplasia and high-grade prostatic intraepithelial neoplasia [5].

Because of its high phenotypic variation, sluggish growth behaviour, and lack of symptoms in the early stages, PCa is difficult to identify and treat and, as a result, a large percentage of men with localized PCa do not experience symptoms as a clear product of the disease itself [7]. Those who have it mainly

suffer from lower urinary tract symptoms, including urine frequency, urgency, reduced stream force, and nocturia, as well as other ailments such as back discomfort, leg inflammation, peripheral neurological difficulties, and erectile dysfunction [8], [9]. The existence and prevalence of circulating tumour cells (CTCs) in the bloodstream of patients with epithelial cancers (carcinomas), such as prostate cancer, is an essential intermediate phase in cancer metastasis that offers critical information about disease stage and potential treatment procedures [26].

Metastasis occurs when cancer cells spread from where they initially developed to another section of the body breaking away from the original (primary) tumour, moving via the blood or lymph system, and forming a new tumour in other organs or tissues of the body in a process known as metastasis [27]. It is also of note that the metastatic tumour is the same type of cancer as the primary tumour [27]. Cell migration, local invasion, intravasation of tumour cells into the circulation, dissemination, arrest at secondary and primary locations, extravasation into a distant site, and ultimately the development of clinically evident metastasis are all processes of the metastatic disease. The epithelial-to-mesenchymal transition (EMT), during which epithelial cells intercellular adhesion is shed and they gain a phenotype that is both more invasive and more mobile, is required for metastatic colonization; once this occurs, tumour cells then enter the circulatory system as single cells or clusters, spread throughout the body, and infect distant organs [9]. The cancer cells that are shed from primary tumours into the peripheral bloodstream during metastasis, as illustrated in Figure 2.3, are known as circulating tumour cells (CTCs) [11].

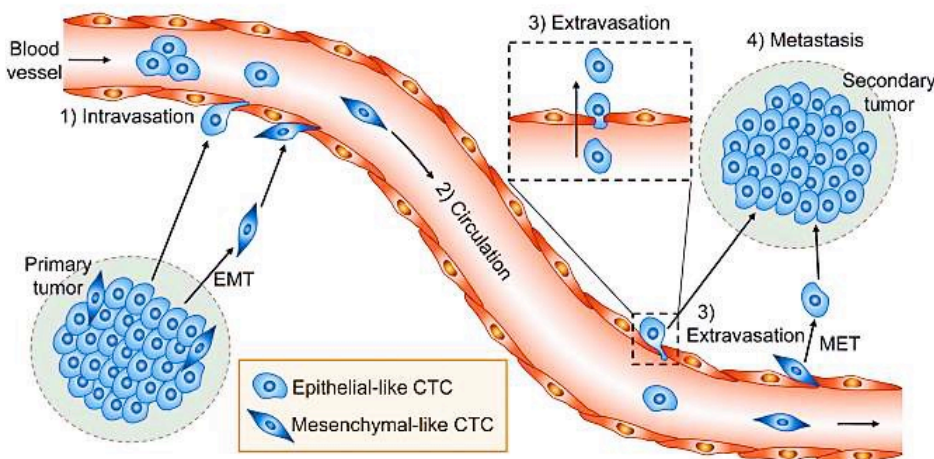


Figure 2.3 - Representation of cancer cells (CTCs) being shed from a primary tumour into the peripheral bloodstream during metastasis [11].

In the bloodstream CTCs are subjected to shear stress, the innate immune system, and oxidative damage in the circulation, which causes them to associate with platelets to defend themselves [28]. Cells are then converted back to an epithelial state when these are exposed to a specific signal, a process known as mesenchymal-to-epithelial transition (MET) [9]. As a result, CTCs begin to acquire resistance to both the immune system and the tissue's defence responses, and from then on there can either occur cell death, entering in a latent state as single cells or micro metastases (once these cells emerge from their dormant condition, they resume their development by conquering the local tissue's microenvironment), or colony formation through continuous multiplication [29].

CTCs in bloodstream usually have a round, spherical morphology with a well-defined nucleus, but their dimensions depend on tumour type and can be very variable across individuals [12]. Generally, they range from 12 to 25  $\mu\text{m}$  of diameter, but there can even be particles with diameters up to 50  $\mu\text{m}$  [12]. In Figure 2.4 it's possible to observe optical images of an isolated CTC micro cluster.

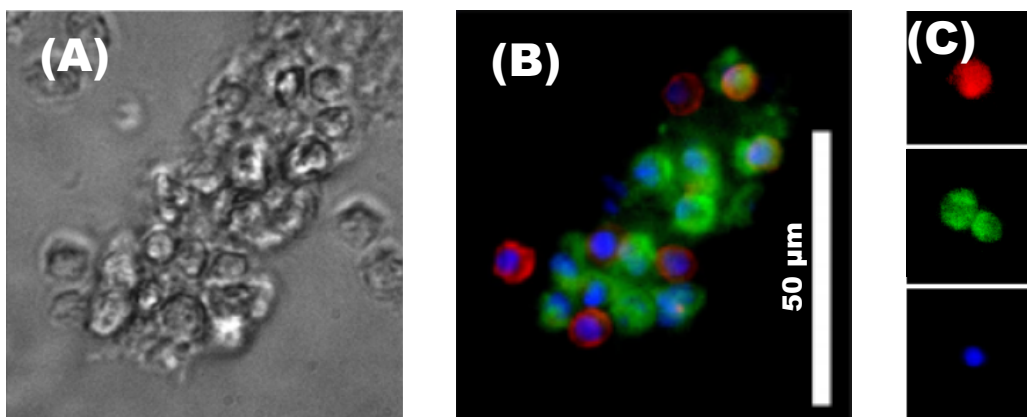


Figure 2.4 - Optical image (60 $\times$  magnification) of an isolated CTC micro cluster (A), as well as the correspondent fluorescence image (B), including fluorescence images of the isolated CTC particles (C), with the sorted CTCs having been stained with stem cell marker CD133 (red), cytokeratin (green) and Hoechst (blue), adapted from [12].

CTC molecular expression (phenotypic and genetic characterization of these rare cells) can be utilized as surrogate biomarkers to provide crucial insight for classifying disease phenotypic, which can contribute for early cancer detection, diagnostic and monitoring cell; these surface biomarkers can be assessed using immunofluorescence microscopy [26]. The identification of prostate cancer-specific biomarkers in body fluids is the most often applied technique used for PCa diagnosis and to eliminate the need of biopsies, with only three tumour markers being cleared by the US Food and Drug Administration (FDA) for routine practice in patient care, namely Prostate-Specific Antigen (PSA), Prostate

Health Index (PHI) and Prostate Cancer Antigen 3 (PCA3) and more recently the CTCs counting for disease stratification and treatment monitoring [6].

However, due to the CTCs' heterogeneity, accurate identification of CTCs has some challenges, since there is no uniform and universal biomarker that can be used to identify them, while the limited sensitivity of the available techniques to enumerate them also adds to poor characterisation and, as a consequence, the use of CTCs biomarkers can lead to episodes of over-diagnosis and overtreatment of a low risk PCa [6]. For example, it is possible to distinguish cancer patients from healthy subjects by verifying if the pan-cytokeratin (panCK) marker can be identified in the patient. However, these biomarkers are only able to identify the presence of CTCs in the patient while not helping predict the cancer's origins nor the metastasis stage, since they are present in many different types of carcinomas (including prostate cancer) [30].

Recent research has demonstrated, that CTCs are insufficient for the formation of metastasis since the tumour microenvironment is made up of leukocytes, fibroblasts, and vascular endothelial cells, with immune cells constituting the majority [31], [32]. Monocytes and monocyte-derived macrophages are immune cells that can impact tumour cell invasiveness, motility, and metastatic potential, and, as a result, when chemokines draw them into tissues peripheral to the circulation, they grow into differentiated mature macrophages that perform particular immunological functions [33]. Circulating cancer-associated macrophages-like cells (CAMLs) are described as highly diversified giant phagocytic cells of the myeloid lineage, whose size ranges, shapes, and nuclear profiles can largely vary [34]; these are generally quite big, measuring between 25  $\mu\text{m}$  and 300  $\mu\text{m}$ , with an atypically large nuclei (between 14  $\mu\text{m}$  and 64  $\mu\text{m}$ ) or perhaps even several separate nuclei, and might even have different morphological profiles, as can be seen in Figure 2.5 [35]. Since they are engaged in phagocytosis of foreign necrotic tissue, tissue reabsorption, and inflammation, these cells are different than CTCs, with researcher thinking that CAMLs play an important role in enabling tumour cells to morph into CTCs by releasing cytokines and growth factors, with both of these types of cells eventually migrating into the peripheral circulation via the lymphatic system or intravasate past intratumour capillary barriers [34], [36], [37].

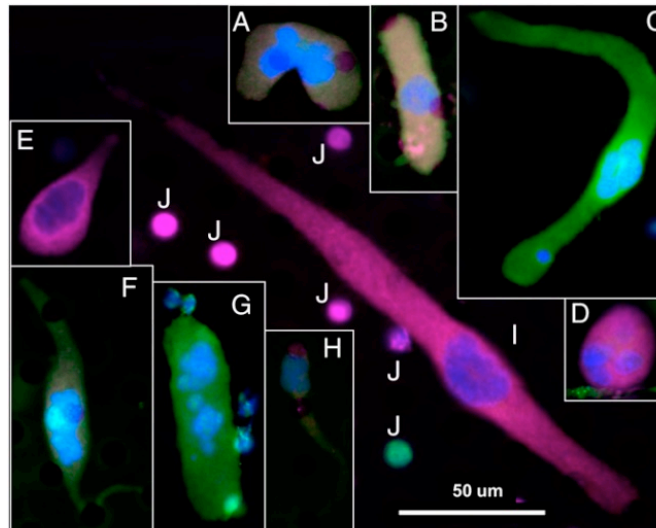


Figure 2.5 - Morphologies of different types of CAMLs (giant macrophages). From an origin standpoint, these can be classified as pancreatic cells (A, F, and G), breast cells (B, C, and D), prostate cells (E, H, and I) and typical WBCs (J); in regards to their morphology, they can be amorphous (A), oblong (B and G), spindle-shaped (C, F, and I), round (D), and tadpole-shaped (E and H).

CAMLs have been detected in all cancer patients, regardless of cancer type and development stage, in contrast to CTCs, which has been found predominantly in metastatic tumours [37]. Due to their heterogeneity, these cells have a heterogeneous markers expression, as CAMLs might express, epithelial, monocyte, endothelial, and megakaryocyte protein markers [34], [38]. Taking this into account, CAMLs show potential to be a useful biomarker for all cancer stages [34]. Thus, to better understand the biological characteristics of solid tumours, it's fundamental that these cellular components are characterized and monitored.

Despite their medical significance, rare cancer cells research is hampered by a lack of effective and reliable CTCs and CAMLs separation procedures due to their relatively uncommon incidence (i.e., ~1–100 CTCs per  $10^9$  blood cells); because of this, as well as their very diverse morphologies and molecular signatures, isolating them from blood is difficult, limiting their utility as possible cancer biomarkers in clinical cancer management [39]. As such, there is a clear need for developing efficient and simple macroscale or microscale CTCs and CAMLs separation techniques.

### 2.3 Cell Separation Methods

Several clinical and scientific fields are interested in the separation and sorting of distinct populations or subpopulations of blood cells from unprocessed or minimally handled blood specimens, as it is important in the diagnosis and prognosis of physiologic and pathologic disorders such infectious illnesses, tumours, and inflammatory reactions [1].

As such, prior to blood analysis, cell separation is an important sample preparation process in biomedical research to filter the target cell population and reduce cell-cell interactions. In clinical samples that are highly heterogeneous, for example, subpopulations of cells with distinct biological signatures and roles are commonly detected, which means that, in order to enable downstream biological tests, it is important to separate specific target cells. Accurate clinical evaluation will be achieved by efficiently extracting viable blood cells, such as cancer-related rare cells (CTCs or CAMLs,  $\sim 1$  in 100 cells/mL) from a huge cellular population ( $\sim 5$  billion RBCs/mL) [1], for further downstream analyses.

In order to have an efficient system that is able to isolate one or various component from the bloodstream, there are some key requirements that a cell separation technique has to comply: it has to be able to perform a high separation resolution; the separated cells should have high purity; it should admit a high throughput to process larger sample volumes; it must be versatile in order to adapt to different cell types and samples and show operational robustness, as well as reproducibility [40].

### 2.3.1 Label-dependent and label-free cell separation techniques

Cell separation techniques are commonly classified into two groups, depending if it follows a label-dependent (affinity-binding approaches) or a label-free (conventional separation techniques) approach [40].

#### *2.3.1.1 Affinity-binding approaches (label-dependent)*

Affinity-based cell separation techniques such as fluorescence-activated cell sorting (FACS) and magnetic-activated cell sorting (MACS), both illustrated in Figure 2.6, have become popular among biologists as a result of the considerable growth of monoclonal antibodies available. In this kind of approach, prior to separation, target cells are immunolabeled with antibodies that bind to particular surface markers [41]



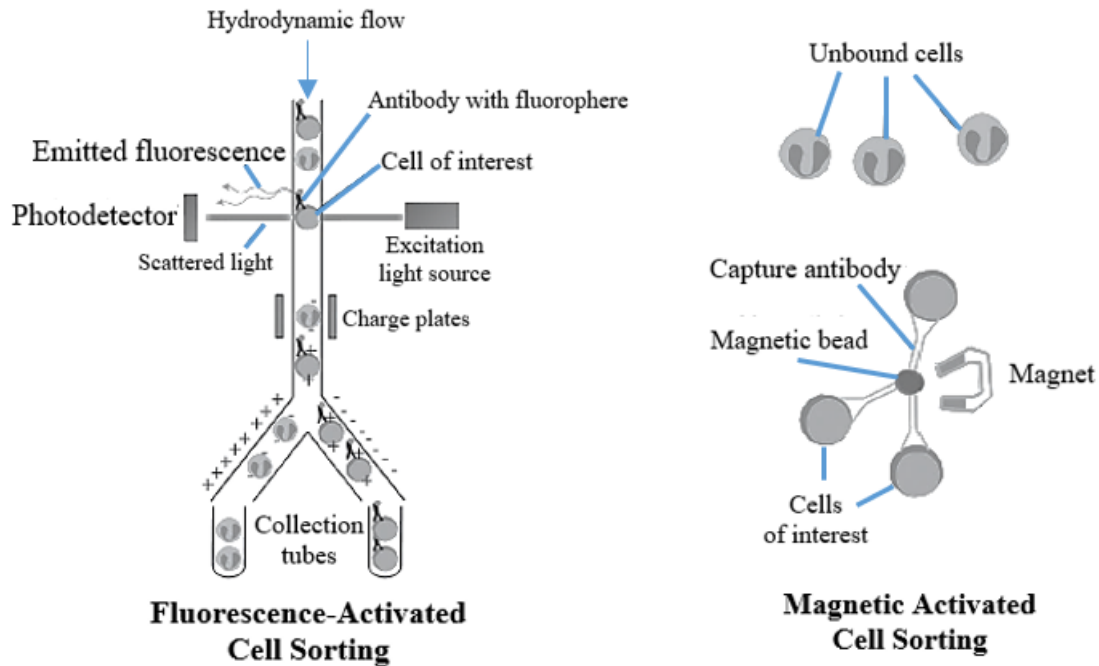


Figure 2.6 - Examples of affinity-binding approaches procedures, as MACS uses magnetic beads coupled with antibodies that are introduced to a pool of cells and attached to the cells expressing the specific protein marker, while FACS makes use of antibodies labelled with fluorophores, adapted from [1].

Even though affinity binding techniques usually offer better separation purity, the use of surface antigens are less favourable because their expression levels are highly heterogeneous and tumour-dependent, as well as the retrieval of collected CTCs is difficult thanks to the strong cell binding in the device [42]. Besides that, due to EMT, which causes down-regulation of epithelial markers (i.e., EpCAM) widely utilized for affinity binding, there is a possibility of losing the most of the CTC subpopulation, which might result in a potential underestimation of the real number of CTCs present in the bloodstream [43]. For example, the only medical instrument that follows an affinity-based approach and clinically authorized in the last decade by the FDA is the CellSearch<sup>®</sup> system from Janssen Diagnostics, but it fails in isolating the majority of CTCs in a blood sample (7.5 mL), omitting cells that have undergone a complete EMT phenotype or have a low degree of cytokeratin expression [40], [44].

These approaches are labour-intensive, time-consuming, and costly, and the cell yield or recovery is too reliant on a qualified user conducting the procedure. Furthermore, recent clinical researches have demonstrated that some CTCs recovered from peripheral blood also display EMT and stem cell markers, emphasising the importance of adopting non-EpCAM enrichment approaches as well as other EMT markers such as vimentin and N-cadherin for precise CTC enumeration [45], [46].

*2.3.1.2 Conventional separation techniques (label-free)*

In order to avoid these problems linked with the affinity-binding approaches, there's been an urge to create traditional label-free separation techniques on a micro scale level, which might rely on biophysical features such as size, density, deformability, or dielectric properties [40], [47]–[53].

Membrane filtration and centrifugation are two common "label-free" macro separation techniques that are both widely accessible and simple to perform [41]. Differential centrifugation is a common technique for sorting cells depending on their size and density [41]. Membrane filtration works by size-exclusion, retaining cells bigger than a specific size (larger than the pore size) while allowing smaller cells to flow through a porous matrix, with target cells being collected either on the membrane or in the filtrate [41]. However, these label-free methods also present several disadvantages, namely only being able to process low throughputs, clogging issues, low ability to recover interest cells, complex integration of external force fields, and potential loss of cell viability, all of which make them unsuitable for widespread application, particularly in clinical settings [54], [55]. For example, it's hard to have an efficient separation of blood cells with centrifugation or size-based filtration approaches using fibrous membranes or track-etched polycarbonate filters, which represent some of the widely used conventional "label-free" separation approaches. Apart from that, traditional macroscale blood cell separation procedures demand a huge volume of blood and numerous manual interventions that are prone to introducing contaminants, while also creating a need for competent technicians and well-equipped, expensive facilities [1].

In spite of that, novel microfluidics and lab-on-a-chip (LOC) technology show a lot of promise as it is a particular kind of microscale label-free approach that has been developing positively and gaining importance in recent years since it allows for an efficient high throughput blood cell separation, due to its precise fluid behaviour control and capacity to scale down the required sample volume and enable continuous non-invasive molecular and functional analysis of blood cells down to the single-cell level [1]. Furthermore, by exploring unique fluidic transport phenomena in confining microfluidic environments and integrating physical methods and analytical assays in a single-chip format, integrated microfluidic approaches for blood cell sorting are provided with better comprehensive and analysis capabilities than conventional macroscale methods [1].

Thus, microfluidic cell separation devices have several benefits over traditional cell sorters, including portability, simplicity of operation and low sample and reagent consumption, which might allow the development of point-of-care diagnostic systems, and higher particle separation resolution, due to its

channel diameters being specifically tailored to the interest particles' cell size for improved separation control [40].

### 2.3.2 Microfluidic lab-on-a-chip cell separation

Microfluidics, which is defined by George Whiteside as “the science and technology of systems that process or manipulate small ( $10^9$  to  $10^8$  L) amounts of fluids, using channels with dimensions of tens to hundreds of micrometres”, has fundamentally transformed chemical analysis and biological testing due to its unique physical phenomenon characteristics and flow control in the microscale since the birth of these lab-on-a-chip (LOC) technologies in the 1990s [56], [57].

Higher analysis efficiency, reduced sample and reagent usage, shorter processing time, great spatial resolution, ability to perform dimension matching between channel sizes and cell diameter, ease of operation, reduced device cost, and great portability are all advantages of these downsized systems, which allows them to play an increasingly important role in the field of single-cell study [13], [58]. Consequently, taking into account its ability to achieve remarkable size resolution and purity, as well as high throughput sample processing, LOC cell separation systems have become a key instrument for cell separation purposes [41].

It should be noted, however, that microfluidics has not taken off in the way that many expected, as a lack of standardisation has limited LOC technology, with needlessly complicated and sophisticated designs being developed and manufactured by engineers, making it difficult for these to have a real-world application, thus remaining simply an academic research tool [56], [59].

Based on the presence or absence of external fields (such as electric, optical, acoustic, magnetic fields), microfluidic cell separation techniques are divided and classified into active and passive methods; while active techniques employ external fields to impose varying forces on cells in order to induce particle separation, passive separation methods rely solely on intrinsic hydrodynamic forces during fluid flow, which can be controlled by changing the microchannel design and flow conditions [41]. Various passive separation techniques are compared on Table 2.1.

Table 2.1 - Comparison of various microfluidic passive separation techniques, adapted from [49].

<b>Separation technique</b>	<b>Mechanism/principle</b>	<b>Separation criteria</b>	<b>Throughput</b>
Biomimetic	Hydrodynamic force/ Fåhræus effect	Size deformability	10 $\mu$ L/h
Hydrodynamic	Streamline manipulation	Size shape	20 $\mu$ L/min > $10^5$ /min
Hydrophoretic filtration	Pressure field gradient	Size	$4 \times 10^3$ /s
Inertial	Lift force secondary flow	Size shape	$\sim 10^6$ /min
Microstructure (Pillars and weirs)	Laminar flow/perturbation of flow	Size deformability	$10^3$ $\mu$ m/s 5 $\mu$ L/min
Surface affinity	Specific binding to surface markers	Size surface biomarkers	1–2 mL/h
Pinched flow fractionation (PFF)	Laminar flow (Hydrodynamic force)	Size	$\sim 4 \times 10^3$ /min 20 $\mu$ L/h

Because of its ease of use and greater separation resolution when compared to the others technologies, inertial microfluidics has emerged as a very promising option for size-based cell separation [41]. Di Carlo et al. [60] published the first key paper about this approach in 2007, in which the particle inertial focusing effects in microfluidics and their use for high throughput size-based particle separation was described, and ever since then numerous inertial microfluidics review articles have been published, providing a great overview of inertial microfluidics in various channel geometries [60]. Among those, the spiral microchannel geometry is one of the most popular cell separation designs since it makes use of both size-dependent particle inertial focusing and secondary Dean-induced migration phenomena to accomplish cell separation.

## 2.4 Spiral Inertial Microfluidics

Inertial focusing, as the name implies, takes advantage of inertial forces created by the fluid flow within a confined microchannel. Shear-gradient lift and wall-induced lift combine to provide a net lift force

which propels particles toward equilibrium points inside the microchannel cross-section, rapidly transforming an initially homogenous microparticle flow into a highly focused microparticle stream [60].

There are two variables that are mainly responsible for regulating these inertial forces, which are the Dean number and the ratio of particle diameter to the microchannel hydraulic diameter [1]. By manipulating these two parameters it is possible to optimize a device design, in order to achieve blood cell separation and sorting, and specifically to isolate CTCs from diluted blood [1], [61]. This is possible to accomplish by designing a microfluidic device with a curvilinear channel; as particles travel through the microchannel at different speeds, due to a centrifugal acceleration of the fluid flow, an extra lift (the Dean drag force) is generated thanks to the channel curvature [12]. The devices that contain this sorting method with a curved section are designated spiral devices [12].

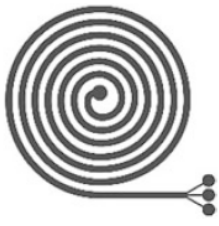



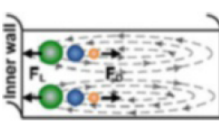
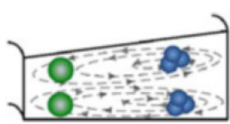
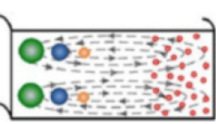
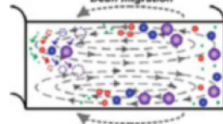




The ultimate particle location is determined by a net force between Dean drag, shear-gradient lift, and wall-induced lift, which varies depending on particle size [12]. As hematologic cells are usually smaller than CTCs, these cells tend to flow towards the outer wall, while CTCs and cells with higher sizes flowed closer to the inner wall, theoretically resulting in an efficient separation of CTCs or rare cells from hematologic cells [61].

It should be taken into account that there's a factor that has been deeply limiting to the use of inertial microfluidics for blood related separation: the large red blood cells (RBCs) background (45% v/v in blood,  $\sim 10^9$  RBCs/mL), as cell-to-cell interactions can have a significant negative impact on cell focusing behaviour and, as a result, in the separation efficiency [62].

#### 2.4.1 Classification of spiral devices

Due to the dominant viscous drag forces (low Reynolds), fluid mixing at the microscale presents a number of obstacles, as molecular diffusion continues to be the primary transport mechanism in this laminar flow regime [41]. As the form and size of Dean vortices are affected by flow conditions and channel geometries, these parameters have been intensively researched in the spiral inertial microfluidics field of studies in order to improve cell sorting capacities [63], [64]. There are four main types of spiral devices, each with its own focusing methods and characteristics: rectangular spiral microfluidics, trapezoidal spiral microfluidics, double-inlet spiral (designated as Dean Flow Fractionation (DFF)), and High-resolution Dean Flow Fractionation (HiDFF), and their properties are compared in Table 2.2 [41].

Table 2.2 - Comparison of different spiral devices configuration and sorting, adapted from [49].

Type	Rectangular spiral microfluidics	Trapezoid spiral microfluidics	Dean flow fractionation (DFF)	High resolution DFF (HiDFF)
Configuration				
Principle				
Size	 ~5–50 $\mu\text{m}$	 ~5–30 $\mu\text{m}$	 ~1–30 $\mu\text{m}$	 ~1–3 $\mu\text{m}$
Mode	Multiplexed sorting	Binary sorting	Multiplexed sorting	Binary sorting
Sample Flow Rate	~0.5–3 mL/min	~0.5–6 mL/min	~0.1–0.2 mL/min	~0.05–0.2 mL/min
Cell	~ $10^{5-6}$ /mL (~0.1–0.5% hematocrit)	~ $10^{6-7}$ /mL (~0.5–2% hematocrit)	~ $10^{6-8}$ /mL (~10–20% hematocrit)	~ $10^{6-8}$ /mL (~10–20% hematocrit)
Applications	Cell separation Particle concentrator Cell alignment and ordering	Rare cell isolation Microfiltration Plasma separation	Rare cell isolation Bacterial sorting Protein purification Buffer exchange	Microvesicle isolation Nanoparticles separation Bacterial sorting

However, some of these systems do not meet the established requirements, as the rectangular and trapezoidal spiral microchannels. The two strategies can be highly effective for size-based particle and cell separation while working with low sample concentrations (around  $\sim 10^{5-7}$ /mL), but their usage in blood-related applications is severely constrained due to the high RBC background ( $\sim 45\%$  v/v,  $\sim 10^9$  RBCs/mL) [62]. The cells interactions can significantly impact cell focusing behaviour and thus decrease separation efficiency [62]. Another alternative consists on the dilution of whole blood samples (50–100 x,  $\sim 0.1$ –2% haematocrit), but that would increase processing time to a level unsuitable to process the large volumes of blood samples required for CTCs isolation applications, namely 7.5 mL [41].

In order to solve these issues, the Dean Flow Fractionation (DFF) configuration developed by Hou et al [12] was introduced, consisting in a more flexible and practical separation approach, allows for a continuous collection of sorted CTCs in a single stage [12]. When compared to the previously mentioned CTCs separation spiral inertial methods, DFF technique presents many advantages such as the ability to process large amounts of whole blood samples in a short period of time (3 mL of whole blood in an hour) while also efficiently separating the CTCs, thus providing unmatched separation and throughput performance [12]. Besides that, this type of setting also holds advantages to affinity-capture or physical filtration microdevices, as the constant collection of sorted CTCs and its brief residence time inside the device's channels (<10 msec) considerably reduces CTCs' exposure time to the shear in the channel, minimizing the shear-induced alterations to the CTCs' phenotype and preserving its properties and allowing for a better molecular characterization [12]. Lastly, using this sort of configuration, the device setup and operation are simplified because sample preparation is minimal and just syringe pumps are needed for it to work; this is something that is very important since it allows technicians and clinicians with minimum training and expertise to easily work with the DFF device, facilitating its commercialization and adoption in clinical settings [12].

In sum, the Dean Flow Fractionation (DFF) configuration is a flexible blood separation technology that, via the characterization of differences in cell morphology, can be used to separate diseased cells (such as CTCs) from whole blood.

#### *2.3.1.1 Dean Flow Fractionation (DFF) characteristics*

Hou et al [12] developed a Dean Flow Fractionation (DFF) configuration with two-inlet and two-outlet spiral device that has the purpose of isolating CTCs from whole blood, represented in Figure 2.7 [12]. By taking advantage of the size difference between cancer cells and other blood cells, this technique allows for larger CTCs and CAMLs to be inertial focused towards the inner wall, whereas smaller blood components, such as RBCs and WBCs, are predominantly impacted by the Dean drag and transferred towards the outer wall, thus resulting in the isolation of the rare cells.

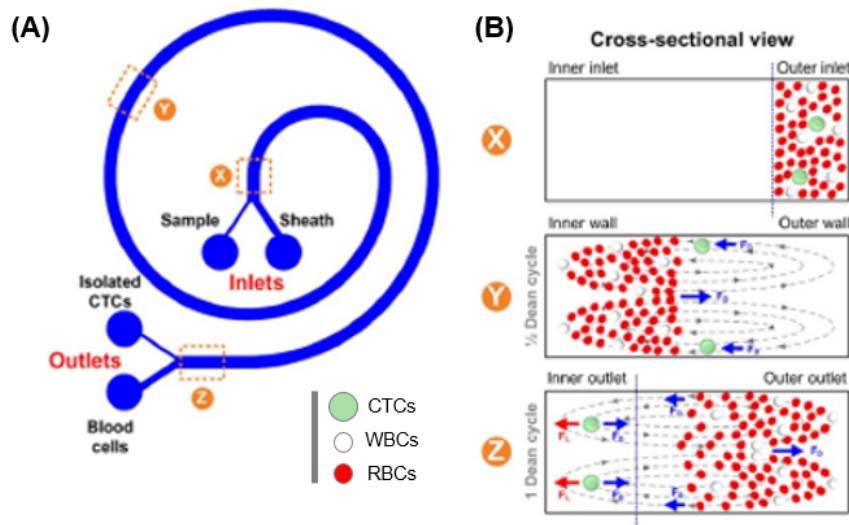


Figure 2.7 - Schematic representation of the separation principle for high-throughput CTCs separation using Dean Flow Fractionation (DFF): (A) inertial microfluidic design and (B) representation of the cells focusing considering the cross-section of the device, adapted from [12].

This separation approach uses a sheath buffer (which is used to influence particle focusing), allowing for a seamless and controlled Dean migration of huge volumes of RBCs, enabling the processing of even high hematocrit blood samples ( $\sim 20\text{--}25\%$ ) [41]. The sample to sheath flow rate ratio ends up playing a major role in the DFF technique, as its careful regulation will allow DFF to serve as an effective buffer exchange system to efficiently deplete tiny biological components such as biomolecules (aptamers) and nanoparticles from the target cells [41], [65], [66].

From a clinical and research standpoint, the DFF spiral biochip presents a series of distinct features that make it extremely valuable, such as:

1. CTCs (or the isolated cells) are counted in suspension rather than immobilized on chips, allowing for rapid manipulation and analysis, as the continuous collection of viable CTCs enables easy coupling with, for example, conventional 96-well plate for subsequent biological assays or other downstream tests [40].
2. Isolation principle is not dependent on tumour antigen and, as a result, this technique might be more sensitive than other immuno-based technologies. CTC clusters, which are thought to play a role in tumour metastasis, may also be detected and quantified from blood samples [67].
3. High purity of the enriched samples, with up to 4 log WBC depletion [49], [68]. The CTC separation technique's high specificity allows for better precision in genome sequencing and mapping, as well as single-cell analysis [40].



4. The large microchannel diameters and high flow conditions, which enable processing high hematocrit blood samples, minimizing clogging difficulties, unlike conventional affinity-capture or physical filtering microfluidic devices, ensuring a robust separation platform for processing of large clinical sample volumes [12].

Though, there are also some limitations in this configuration, since despite the fact that spiral microfluidics avoids the usage of immunoaffinity markers, which can have limited sensitivity and specificity, the DFF approach may still be unable to identify the smaller CTCs, as the isolation of the interest particles is performed in accordance to a pre-established size threshold; for example, if the defined size threshold for separation of cells is too low in order to isolate even the smallest CTCs ( $\sim 10 \mu\text{m}$ ), this would result in other non-interest cells such as WBCs ( $\sim 12 \mu\text{m}$ ) to be separated into the interest outlets [40]. Thus, even if there is some loss of smaller CTCs, it is better to define a higher size threshold in order to avoid non-interest cell contamination. Nevertheless, thanks to its proven high isolation efficiency, it is expected that a significant pool of CTCs can be obtained for therapeutic and research purposes [40]. Besides the design and working flow rates that should be manage for high isolation, other strategies can be applied, namely to decrease cellular interactions that effect inertial focusing in microchannels, RBC lysis and subsequent sample dilution can be applied [40].

These extra steps can be avoided by using a cascaded spiral configuration, as a 2-stage cascaded DFF system can be built up by connecting the CTCs outlet of the first spiral device to the sample intake of a second spiral device for full RBC removal from the sorted CTCs. This sort of setup enables for the elimination of any leftover RBCs and leukocytes that may reach the CTCs output during the first stage due to undesired cell-cell interactions, as well as for the reduction of CTCs loss by removing the need to manually transfer the separated CTCs solution to a new device, all while maintaining the same throughput and processing time values (20 mins/mL of whole blood) since both spiral devices are working in conjunction, as well as achieving a CTC recovery rate of more than 85% according to hemacytometer analysis and thus outperforming existing CTC sorting approaches based on size and affinity [12].

## 2.5 Flow characteristics

To properly understand the advantages of inertial microfluidic systems, it's necessary to understand the physics of fluids at this size and how this influences their behaviour.

A fluid, such as a liquid, may be regarded of as a material that deforms continuously under shear stress when an external force is applied, displacing some of its constituents at the boundary layer (i.e.,

surface) [69]. The continuum approach, which means modelling the mechanical behaviour of materials as a continuous mass instead of separate particles, can be assumed in microfluidic systems, since fluid is a material that can be deformed continuously under the action of shear stress without a change in its properties [70]. In order to characterize a liquid, it is fundamental to know three major properties, which are its density,  $\rho$  (kg/m<sup>3</sup>), its pressure,  $P$  (Pa), and its viscosity,  $\mu$  (Pa.s).

One of the fundamental principles in order to understand the physics of fluids is the conservation of mass principle which, according to the continuity equation (Equation (1)), assures that the mass entering any control volume will be the same as the mass exiting said volume, where  $\rho_1$  is the fluid density at point 1,  $A_1$  is the area across which the fluid enters the control volume and  $v_1$  the average velocity of the fluid across  $A_1$ ; in accordance with this logic, the variables with the index '2' refer to point 2 [20].

$$\rho_1 A_1 v_1 = \rho_2 A_2 v_2 \quad (1)$$

The continuity equation may be simplified and rewritten as Equation (2) for incompressible flows, such as blood, as for these the fluid density is constant for a set control volume ( $\rho_1 = \rho_2$ ) and the mass does not change [20]. It should be noted that  $Q$  is the volume flow rate that traverses the control volume. The continuity equation can be particularly useful when applied to a bifurcation, such as the ones that might be found in a DFF device, with the equation being expressed as Equation (3) or alternatively Equation (4) for a situation like the one illustrated on Figure 2.8 [20].

$$A_1 v_1 = A_2 v_2 = Q = \text{constant} \quad (2)$$

$$Q_1 = Q_2 + Q_3 \quad (3)$$

$$A_1 v_1 = A_2 v_2 + A_3 v_3 \quad (4)$$

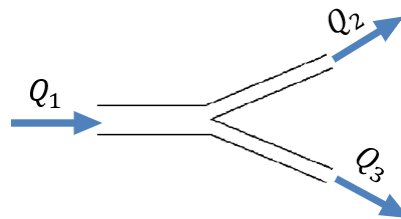


Figure 2.8 - Bifurcation in a DFF device's microchannels, for which the continuity equation can be applied, adapted from [21].

In regards to pressure in a microfluidic system, where the channel depths are on the micrometre scale, pressure changes owing to differing depths may be ignored, however, since the microchannels in which the liquid is present might have inlets and outlets, any external pressure difference impacting them will be perceived by the liquid, which then causes the flow to begin. This flow does not flow freely though, as it experiences a certain resistance to its motion, with this internal friction being called viscosity [69].

In fluid mechanics, there are many phenomena that fluids have to follow, with one of them being known as the no-slip condition, with all fluids satisfying this condition [20]. Considering a scenario of two parallel plates separated by a film of liquid of thickness  $L$ , illustrated in Figure 2.9, while the lower plate remains stationary, an external force,  $F$ , causes the upper plate to move, resulting velocity,  $v$ , because of the intermolecular interactions between the liquid molecules, the movement of the upper plate causes the molecules in the immediately following layer to move as well, with this process being continued across the successive levels [69]. This then indicates that the velocities of these layers range from  $v$  (the layer nearest to plate B) to zero in a steady state (the layer closest to plate A) and, thus, the fluid molecules cling to the plate and do not slide over its surface [20].

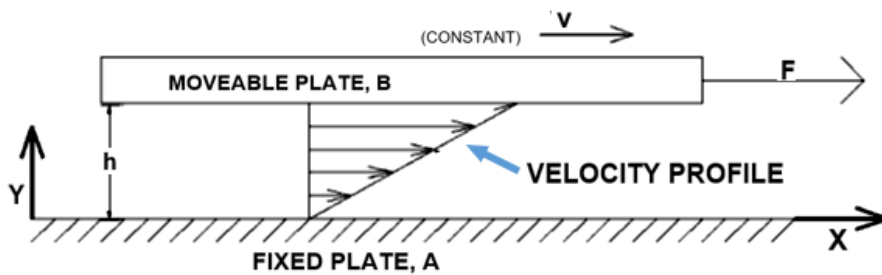


Figure 2.9 - Velocity profile in a fluid between two parallel plates demonstrating the no-slip condition, adapted from [21].

The shear stress ( $\tau = F/A$ ) is caused by the area of the liquid surface,  $A$ , that is impacted by the force, while the shear strain ( $\gamma = \Delta x/L$ ) is caused by the displacement of the liquid at the top plate,  $\Delta x$ , in relation to the thickness of the film,  $L$ . With this in mind, the coefficient of viscosity,  $\mu$ , can be defined as the ratio of the shear stress to the shear rate, as stated in Equation (5), with the results of this equation making it possible to determine if the fluid being studied can be considered as a Newtonian fluid [20]. In case the shear stress of the fluid is directly proportional to the velocity gradient, or putting into other words, if the viscosity of that fluid remains constant, it is indeed a Newtonian fluid, as fluids in which the viscosity varies in accordance with the shear rate are called non-Newtonian [20]. It should be noted that with increasing shear rate, the viscosity of non-Newtonian fluids can either increase (shear thickening) or drop (shear thinning) depending on fluid properties [20]. When it comes to fluid mechanics in

microfluidics, shear stress is an important concept to understand, especially when the pressures applied to blood are high enough to cause red blood cell rupture.

$$\mu = \frac{F/A}{v/l} \quad (5)$$

The viscosity of a fluid, which is related to its resistance to deformation, is one of its most important attributes, with the viscosity of many fluids being a constant property that only varies with temperature and pressure [70]. In fluid mechanics, the Navier-Stokes equations, as presented in Equation (6), can be used to characterize the motion of a viscous fluid. The Navier-Stokes equations, which are based on the fundamental laws of conservation, regulate the motion of fluids (mass, momentum, and energy). Because the equations include more unknown factors, these are solved using a variety of boundary conditions and assumptions [41].

$$\rho(\partial u / \partial t + u \cdot \nabla u) = -\nabla p + \mu \nabla^2 u + f \quad (6)$$

In the equation above,  $\rho$  represents the fluid density,  $\mu$  is the fluid dynamic viscosity,  $u$  is the fluid velocity field,  $p$  represents fluid pressure field, and  $f$  is the vector field of external body forces imparting on fluid elements.  $\rho(\partial u / \partial t + u \cdot \nabla u)$  corresponds to the inertial forces,  $-\nabla p$  corresponds to pressures, and  $\mu \nabla^2 u$  corresponds to viscous forces [41]. As blood constitutes a steady, incompressible fluid ( $\nabla u = 0$ ), then Equation (7) may be simplified and, when solved together with the continuity equation (Equation (1)), can be written as Equation (7), with the conservation of momentum being represented by the Navier-Stokes equations, whereas the conservation of mass is represented by the continuity equation [20].

$$\frac{\partial(\rho)}{\partial t} + \vec{\nabla} \cdot (\rho \vec{u}) = 0 \quad (7)$$

The Reynolds number ( $Re$ ) can be used to determine the fluid flow conditions in microsystems [70]. The channel Reynolds number ( $Re_c$ ) is a dimensionless quantity that quantifies the ratio of inertial to viscous forces in a fluidic system, as stated in Equation (8) and is used to define fluid flow [41].

$$Re_c = \frac{\rho U_m D_h}{\mu} \quad (8)$$

Here,  $\rho$  is the density of the fluid,  $U_m$  is the maximum velocity of the fluid flow,  $D_h$  is the characteristic linear dimension of the system (either diameter or channel depth) and  $\mu$  is the dynamic viscosity of the fluid. In case the microchannel under consideration does not have a cylindrical cross-section, the hydraulic diameter,  $D_h$ , will be employed in order to compute  $Re_c$ , in accordance to Equation (9), where  $P_{wet}$  is the perimeter that is in contact with the liquid and  $A_{CS}$  is the cross-sectional area.

$$D_h = \frac{4A_{CS}}{P_{wet}} \quad (9)$$

From Equation (8) it can be deduced that the Reynolds number decreases as the system's characteristic dimensions decrease; when the Reynolds number goes below 2000, the system enters the laminar flow regime, which differs from turbulent flow ( $Re_c > 4000$ ) in various ways [71]. For starters, laminar flow is highly predictable, which makes mathematical modelling of these systems easier and less intensive; furthermore, unlike in the turbulent regime, there is no convective mixing in the laminar phase, only diffusion, resulting in extremely predictable kinetics [71]. As for the particle Reynolds number ( $Re_p$ ) it is used to characterize the interaction between the particles ( $a$  is the particle size) and the channel dimensions, according to Equation (10), when considering finite-size particles in the channel flow [41].

$$Re_p = Re_c \frac{a^2}{D_h^2} = \frac{\rho U_m a^2}{\mu D_h} \quad (10)$$

The size ratio of particle to channel constitutes a very important variable, as the flow pattern in the channel will change accordingly to it [41]. As such, for example, the viscous drag dominates at  $Re_p \ll 1$  and the particles are classified as "point-particles" [41]. Inertial effects in the channel flow become increasingly obvious as  $Re_p$  grows, and when  $Re_c$  falls below a crucial value of around approximately 2040 laminar flow begins [72].  $Re_c$  is often less than 100 in microfluidics due to the narrow channel diameters (normally less than 1 mm), as fluid flow is entirely laminar and thus viscous forces of the fluid outweigh inertial forces (Stokes flow) [41]. This means that, for most microfluidic systems, the inertial element of the Navier-Stokes equation (Equation (6)) is neglected by equating the left-hand side of the equation to zero.

### 2.5.1 Fluid transport mechanics

Microfluidic flows are frequently linked with significant viscous drag forces (low Reynolds number,  $Re$ ), which provide laminar flow profiles that entrain suspended particles and cells along streamlines [58]. It has been demonstrated that, due to considerable inertial forces, particles may migrate across

streamlines to concentrate at various points in microchannels, which can be used for high throughput, size-based particle and cell separation [60], [61], [73], [74].

Particle lateral migration and focusing are caused by the combination of two inertial lift forces ( $F_l$ ) operating in opposing directions on the particles: shear induced lift force and wall-induced lift force; besides that, due to the presence of transverse Dean flows coming from the centrifugal acceleration of fluid flow in curved channels, particles encounter an extra lateral Dean drag force ( $F_d$ ) in curvilinear channels, such as the DFF spiral device setting [60], [75]. In order to reach an efficient, high-resolution size-based separation of whole blood particles, it's crucial to take advantage of the interplay between inertial lift and Dean forces.

### 2.5.1.1 Inertial lift forces

The interaction of two dominant inertial lift forces, the shear gradient induced lift force pushing particles in the medium away from the channel centre and the wall induced lift force repelling particles away from the wall, was found to be the cause of this unusual particle lateral migration effect. Besides these forces, it's also important to note that the Stoke's drag force in secondary lateral flow is another crucial factor to consider [41].

For a particle flowing near the channel wall, the Wall Induced Lift Force ( $F_{WL}$ ) is formed as the contact between the particle and the channel wall causes the particle to lag behind the fluid flow; furthermore, because of the constrained flow area between the particle and the channel wall, fluid flow towards the top side of the particle will be accelerated as more streamlines are diverted to this side. This results in a decreased pressure on the particle's "opposite to the wall" side, resulting in a lift force directed away from the wall, as depicted in Figure 2.10 [41].

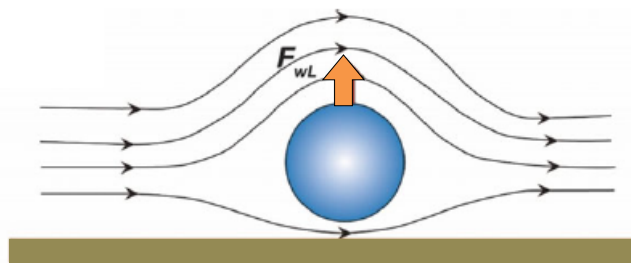


Figure 2.10 - Schematic illustration of the wall induced lift force experienced by particles in inertial microfluidics, adapted from [42].

The curvature of the parabolic velocity profile induces the shear gradient lift force, as the velocity magnitudes on either side of the particle are distinct, as illustrated in Figure 2.11, resulting in a pressure difference between the top and bottom sides of the particle. The shear gradient lift force ( $F_{SL}$ ) is generated on the particle due to this pressure discrepancy, which pushes it towards the channel wall until it is balanced by the wall induced lift force [41]. The net lift force acting on a particle changes depending on where it is positioned in the microchannel, as the diverse fluid dynamics at different places in the channel are to blame for the variance in lift patterns: the shear gradient lift force prevails at the channel's centre, whereas the wall induced lift force is more substantial towards the channel's periphery [41].

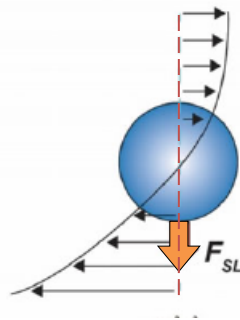


Figure 2.11 - Schematic illustration of the shear gradient lift force experienced by particles in inertial microfluidics, adapted from [42].

For a Poiseuille flow, Asmolov developed an analytical equation for the net lift force imposed on a solid particle ( $a/D_h \ll 0.1$ ), which can be seen in Equation (11), where  $f(Re_c, x)$  is the lift coefficient which depends on the particle position within the channel ( $x$ ) and the channel Reynolds number ( $Re_c$ ) [76].

$$F_L = \frac{\rho U_m^2 a^4}{D_h^2} f(Re_c, x) = \frac{\mu^2}{\rho} R_p^2 f(Re_c, x) \quad (11)$$

Existing theoretical predictions are based on the "point-particle" approach, which neglects the particle size impact; however, when the size of the particles approaches the channel diameter the particles will alter the flow disruption [41]. Besides that, it has also been experimentally demonstrated that the net lift force varies with the position of the particles in the microchannel [77]. As such, for a particle of finite-size ( $0.05 \leq a/D_h \leq 0.2$ ), the lift force scaling relationship varies when comparing the area near the channel wall (Equation (12)) and the one near the centre of the channel (Equation (13)).

$$F_{WL} = \frac{\rho U_m^2 a^6}{D_h^4} f_{WL}(Re_c, x) \quad (12)$$

$$F_{SL} = \frac{\rho U_m^2 a^3}{D_h} f_{SL}(Re_c, x) \quad (13)$$

The diverse fluid dynamics at different places in the channel are responsible for the variance in lift forms, as the shear gradient lift force prevails at the channel's centre, whereas the wall induced lift force is more substantial towards the channel's periphery.

### 2.5.1.2 Dean drag force

William Dean identified the now-called Dean vortices in curved channels in 1928, which resulted of a mismatch in fluid momentum inside the channel cross section caused by centrifugal acceleration acting on the fluid flow [78]. It means that, because of the parabolic flow profile, when fluid flows through a curved channel, the fluid velocity at the centre is higher than at the edges; due to centrifugal acceleration, the faster-moving fluid in the channel centre gains more momentum and is pushed toward the outside wall (the concave wall) of the channel curvature along the channel midline [41]. This also means that secondary counter-rotating flows are created to compensate for the fluid displacement due to mass conservation and, as a result, at the top and bottom of the cross-sectional plane, two symmetrical counter-rotating vortices develop (Dean vortices), as depicted in Figure 2.12 [41].

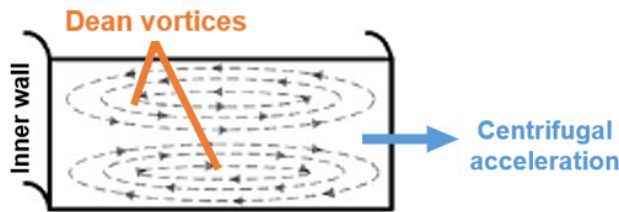


Figure 2.12 - Representation of a pair of Dean vortices within a spiral channel with a rectangular cross section, adapted from [42].

A non-dimensional Dean number ( $De$ ) can be used to determine the strength of the secondary flow ( $De$ ), according to Equation (14); in this equation,  $Re_c$  is the channel Reynolds number, previously defined in Equation (8). A large curvature ratio ( $\delta = D_h/2 R$ , where  $R$  is the average radius of curvature of the channel) will imply a faster turn in the channel (i.e., smaller radius of curvature  $R$ ) and resulting in a stronger Dean flow [41].



$$De = Re_c \sqrt{\frac{D_h}{2R}} \quad (14)$$

The expression of average transverse Dean velocity for a given  $De$  ( $U_{De}$ ) may be calculated as in Equation (15) and, as a result, assuming Stokes drag, the Dean drag force ( $F_D$ ) experienced by a particle in this flow may be calculated and stated as in Equation (16), with this force being represented in Figure 2.13.

$$U_{De} = 1.84 \times 10^{-4} De^{1.63} \quad (15)$$

$$F_D = 3\pi\mu U_{De} a = 5.4 \times 10^{-4} \pi\mu De^{1.63} a \quad (16)$$

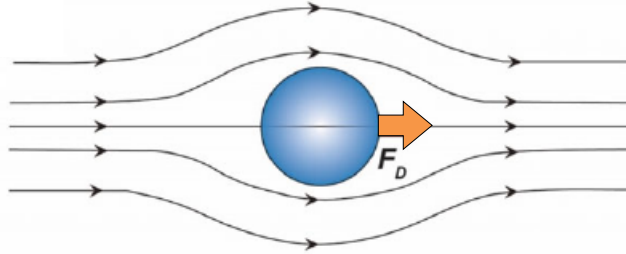


Figure 2.13 - Schematic illustration of the shear gradient lift force experienced by particles in inertial microfluidics, adapted from [42].

The Dean coupled inertial migration of particles is caused by the interaction of the net inertial lift force ( $F_L$ ) and the Dean drag force ( $F_D$ ) in spiral or curved channels. This Dean-induced lateral migration can be defined in terms of a "Dean cycle" ( $DC$ ); for example, a particle that begins near the microchannel outer wall and makes its way to the inner wall is considered to have completed half of a Dean cycle ( $DC$  0.5), while returning to the original location near the channel outer wall completes a full Dean cycle ( $DC$  1) [12]. A complete Dean cycle migration length ( $L_{dc}$ ) is approximately equal to  $2w + h$  (where  $w$  is the microchannel width and  $h$  is the channel height) and thus, for a certain microchannel length, particles may experience several  $DC$  migrations with rising flow rate conditions, while the opposite can also be verified [12].

Lastly, Di Carlo et al. [73] introduced a critical parameter  $R_f$  (Equation (17)), the ratio of shear gradient lift force to Dean drag force, to describe particle inertial focusing in curved channels, and it is widely acknowledged that particle inertial focusing in microchannels requires an  $R_f > 0.04$  (or  $a/D_h > 0.07$ ) [75], [79], [80]. Since  $R_f$  has a substantial dependence on particle size, this constitutes the

backbone for size-based particle separation in spiral devices, as the particle equilibrium separation can be adjusted by manipulating these forces [41].

$$R_f = \frac{F_{SL}}{F_D} \propto \frac{1}{\delta D_h^3} \quad (17)$$

## 2.6 Fabrication of DFF devices

In the design of microfluidic systems, the use of certain materials with specific properties is quite important. One of the cornerstones of successfully creating a device with multiple microfluidic functions is correctly selecting materials with specific qualities, such as hardness, processability, electrical conductivity, transmittance, corrosion resistance, and biocompatibility depending on its final purpose [13]. Generally, the optimum material for microfluidic DFF applications should be low-cost, easy to produce, transparent, chemically inert to the substrate being tested in the device, biocompatible, have appropriate elasticity, and allow for a rather straightforward bonding process to other surfaces [17].

The materials used in microfluidic manufacturing may be split into two categories: inorganic materials, such as silica and glass, and polymer materials [13]. Initially, silicon and glass were generally employed for fabrication, however its use presented many disadvantages, such as brittleness, high cost, bonding difficulties, complex fabrication techniques and opaqueness in the case of silicon, and as such researchers were compelled to investigate alternate materials and production methods for the fabrication of microfluidic devices, with polymer-based microfluidic coming out as a better solution [17].

As distinguished from inorganic materials, polymer materials have the benefits of diversity, processability, compatibility with biological and chemical reagents and suitability for mass production at a low cost; polymer-based microfluidics also allows for a wide range of possibilities and variation by making it possible to select appropriate materials with specified qualities in order to meet a certain requirement, as it can be seen in Figure 2.14 [81]–[83]. Therefore, polymers have become the most commonly used materials for microfluidics, with Polydimethylsiloxane, or simply PDMS, especially taking the spotlight in this field of studies, thanks to its low toxicity, easy shaping, and high thermal stability and biocompatibility [13].

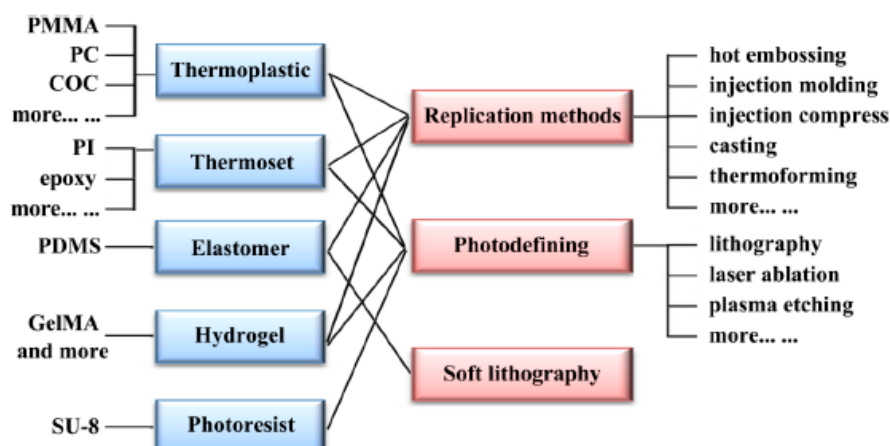


Figure 2.14 - Diagram depicting the relationship between several types of polymer materials and manufacturing methods for polymer-based microfluidics [13].

PDMS is an elastomeric substance pioneered by George Whitesides and his Harvard group in the late twentieth century [84]; it is a siloxane elastomer, a synthetic polymer with a dimethylsiloxane repeating unit  $((\text{Si}(\text{CH}_3)_2\text{O})_n)$  along its backbone, and it became the most widely used material for microfluidic devices fabrication [85].

It's an elastomer with long chains and low glass transition and melting temperatures, which allows for a lot of flexibility and elasticity. Since PDMS has a low shear modulus of 250 kPa, it acts like a flexible rubber, and its flexibility may be tweaked by adjusting the monomer-to-crosslinker ratio as well as the thickness of the manufactured device [86], [87]. Besides that, as PDMS has a high optical transparency, it allows for real-time observation, which facilitates the study of the physical and biological processes that take place within them [88]–[90]. It is also durable and permeable to gas, and as such PDMS is a good material for flexible microfluidics [85], [91], [92].

Regarding the fabrication process of the spiral devices using PDMS, it is rather simple and does not require expensive clean room facilities [71]. First a master structure has to be created, and then the solution of PDMS base and curing agent can be poured over the mould; since PDMS has a low surface energy, it is easily removed from the mould and flows into the mould' features [71].

The elastomeric structure of PDMS allows it to produce a seal capable of withstanding mild fluid pressures when placed in direct contact with another substrate [84], [93]. After this fabrication process, the PDMS channels are usually sealed with ease by bonding it to another material, as an irreversible bond between the two surfaces can be established when they are heated or put through a plasma treatment of the two interfaces, with PDMS devices being frequently sealed against a glass slide [71]. Taking advantage of the simplicity of executing this method, development of microfluidics devices became rapid

and inexpensive. Nevertheless, there have been some concerns about the usage of PDMS in recent years, as it has been verified that, at high pressures, the PDMS channel diameters can change due to its low modulus of elasticity and PDMS might also absorb tiny molecules due to its vapour permeability properties, leading to a decrease in precision [94].

### 2.6.1 Manufacturing Methods for PDMS-Based Microfluidics

The correct selection of manufacturing method also constitutes a fundamental part in an efficient microfluidic system. As such, it's critical to consider the availability of technologies and equipment, as well as the cost, speed, and fabrication capabilities (for example, the size and profile of the desired feature), while deciding on the best suited manufacturing process [95], [96]. In the case of PDMS-based microfluidics, soft lithography is the most indicated procedure for the fabrication of PDMS microfluidic device [13]. This process can be divided into two stages, which are the master mould fabrication (via photolithography, Figure 2.15 (A) and the PDMS processing (via soft lithography, Figure 2.15 (B) [13].

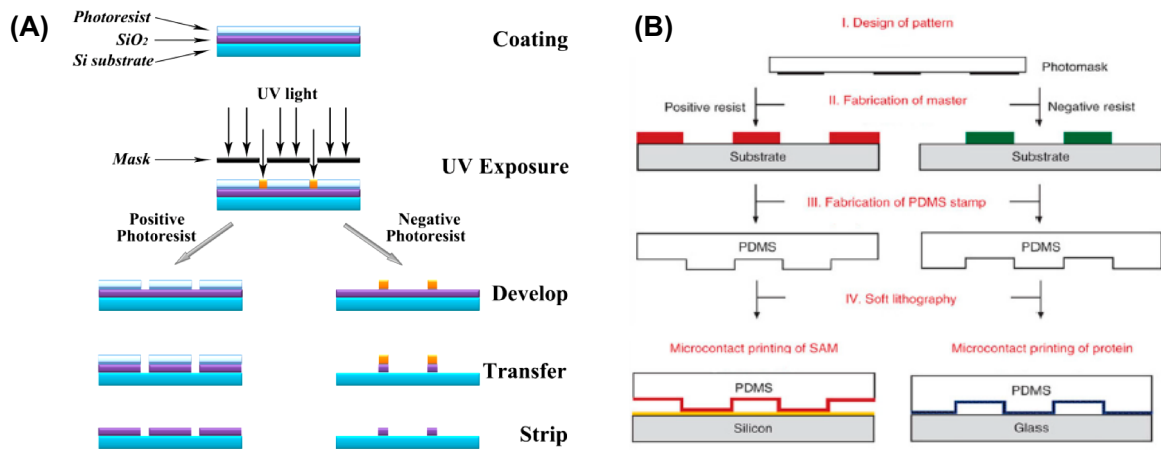


Figure 2.15 - Schematic illustration of the soft lithography procedure for the fabrication of PDMS microfluidic devices, which can be divided in two stages: (A) photolithography process and (B) soft lithography process, adapted from [22].

For the photolithography stage, also referred to as UV lithography or optical lithography, micro and nanostructures are patterned on a variety of surfaces, with light being used to stimulate the polymerization reaction and to transmit geometric patterns through photomasks, as solid microstructures are produced out of a liquid resist [13]. SU-8 is the most extensively used photoresist, as it grants excellent thermal, chemical, and mechanical stability to the resulting lithographic structures, due to the strong crosslinking that occurs during the UV exposure procedure [97], [98]. The various stages that constitute the moulding fabrication procedure can be breakdown in the following steps [97], [99]–[102]:

- I. The photosensitive thin film is either spin-coated or simply put onto the substrate, which is typically a silicon wafer, in order to selectively etch it.
- II. With the use of a photomask, which regulates the light output that reaches certain sections of the thin film, target patterns are formed in the substrate during UV exposure in accordance to the photomask's placement.
- III. When exposed to UV light, the photoresist can be chemically to either dissolve the exposed portions in case it is a positive photoresist or to dissolve the unexposed parts in case it is a negative photoresist; as the SU-8 is a negative photoresist, the exposed portions of SU-8 become stiff and intractable when exposed to radiation, whereas the nonexposed parts are removed.
- IV. The uncured photoresist is washed out afterwards, leaving just the etched pattern.
- V. The master mould is subjected to a surface chemical treatment called silanization to boost the mould's longevity and diminish PDMS adherence to the pattern structures.

Regarding the PDMS processing stage, first the PDMS prepolymer has to be cast on the surface of the master mould and then cured on a hot plate under vacuum conditions. After being fully cured, holes can be punched in the wafer, as these will serve as the inlets and outlets that will be responsible for introducing and collecting fluids in the device [13]. In the last stage, the PDMS wafer with the patterned geometries has to be treated and bonded with a laminate film, generally a glass slide [13]. It is important to create strong and conformal binding between the materials surfaces, with oxygen plasma activation being the most often employed technique for irreversible bonding [103], [104]. Several plasma treatment parameters, including power, oxygen flow, and plasma exposure time, can impact the bonding process, and so they must be manipulated in a way that grants the ideal characteristics for the desired application and design of the microfluidic biochip [103], [104]. Lastly, a conformal contact between the treated surfaces of the PDMS and the laminate surface must be made in order to form the final microfluidic device [13].

### 3. NUMERICAL METHODS

Prior to the experimental approaches, 3D models of two spiral devices were created through a CAD software. Then the designs were transferred to the numerical software COMSOL (version 5.3). The numerical simulations were performed to determine the optimal working conditions (i.e., device geometry, flow rates and fluid viscosities), in order to achieve high isolation efficiency of particles or cells.

In this chapter the numerical procedures and methodology developed are presented into five sections, one dealing with the microfluidic device geometry, followed by a breakdown of the initial considerations regarding the numerical methods, then a section where the numerical model is detailed and finally the numerical simulations are explained.

#### 3.1 Microfluidic Devices Geometries

As illustrated in Figure 3.1, there are many aspects, considerations and constraints that have to be accounted in order to design an efficient CTCs and CAMLs separation microfluidic device. The choice of a passive technique, based in the device geometry, cells size and sample fluid (interest cells and whole blood), lead to the development of inertial based designs with a spiral geometry comprising two inlets and several outlets [17].

Considering the information present in section “Microfluidic lab-on-a-chip cell separation”, chapter 2, among passive separation methods, the spiral inertial technique for particle separation stands apart, having benefits such as ease of use and greater separation resolution when compared to the other technologies. However, cell-to-cell interactions can have a significant negative impact on cell focusing behaviour and, as a result, separation efficiency may be affected, primarily due to the large red blood cells (RBCs) background (45% v/v in blood,  $\sim 10^9$  RBCs/mL) and rarity of the interest CTC and CAML cells ( $\sim 10 - 100$  CTCs and CAMLs/mL of whole blood).

The Dean flow fractioning technique (DFF) configuration is particularly fit to fulfil an efficient separation of these large, rare cells. It has the ability to process large amounts of whole blood samples in a short period of time (3 mL of whole blood in an hour) and to efficiently isolate the CTCs and CAMLs, while also being simple to use and having properties that allow for a good molecular characterization. Thus, a Dean flow fractionation (DFF) method with a double-inlet spiral geometry, will be used in this study in order to isolate the rare and large CTCs and CAMLs from the rest of the blood cells population.

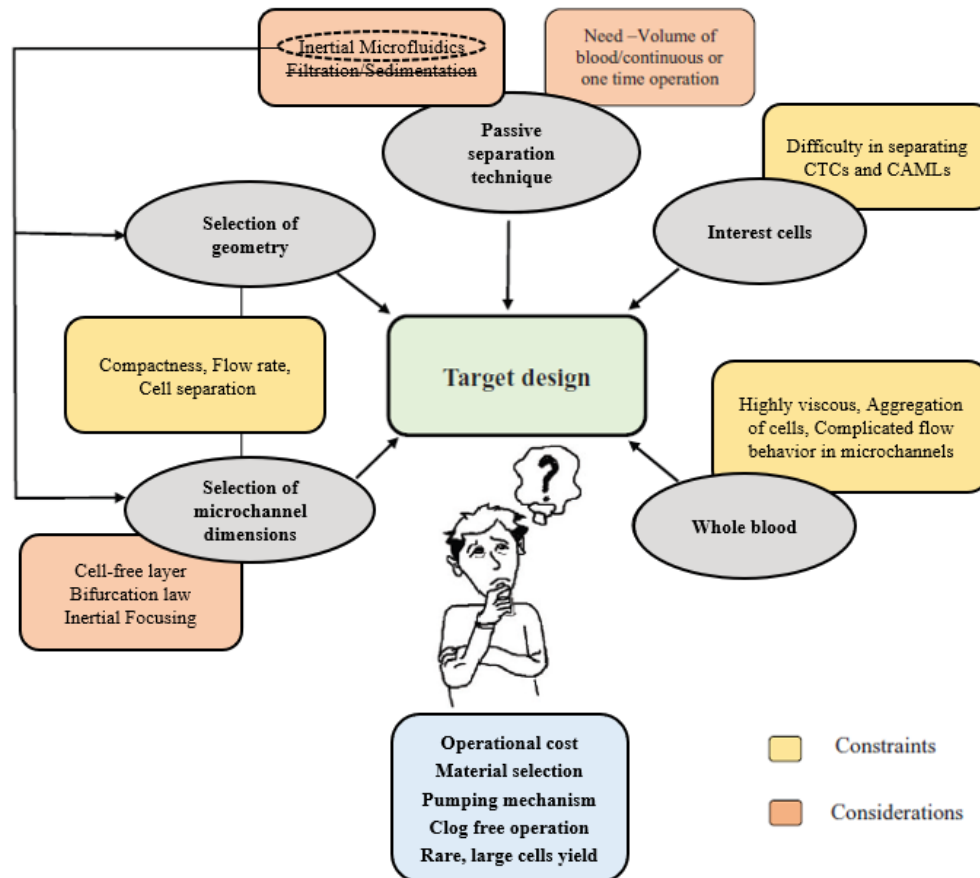


Figure 3.1 - Aspects, considerations and constraints that have to be examined in order to design an efficient passive microfluidic CTCs and CAMLs separation device, adapted from [19].

### 3.1.1 Design of the DFF devices' geometries

The microchannel dimensions impact cell equilibrium locations, and so the spiral devices channels had to be designed in a way that it allows only the bigger target cells to be focused towards the inner wall, while the smaller undesirable particles end up occupying the lateral position near the outer wall. As a result, the target cells will be separated from the rest of the working fluid due to their size and collected via the interest cells outlets, while non-target cells end up being depleted by the waste [105]. In order to fully understand the particle focusing dynamics in a DFF device microchannel, in Figure 3.2 it is possible to observe a schematic illustration of this, which can be breakdown in the stages below [41]:

- i. At the channel's inlet, neutrally buoyant particles are spread at random.
- ii. A severe shear gradient is formed in the vertical direction of the channel due to the asymmetrical parabolic flow profile, with the randomly distributed particles being pushed from the streamlines to the channel top and bottom surfaces by the dominating shear gradient lift force ( $F_{SL}$ ). Near these walls, the particles equilibrate into two broad bands as they experience opposing wall-induced lift force ( $F_{WL}$ ).

- iii. A rotational-induced lift force ( $F_{\Omega}$ ) will then act on the particles, causing them to migrate laterally towards the top and bottom channel walls' centre, forming two focussed streamlines. This lift force  $F_{\Omega}$  is more significant in radially asymmetric (i.e., rectangular) channels since particles spin in the presence of a high shear rate near the channel wall.
- iv. The secondary Dean drag force ( $F_D$ ) increases as flow velocity increases, and particles begin to move towards the inner wall region in the presence of the Dean vortices.
- v. Finally, the equilibrium in the interplay between net inertial lift force ( $F_L$ ) and Dean drag force ( $F_D$ ) results in a single concentrating point, with the particles being inertially focused near the inner sidewall region.
- vi. Larger particles ( $a/D_h > 0.07$ , as  $D_h \approx h$  in a low aspect ratio channel) will focus inertially closer to the inner wall due to increased inertial lift ( $F_L \propto a^4$  vs.  $F_D \propto a$ ), whereas smaller particles will be positioned further away from it, as these different equilibrium positions are greatly dependent on particle size ( $R_f \sim a^2$ ); a decrease in the lift coefficient  $f(Re_c, x)$ , which is dependent on particle position within the channel, can explain the phenomena of particle migration away from the inner wall. It should be noted that, in case there is a further increase in flow velocity, the focused particle streams will move back towards the outer wall due to increasing Dean drag force.

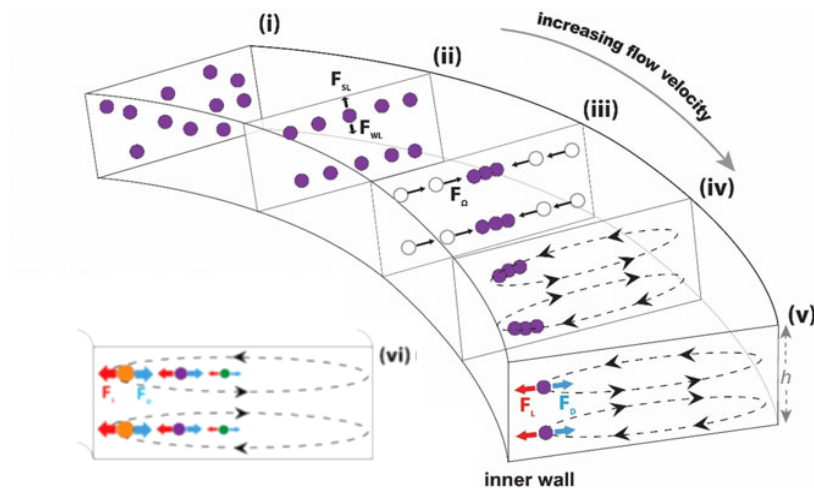


Figure 3.2 - Schematic representation of particle migration dynamics in a DFF device microchannels. Adapted from [49].

The DFF technique is a size-based separation method and, despite both desired cells having large sizes, CTCs and CAMLs differ in size. The particle's size threshold was established in order to define the microchannels' dimensions. As CAMLs have generally a size over 25  $\mu\text{m}$  and CTCs' dimensions may



range between 12  $\mu\text{m}$  and 25  $\mu\text{m}$ , with its average dimension being closer to 20  $\mu\text{m}$ , it was established that the size-based separation would occur for particles with diameters over 20  $\mu\text{m}$ . This means that some smaller CTCs may be lost during the size-based separating procedure, however that threshold will also prevent cells like RBCs ( $\sim 8 \mu\text{m}$ ) and WBCs ( $\sim 7 - 12 \mu\text{m}$ ) from being focused in the interest outlets.

It was also defined that two DFF devices would be used for isolation of the target cells. A device with two outlets will separate cells that are above the proposed particle size threshold (20  $\mu\text{m}$ ) from those that are below (Figure 3.3 (A)), and a device with four outlets that further separates and categorizes the separated cells over its various outlets in accordance to which cell population these belong to, namely if they are CTCs, CAMLs or remains of RBCs and WBCs (Figure 3.3 (B)).

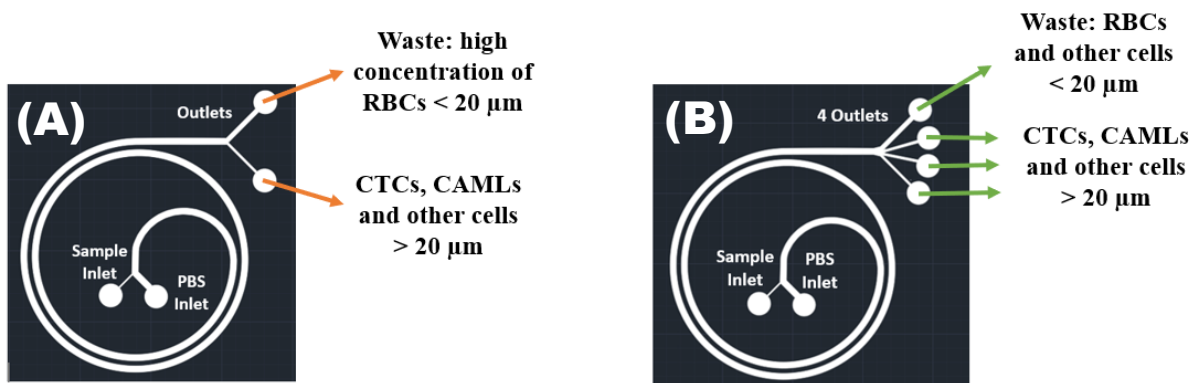


Figure 3.3 - Proposed DFF two-outlets (A) and four-outlets (B) devices for target cell isolation, which differentiate between themselves in the number of outlets and, consequently, on how the particles are isolated and categorized.

A functioning spiral cell sorter must feature a microfluidic channel with a proper depth to allow inertial concentrating of only the target cells near the inner wall, while the remainder of the smaller untargeted cells are scattered and follow the streamline away from the inner wall. Taking into account that particle inertial focusing in microchannels requires that  $R_f > 0.04$  or, equivalently, that  $a/D_h > 0.07$ , the target particles will achieve a tight focusing along the inner wall when satisfying  $a/D_h \sim 0.1$ . Thus, for separating the interest cells ( $\geq 20 \mu\text{m}$ ) from the other blood cells, a spiral CTC isolator should have a channel depth of  $\sim 150-180 \mu\text{m}$ , in accordance with Warkiani et al. [40]. Thus, the two proposed DFF devices have a depth of 170  $\mu\text{m}$  and are composed by a two-loop spiral channel of 500  $\mu\text{m}$  of width.

Warkiani et al. [40], also proposed that the channel length of the CTC isolator should be determined following the Equation (17) for a Reynolds number of  $\sim 20 - 100$ , since the inertial focusing of large particles generally occurs under these conditions. As a result, for both devices, it was defined that the buffer inlet, placed near the inner wall, would have a channel width of 500  $\mu\text{m}$ , while the sample

inlet, placed near the outer wall, would have a channel width of 75  $\mu\text{m}$ , with the purpose of forcing the cells to enter the spiral channel and begin their lateral migration at a similar position, due to the small sample intake.

The lateral position of the cells along the channel width at varied flow rates was used to define the split design and dimensions of the channel outlets. To do that, it was necessary to determine the flow rate range required for 20 and 35  $\mu\text{m}$  diameter particles, such as CTCs and CAMLs, to focus near the inner wall, as well as the flow rate and channel length necessary for blood cells ( $< 12 \mu\text{m}$ ) to complete one Dean cycle. By finding a flow rate and channel length window that meets both of the above-mentioned requirements, it was possible to determine the optimal position of the outlet split through the measurement of the particles distribution over the channel width in several experimental trials. As a result, for the two-outlet device the optimal position for the bifurcation is 150  $\mu\text{m}$  wide for CTC collection outlet near the inner wall (Outlet 2) and 350  $\mu\text{m}$  wide for waste outlet near the outer wall (Outlet 1). In regard to the device with four outlets, the optimal position for the outlet split is 150  $\mu\text{m}$  wide for CTC collection outlet near the inner wall (Outlet 4), 180  $\mu\text{m}$  and 210  $\mu\text{m}$  for Outlets 3 and 2, respectively, and 350  $\mu\text{m}$  wide for waste outlet near the outer wall (Outlet 1).

Thus, in order to the DFF microfluidic devices achieve proper separation between larger CTCs and CAMLS ( $\geq 20 \mu\text{m}$ ) and smaller blood cells, its dimensions were defined as stated on Table 3.1. After having the dimensions determined, it was then possible to create CAD models of the DFF microfluidic devices geometry using *AutoCAD* software. With the final models being presented in Figure 3.4 for the two-outlet device, and in Figure 3.5 for the four-outlet device.

Table 3.1 - Defined dimensions for the main design features of the DFF microfluidic devices that will be used for numerical and experimental trials.

<b>Design Feature</b>	<b>Dimensions projected in the <i>AutoCAD</i> design (<math>\mu\text{m}</math>) two-outlet device</b>	<b>Dimensions projected in the <i>AutoCAD</i> design (<math>\mu\text{m}</math>) four-outlet device</b>
Spiral channel width	500	500
Spiral channel depth	170	170
Buffer inlet channel width	500	500
Sample inlet channel width	75	75
Outlet 1 width	350	350

Outlet 2 width	150	210
Outlet 3 width	-	180
Outlet 4 width	-	150

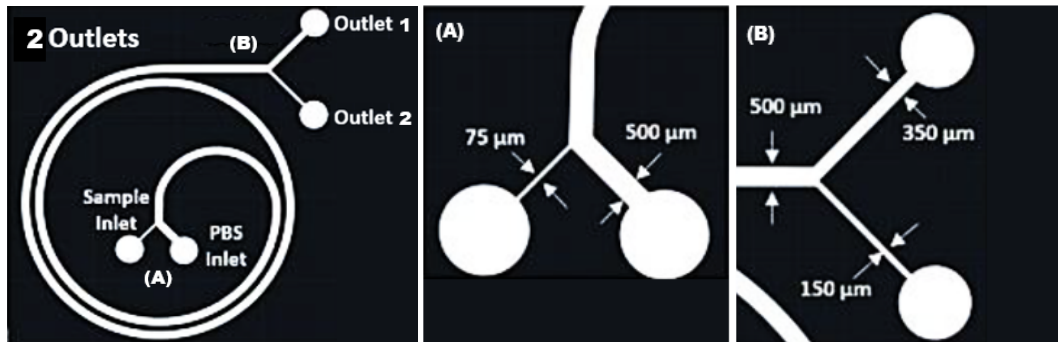


Figure 3.4 - Design in *AutoCAD* software of the proposed two-outlet DFF device with the respective lengths of inlets (A) and outlets (B).

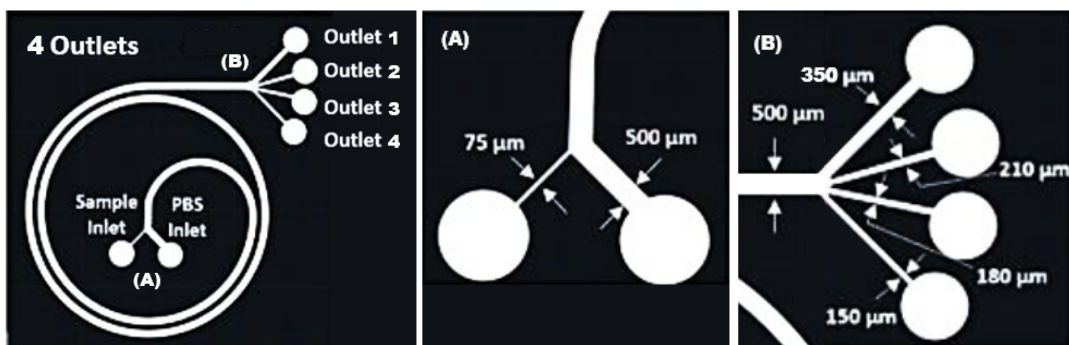


Figure 3.5 - Design in *AutoCAD* software of the proposed four-outlet DFF device with the respective lengths of inlets (A) and outlets (B).

### 3.2 Numerical Model

Taking into account that the objective of this study is to determine the working flow rates for an efficient cells distribution and isolation through the proposed DFF devices, it was used the CFD Module from COMSOL software for the numerical modelling process. The following main steps were necessary to perform:

- I. Defining parameters and component variables;
- II. Geometry creation, import, and manipulation;
- III. Choosing the materials that will be used in the component;
- IV. Defining the physics of the fluid flow in domains and on boundaries (i.e., laminar flow), and coupling that to other physics (i.e., particle tracing physics for fluid flow);

- V. Creating a suitable mesh for the modelling domain, while taking into account the behaviour of the fluid-flow system;
- VI. Solving the equations that explain a system's behaviour, whether stationary or dynamic;
- VII. Gathering and evaluating results.

### 3.2.1 Initial conditions

To successfully run the simulations, it was necessary to define the properties that would influence the model, like the particles characteristics and the fluid that would flow inside the microchannels. As such, the parameters used to represent both the fluid and the particles are exposed in Table 3.2, for a reference temperature of 20°C and a reference pressure of 101.325 kPa (i.e., atmospheric pressure). It should be noted that water (H<sub>2</sub>O) was chosen as the material that would be used to flow in the device due to its characteristics being close to those of the buffer fluid, phosphate buffered saline (PBS). PBS will be used as sheath fluid and to dilute the whole blood sample. This was defined in the “Parameters” section, “Global Definitions” interface and in the “Materials” section in the “Component” interface.

Table 3.2 - Parameters used in all the simulations performed within this study.

<b>Name</b>	<b>Description</b>	<b>Value</b>
dp_rbc	Particle diameter: RBCs	8 µm
dp_wbc	Particle diameter: WBCs	12 µm
dp_ctc15	Particle diameter: Small CTCs	15 µm
dp_ctc20	Particle diameter: Large CTCs	20 µm
dp_caml	Particle diameter: CAMLs	35 µm
rho_rbc	Particle density: RBCs	1130 kg/m <sup>3</sup>
rho_wbc	Particle density: WBCs	1080 kg/m <sup>3</sup>
rho_ctc	Particle density: CTCs	1050 kg/m <sup>3</sup>
rho_caml	Particle density: CAMLs	1050 kg/m <sup>3</sup>
rho_h20	Fluid density: Water	998.23 kg/m <sup>3</sup>
mu_h20	Fluid dynamic viscosity: Water	0.001003 Pa·s

In regard to the models geometries, after having already created the CAD models using *AutoCAD*, both geometries were then imported to COMSOL, in order to study the fluid flow and particles sorting, as can be seen in Figure 3.6.

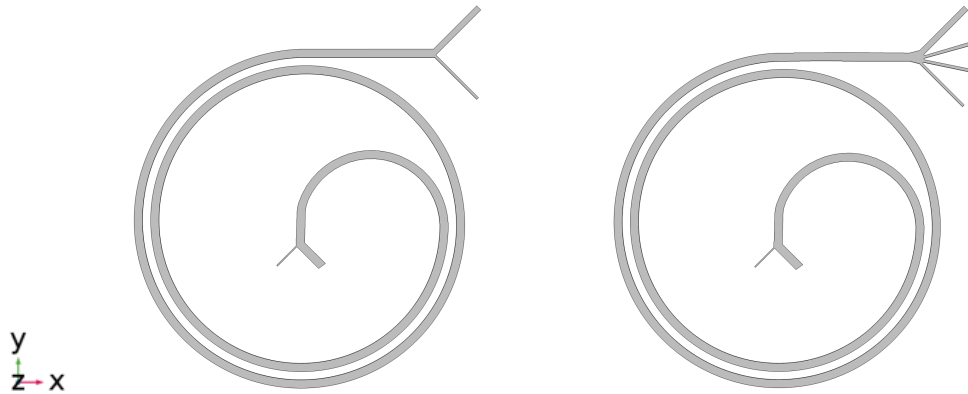


Figure 3.6 - 2D geometry imported to COMSOL of both two-outlet and four-outlet DFF devices that will be used to numerically study fluid flow behaviour and particles distribution.

Since a 2D geometry does not account for the channel depth, a 2D model was not used for this specific study, as the channel depth constitutes an essential variable that deeply impacts the fluid flow and particle sorting behaviour. As such, in order to the inertial focusing take effect and to obtain faithful results, the CAD models were imported into a 3D space dimension. The devices' surface geometries had to be extruded, with the extrusion size correspondent to the channel depth ( $170\ \mu\text{m}$ ). The extruded version of the four-outlet device geometry can be seen in Figure 3.7.

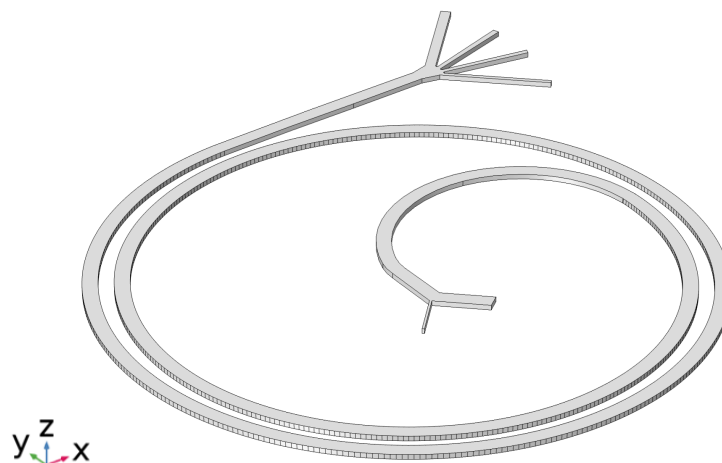


Figure 3.7 – 3D model of the proposed four-outlet DFF device with a channel depth of  $170\ \mu\text{m}$ , which was achieved by extruding the CAD geometry in the “Geometry” interface of COMSOL.

The “Single-Phase Flow” branch included in the CFD Module has a number of subbranches with physics interfaces that describe different types of single-phase fluid flow. One or more of these physics’ interfaces can be used, either singularly or in combination with other physics interfaces for mass transport and heat transfer, for example. In the case of this study, there were two physics’ interfaces that were selected in order to model the fluid flow and particle sorting behaviour in the proposed devices: the “Laminar Flow” interface and the “Particle tracing for fluid flow”.

### 3.2.2 Laminar flow

The “Laminar Flow” physics on COMSOL are used to compute the velocity and pressure fields for the flow of a single-phase fluid in the laminar flow regime (i.e., small to intermediate Reynolds numbers). A flow remains laminar if the Reynolds number is below a certain critical value ( $Re_c \approx 2040$ ), as disturbances have a tendency to grow and cause transition to turbulence at higher Reynolds numbers. As pointed out in section “Flow characteristics”, chapter 2, in microfluidics  $Re_c$  is often less than 100 due to the narrow channel diameters, thus the fluid flow in these numerical models was considered entirely laminar and the “Laminar Flow” interface was used. The equations solved by this physics interface are the Navier-Stokes equations for conservation of momentum (Equation (6)) and the continuity equation for conservation of mass (Equation (1)), and the “Laminar Flow” interface can be used for stationary and time-dependent analyses.

Blood constitutes a steady, incompressible fluid ( $\nabla \cdot \mathbf{u} = 0$ ). When the “Incompressible flow” option is selected on COMSOL, the incompressible form of the Navier-Stokes and continuity equations is applied. For this study, a low Reynolds number was considered thus the inertial terms in the Navier-Stokes equations were neglected.

For the discretization of fluids, the default discretization for “Laminar Flow” interface is P1+P1 elements, which means linear elements for both velocity components and pressure field. However, some higher order interpolations are also available in order to obtain high accuracy for flows with low Reynolds numbers. As a result, the used discretization of fluids was P3+P3 elements (i.e., third order elements for the velocity components and third order elements for the pressure field), as it allowed to obtain more accurate results, namely in what regards to the particles trajectories, as a lower-level discretization resulted in some elements taking a neutral path near the outer wall throughout the entire device.

Lastly, fluid flow with varying flow rates and no slip boundary conditions ( $v = 0$  m/s close to the wall) were applied at the channel inlets and channel wall boundaries respectively. At the outlets, the

pressure was set to zero with no viscous stress on the boundary, which influences the flow behaviour and dictates that it should exit via these outlets.

### 3.2.3 Particle tracing for fluid flow

Dean migration of the fluid elements across the inner and outer wall regions of the devices was obtained using the “Particle Tracing for Fluid Flow” functionality in the COMSOL software.

The trajectory of particles in a fluid may be computed using this interface, which allows the combination of the laminar flow physics with the particle tracing module for computing the flow fields that drive particle motion. For each particle, an ordinary differential equation is solved for each component of the position vector, which means that for each particle in 3D, three ordinary differential equations must be solved. The forces operating on each particle are obtained from the computed fields at the current particle position at each time step, with the particle position being then updated and the procedure being repeated until the simulation's specified end time is achieved. The Particle Tracing interfaces on COMSOL may be used to represent particle motion in laminar flow systems, such as the one under study

In this study particles were considered to have mass, having their movement governed by the Newtonian formulations from classical mechanics. The boundary conditions were imposed on the particles on the surfaces of the geometry in a way that allowed particles to bounce in the channel walls and to freeze in the channel outlets. The particles were uniformly released into the system on a given boundary, which in this case were the channel inlets. To properly emulate the whole blood sample characteristics, it was necessary to guarantee a large RBCs background, as well as to assure the rarity of the cancer cells; to do that, it was defined that a specific number of particles that inherit the whole blood cells' diameter and density would be used in the simulations, with these cell-like particles being introduced into the device via the sample channel inlet (i.e., outer inlet). As such, their initial position was set as “Projected plane grid” and the number of particles per release was set to 30 for the RBCs-like particles, 12 for the WBCs-like particles, 4 for the CTCs-like particles and 4 for the CAMLs-like particles, which met the above-mentioned requirements and did not demand an extreme number of computational resources.

In regards to the inertial forces that will act on the model, the drag force and the lift force were applied, as these play an essential role in the particle focusing dynamics. Two wall induced lift forces had to be used in this study, with one of them being responsible for the up and down parallel boundaries, while the other was tasked with the sidewalls' parallel boundaries. For example, in Figure 3.8 it is possible to observe the sidewalls' parallel boundaries of the inner wall (in colour orange) and of the outer wall (in colour pink).

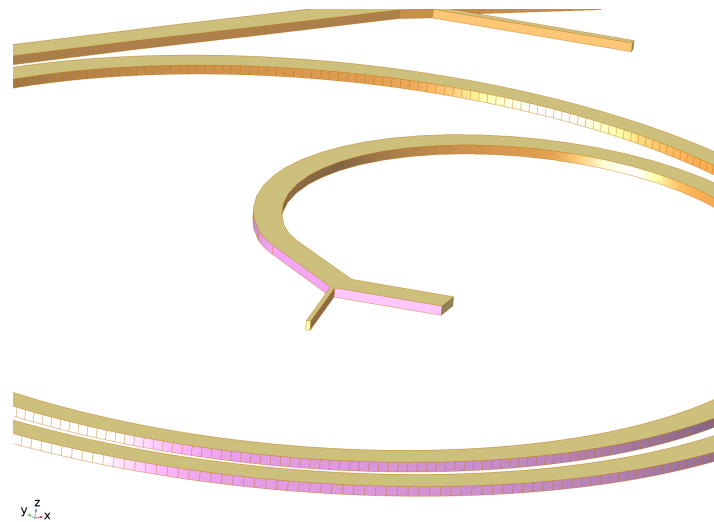


Figure 3.8 - Sidewalls' parallel boundaries of the inner wall (in colour orange) and of the outer wall (in colour pink), which influence the wall induced lift force.

### 3.2.4 Mesh properties

Creating an appropriate mesh for the Finite Element Analysis (FEA) simulations is an important aspect of the simulation process, and it is critical for getting representative results, but the need of high computing power should be taken into consideration.

The mesh used in a fluid flow simulation is determined by the fluid flow model and the simulation's accuracy requirements. There can be cases in which the requirement of accuracy in the results can limit the maximum element size, as a fine element grants results with more precision, and other where the results do not need to be highly precise but in which the fluid flow model may require a fine resolution in order to converge. In order to cover these different mesh needs, there are a number of different mesh types and meshing strategies for fluid flow modeling in COMSOL.

For most types of geometries, unstructured meshes that are generated via free-meshing methods can be used, as the highly automated mesh-generating algorithms can frequently produce a mesh that covers all of the geometry. For the proposed 3D DFF devices, the default COMSOL's physics-controlled unstructured mesh with coarse element size presented a reasonable average element quality to perform the simulations and the computational demands were not too substantial. For these conditions, using the four-outlet DFF model, there was a number of mesh elements of 92803, with the maximum element size being 236  $\mu\text{m}$  and the minimum element size being 70.9  $\mu\text{m}$ ; all the mesh properties can be observed in Table 3.3. In Figure 3.9 it is possible to observe the mesh configuration for the proposed four-outlet DFF device, especially the outlets area.



Table 3.3 – Mesh conditions for the four-outlet DFF model.

Mesh Properties	Value
Number of elements	92803
Minimum element quality	0.065
Average element quality	0.5192
Element volume ratio	0.001559
Mesh volume	1.148E10 $\mu\text{m}^3$

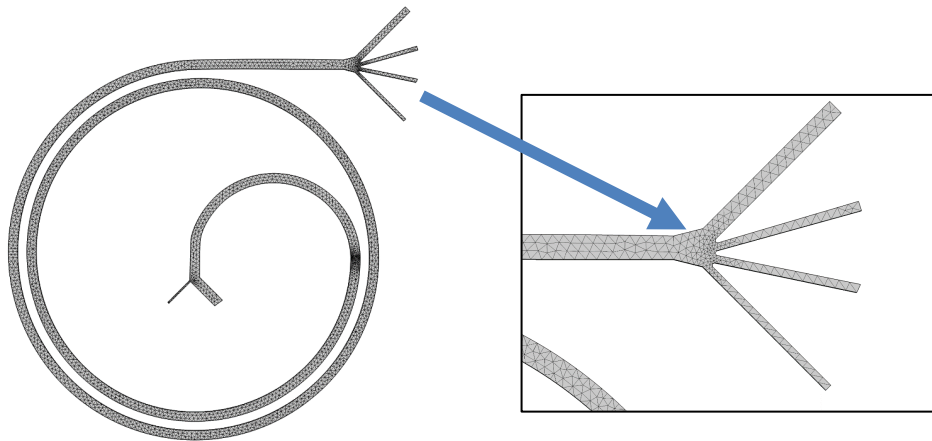


Figure 3.9 - Mesh configuration for the proposed four-outlet DFF device. Detailed view of the outlets region.

### 3.3 Numerical Simulations

In order to determine the fluid flow and particles distribution behaviour in the proposed DFF devices, two studies had to be executed, namely a stationary domain study step to solve the modelled fluid flow, and a time-dependent study based on the solutions obtained from the stationary one, in order to retrieve the particles trajectories under the influence of both drag and lift forces.

In regard to the stationary study (“Stationary” study interface on COMSOL), this was performed by solving the “Laminar Flow” physics interface that had been set up earlier. As a result, the velocities fields that take place on the device’s channels were obtained, making it possible to observe and determine the flow velocity in the various regions of the microchannel. This allowed to obtain information and graphs about the velocity magnitude that is verified in various points and planes of the microchannels, as shown in Figure 3.10 for the inlet are of the four-outlet DFF model.

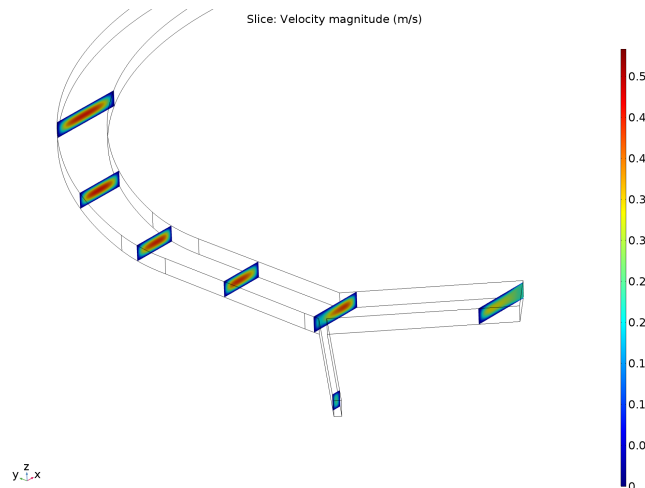


Figure 3.10 - Example of the velocity magnitude graphs that can be obtained by performing a stationary study in COMSOL using the proposed four-outlet DFF model.

Finally, the time-dependent study (“Time Dependent” study interface on COMSOL) was performed by solving the “Particle Tracing for Fluid Flow” physics interface. In order to perform this study, its variables had to be based on the solutions obtained in the stationary study, thus using the computed velocity field obtained in the first study to generate plots of the estimated particles trajectories along the microchannels, as shown in Figure 3.11 for the four-outlet DFF model.

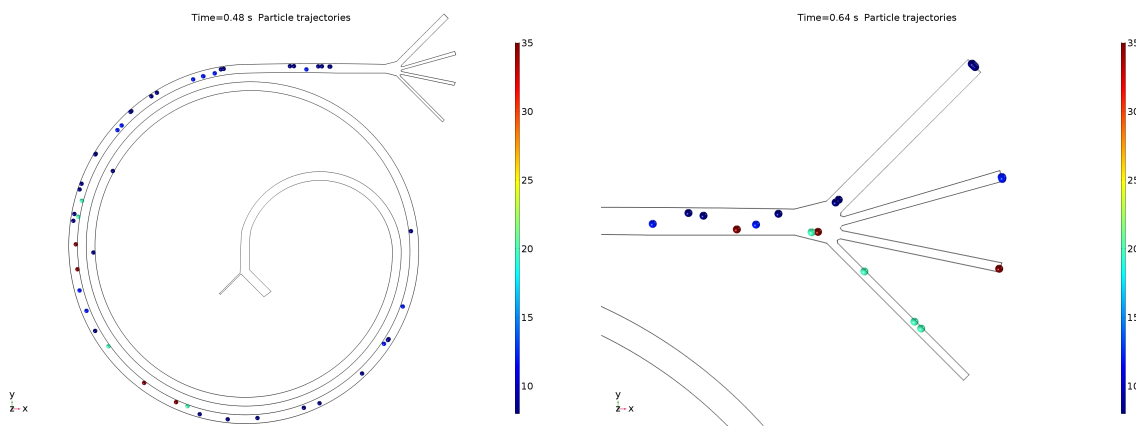


Figure 3.11 - Example of the particle trajectories graphs that can be obtained by performing a time dependent study in COMSOL using the proposed four-outlet DFF model.

### 3.4 Data Treatment

With the numerical simulations solved, the last stage of the numerical procedures consisted on the post-processing of all the information and data that was possible to retrieve from the studied model.

The information was obtained via the “Results” interface of COMSOL with data regarding the velocity fields and the particle trajectories (Figure 3.10, Figure 3.11). Besides that, in order

to be able to determine the separation efficiency of the numerical models, using COMSOL it was possible to determine how many particles follow through each outlet, while also being able to distinguish the different types of particles in accordance to their size.

This data was then treated with the purpose of calculating the particles separation efficiency for both two-outlet and four-outlet DFF models. Various sample and buffer flow rates were used, multiple simulations were run using both models and, as a result, several velocity and particles distribution results were obtained. In order to determine which setting granted the best outcome (i.e., most particles separation efficiency), it was also necessary to perform a comparison between all the results obtained.

## 4. EXPERIMENTAL SETUP AND PROCEDURES

This chapter describes and explains the experimental procedures and relevant stages to perform all the experiments in order to evaluate the microfluidic devices and the final microfluidic system for the isolation of CTCs and CAMLs from blood samples. Thus, the chapter explained in detail the following stages of the experimental procedures:

- Microfluidic devices fabrication;
- Microfluidic devices priming;
- Microfluidic setup and experimental tests;
- Working fluid preparation and handling;
- Sample processing;
- Cell counting process and data treatment.

### 4.1 Microfluidic Devices Fabrication

The two devices designs described in section “Design of the DFF devices geometries”, chapter 3, were fabricated by replica mould, i.e., manufactured by soft lithography. The respective master mould was obtained by photolithography technique. Regarding the master mould processing, this was done in a clean room facility, where a thin layer of the photoresist AZP4110 (indicated for high device depths) was spin-coated onto the silicon (Si) wafer. The devices designs were then transferred to the wafer by direct UV exposure using a Direct Write Laser Lithography machine, as seen in Figure 4.1. After the wafer pattern steps of resists development, etching and optical inspections were performed until the desired depth of the devices (170  $\mu\text{m}$ ), and respective final master mould, was obtained. Wafer dicing using the Automatic Dicing Saw machine was also performed, with the purpose of having a better handling of the wafer when performing (PDMS) replica devices fabrication. After this stage, the moulds were silanized with some droplets of trichlorosilane (tridecofluoro-1, 2, 2 tetrahydrooctyl-1-trichlorosilane) (97%, Sigma Aldrich) during a period of twenty minutes, in order to increase its lifespan and aid in the posterior PDMS detachment stage.

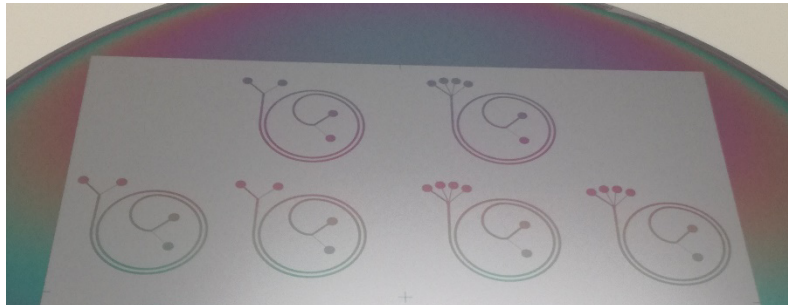


Figure 4.1 - Devices design being transferred to the wafer by photolithography.

In regards to the microfluidic devices fabrication, this should take place in a clean, lab environment, with most of the necessary procedures being done over a laboratory workbench. First, the PDMS (Sylgard 184 Silicon Elastomer kit, Dow Corning) mixture was performed by properly mixing the base and the curing agent at the ratio of 10:1 (w/w). The base-cure agent ratio must be thoroughly respected in order to guarantee that the PDMS chip has the intended characteristics. Both were mixed vigorously in a reservoir until the mixture present a white appearance. Then it was degassed using a vacuum desiccator and a vacuum pump, in order to remove all the created bubbles (Figure 4.2 (I)). The PDMS was cast over the Petri dish with the master mould in it and posteriorly, to achieve proper PDMS casting conditions, it was again degassed in the vacuum desiccator. After all air bubbles being released from the PDMS, the Petri dish was placed in the oven for PDMS polymerization at 65 °C for two hours (Figure 4.2 (II)).

Following that, the PDMS was carefully unmoulded using a sharp blade and spatulas, which requires extreme caution since a mishandle of the blade can cause the wafer to get cut or cracked, which might negatively impact the cell separation process, as well as damage the master mould (Figure 4.2 (III)). Both devices' inlets and outlets holes were made in the appropriate locations using a 1.5 mm puncher (Kai Medical). The PDMS devices replicas were cleaned with scotch tape in order to remove any PDMS debris and to ensure the proper bounding (Figure 4.2 (IV)). Afterward, irreversible bounding was achieved through surface activation of clean glass slides and PDMS replicas by an exposure to an oxygen plasma environment inside the chamber of a plasma cleaner (Harrick Plasma) (Figure 4.2 (V)). Finally, the bounding surfaces of glass slide and PDMS replica were brought into contact and, to reinforce the bounding, the devices were again placed in the oven at 65°C for thirty minutes. The various stages of the microfluidic devices' fabrication procedure can be observed in Figure 4.2.

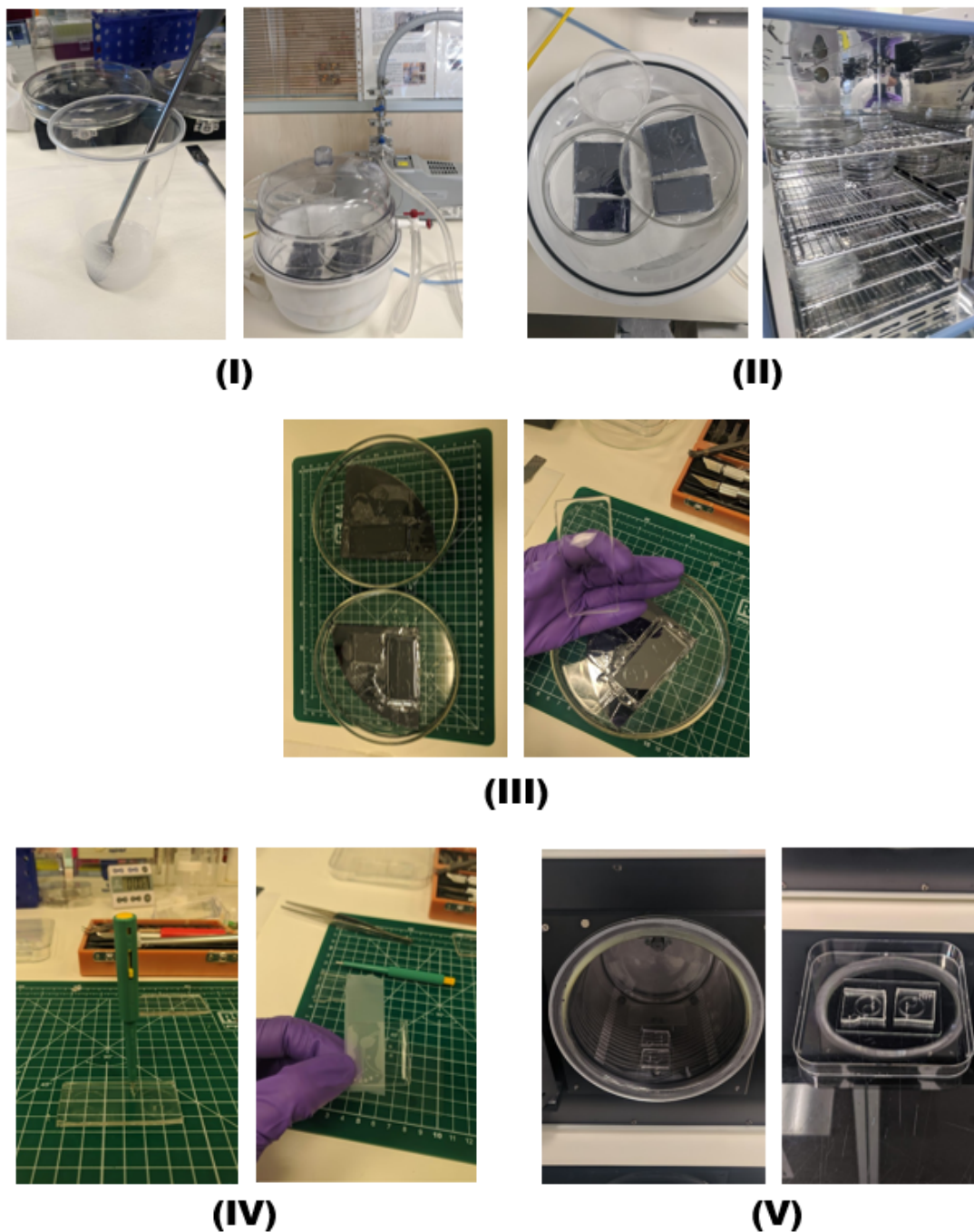


Figure 4.2 - Microfluidic devices' fabrication procedure: (I) PDMS mixture process, (II) PDMS casting over the Petri dish with the master mould and PDMS polymerization in the oven at 65 °C for two hours, (III) detachment of the PDMS replica from the Petri dish with the master mould, (IV) punching of inlet and outlet holes in the PDMS wafer, (V) bonding of the PDMS wafer and glass slide surfaces.

## 4.2 Microfluidic Devices Priming and Tubing

After having the PDMS devices permanently bonded to the slide glass, all inlets and outlets were connected with 1.5-mm-diameter EVA plastic tubing with 25 cm of length and syringe tips on the other end of the tubing, in order to connect the devices to the syringe pumps and to the outlets reservoirs. Following, passivation must be done with the new microfluidic devices, in order to reduce the sample clinging to the devices' walls. Thus, a filtered sample of Pluronic F-127 (Sigma Aldrich) at 1% (w/v) in phosphate buffer saline (PBS) was run inside the spiral chip at a flow rate of 250  $\mu\text{L}/\text{min}$  for around five minutes, in order to get rid of persisting air bubbles within the system and to guarantee that the device's channels are hydrophobic, as can be seen in Figure 4.3. The microfluidic systems were then sterilized with 70% (vol/vol) ethanol at a flow rate of 500  $\mu\text{L}/\text{min}$ . In order to remove some ethanol waste and the remaining air bubbles, a 60 mL syringe was loaded with sterile and filtered PBS, and a final washing run in the microfluidic system was performed at 500  $\mu\text{L}/\text{min}$ .



Figure 4.3 - Pumping of a filtered sample of Pluronic F-127 (Sigma Aldrich) at 1% (w/v) in PBS to the spiral chip at a flow rate of 250  $\mu\text{L}/\text{min}$  for around five minutes, in order to get rid of persisting air bubbles within the system and to guarantee that the device's channels are hydrophobic.

## 4.3 Microfluidic Setup and Experimental Tests

The experimental setup (Figure 4.4) needed to test both two-outlet and four-outlet devices comprises two syringe pumps, calibrated accordingly to the brand and volume of the used syringes, with one being connected to the sample intake (outer inlet) and the other connected to the sheath buffer intake (inner inlet). In regard to the outlets of the devices, these were connected to sterile 15 mL falcon tubes with the purpose of collecting the recovered samples and, posteriorly, counting the cells in them.

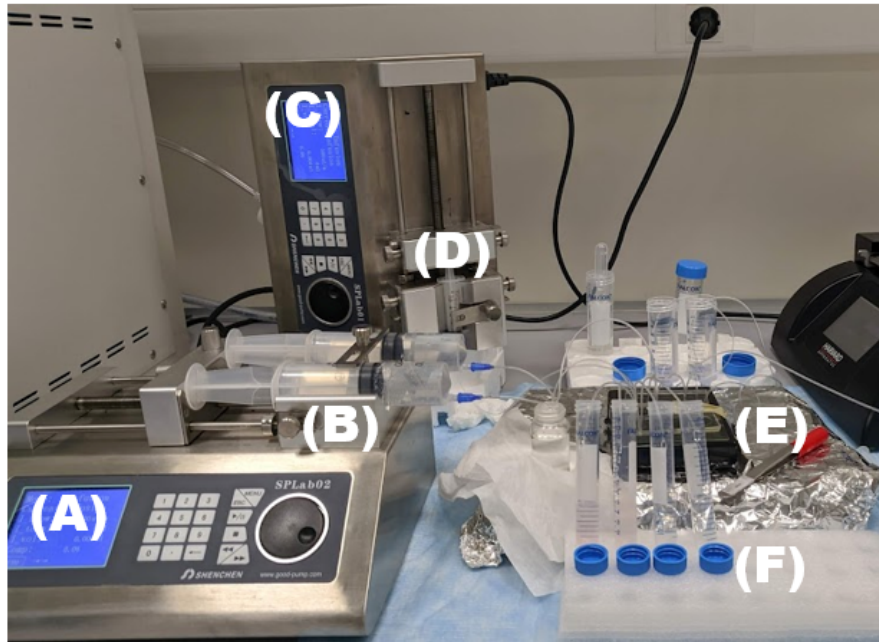


Figure 4.4 - Setup of the microfluidic system, with the syringes (B - buffer syringe, D - sample syringe) properly mounted on the syringe pumps (A and C), the tubing connected to the inlets and outlets of the biochip (E), and the sample collection conical tubes (F) set to receive the microchannels' outputs.

In case of the two-outlet microfluidic device, its outlet 1 (the outlet most distant from the centre of the device) is classified as “waste”, as the non-interest cells and the largest volume of the inlet sample comes through it. Oppositely, the outlet 2 recovered samples are considered as the interest collection, which means that these are the interest cells that were focused next to the inner wall of the device. Regarding the four-outlet microfluidic device, it is comprised of the same inlet configuration, however four outlets were designed in order to efficiently isolate and categorize the cells by size. The outlet 1 is also considered as “waste”, while the other outlets (2, 3 and 4) are the interest ones.

Cell isolation experiments will be performed in the two microfluidic devices that were developed and numerical tested under several conditions and with different samples. The set of experiments are organized as follow:

- A. Flow rates optimization for both devices tested individually for a threshold size of 20  $\mu\text{m}$  (Figure 4.5).
  - Two-outlet device and four-outlet device run separately;
  - This experiment was performed using a single sample composition, of a cell suspension of both DU-145 and giant cells (orange) in diluted whole blood.



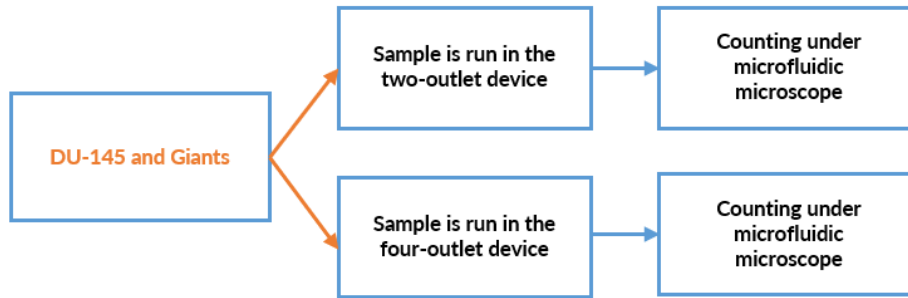


Figure 4.5 - Schematic representation of the experiments (A), as DU-145 and giant cells were suspended in diluted blood and run separately in the two-outlet and in the four-outlet devices, with the cells isolated in each outlet being counted under fluorescence microscope.

B. With the optimal flow rate, the devices were tested in sequence with different cells size and different cells number per sample to determine rare cells isolation efficiency (Figure 4.6).

- Two-outlet device and four-outlet device in sequence, with intermediate centrifugation step.
- Prostate cancer cell line DU-145 and *in vitro* generated giant cells at cell number of 100, 500, 1000 and 2000 were suspended in diluted blood samples;
- This experiment was performed using three different sample compositions: cell suspension of DU-145 (yellow), cell suspension of giant cells (green) and cell suspension with both DU-145 and giant cells (orange).

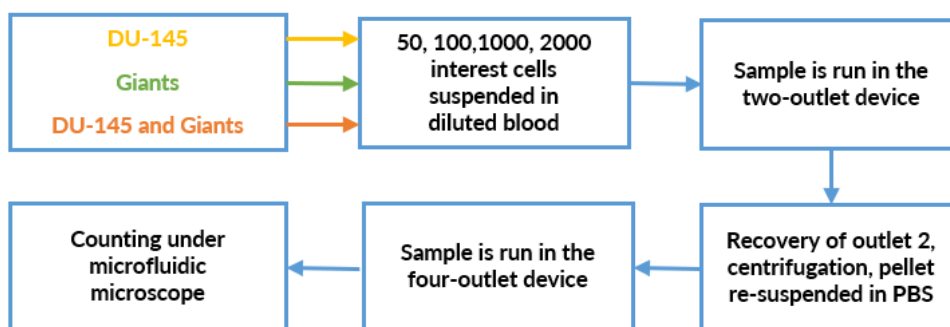


Figure 4.6 - Schematic representation of the experiments (B), as 50, 100, 1000 and 2000 DU-145 or/and giant cells suspended in diluted blood were run into both two-outlet and four-outlet devices, with an intermediate centrifugation stage, with the cells isolated in each outlet being counted under fluorescence microscope.

C. Proof-of-concept of the proposed microfluidic system, using a cell suspension analogous to the pathological samples (Figure 4.7).

- Two-outlet device and four-outlet device in sequence, with intermediate centrifugation step;
- Prostate cancer cell line PC-3 and *in vitro* generated giant cells at cell number of 100 were suspended in diluted blood samples;

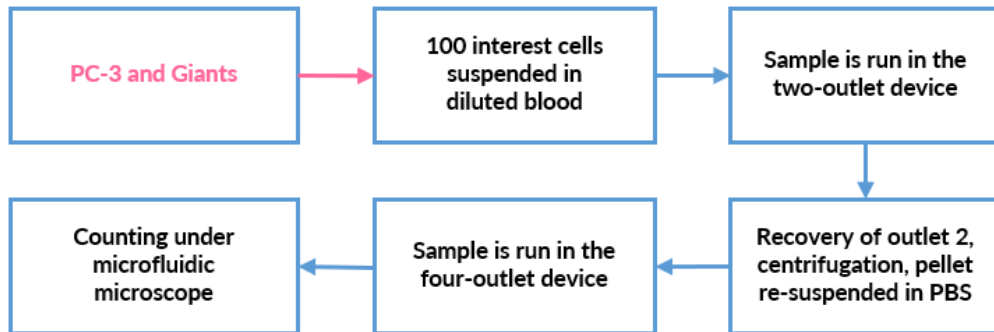


Figure 4.7 - Schematic representation of the experiments (C), as 100 PC-3 cells and giant cells suspended in diluted blood were run into both two-outlet and four-outlet devices, with an intermediate centrifugation stage, with the cells isolated in each outlet being counted under fluorescence microscope.

#### 4.4 Working Fluid Preparation and Handling

In order to be able to successfully run the experiment, the working fluid must first be prepared. As such, it is necessary to have a sample fluid with characteristics that resemble those of a pathological sample, allowing it to have a close behaviour in action, and thus its constituents must be thus carefully selected. For this study, with the goal of having a reliable sample, a suspension of prostate cancer cell lines, *in vitro* generated giant cells and healthy blood samples were used, as seen in Figure 4.8.

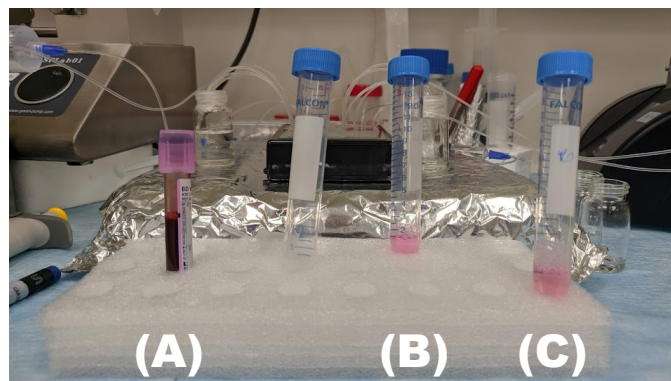


Figure 4.8 - For this study, a reliable sample consisted on a suspension of prostate cancer cell lines (B), *in vitro* generated giant cells (C) and healthy blood samples (A) was used, as their combination has characteristics that resemble those of a pathological sample.

The prostate cancer cells lines, respectively DU-145 and PC-3, were properly cultured with supplemented medium with 10% (v/v) fetal bovine serum and 1% of penicillin-streptomycin. Cells were maintained at 37 °C in an atmosphere of 5 % CO<sub>2</sub> until confluence. These cells, were obtained from Leibniz Institute DSMZ-German Collection of Microorganisms and Cell Cultures Gmb (Germany), went through a testing and authentication process, as cells were monitored by microscopy and tested for mycoplasma contamination. The mean diameter of the DU-145 cells (pictured in Figure 4.9 (A)) was about  $18 \pm 3 \mu\text{m}$ , while the PC-3 cells (pictured in Figure 4.9 (B)) had a mean diameter of  $22 \pm 3.4 \mu\text{m}$ , both in suspension.

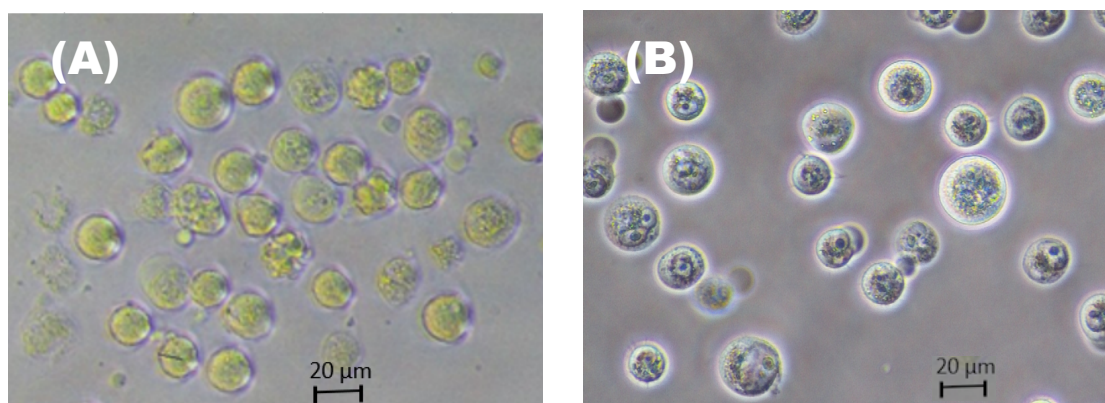


Figure 4.9 - DU-145 cells (A) and PC-3 cells (B) observed via a microscope. Objective lens of 20x.

To generate the giant cells (depicted in Figure 4.10), i.e. *in vitro* differentiation of healthy human monocytes, healthy blood samples from Hospital of Braga were collected for monocytes isolation using a density gradient method. Briefly, a RosetteSep™ human monocyte enrichment cocktail kit (StemCell, Cambridge, MA) and a Histopaque-1077 (Sigma-Aldrich) density gradient medium were used to isolate a monocyte-enriched layer from blood. Then, the monocytes were seeded in a 24-well culture plate supplemented with a RPMI medium with 25% fetal bovine serum (FBS) and 1% penicillin, and differentiated for ten days in an environment with a combination of hM-CSF (50ng/mL) + IFN- $\gamma$  (100U/mL) + IL-3 (10ng/mL) cytokines. After the culture processes, giant cells were removed using a cell scraper and collected for subsequent microfluidic studies. The size of the generated giant cells was evaluated through the use of *ImagerJ* software, and its mean size in suspension was about  $34.8 \pm 7.9 \mu\text{m}$ .

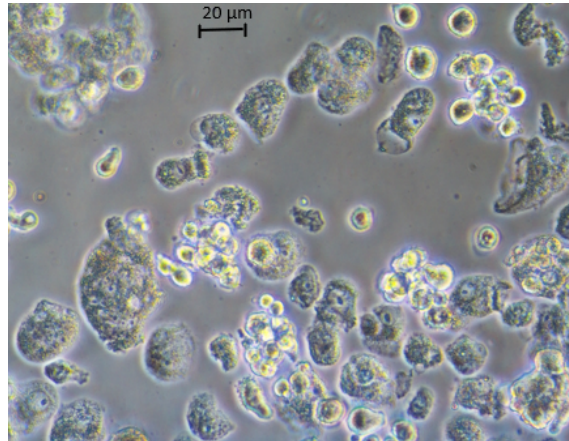


Figure 4.10 - Giant cells observed via an electronic inverted fluorescence microscope. Objective lens of 20x.

With the purpose of being able to better distinguish the cells during the cell counting process, before proceeding to sample fluid preparation, the cancer and giant cells have to go through a staining procedure, with nuclei or viability markers (DAPI, 1mg/mL and Calcein-AM, 12.5 μg/mL, respectively, Sigma Aldrich), which will allow to execute a proper evaluation of the separation efficiency of the devices.

The working fluids were properly prepared by diluting healthy blood samples 2.5x and by adding the respective number of cancer cell lines suspension, with the final result being a sample fluid such as the one depicted in Figure 4.11. A total sample volume of 3 mL was used to perform each experimental test, as well as 60 mL of sheath buffer (PBS).



Figure 4.11 - Sample fluid consisting on a suspension of diluted healthy blood and a certain number of cancer cell lines suspension.

#### 4.5 Sample Processing

To run the experiment, a 60 mL syringe filled with running buffer (PBS) is connected to the sheath inlet of the spiral chip. This buffer will play a role in the cell focusing process, as it contributes to forcing the different cells to move to certain areas of the microchannels and, thus, to different outlets in accordance to their dimensions. A 5 mL syringe containing the working fluid is loaded into a second

syringe pump, having its flow rate set in accordance to predetermined data. This syringe pump must be put in a vertical position, as presented in Figure 4.12, in order to prevent sample sedimentation. The syringe must be at roughly the same height as the rest of the system to achieve consistent pressure conditions throughout the entire experiment.

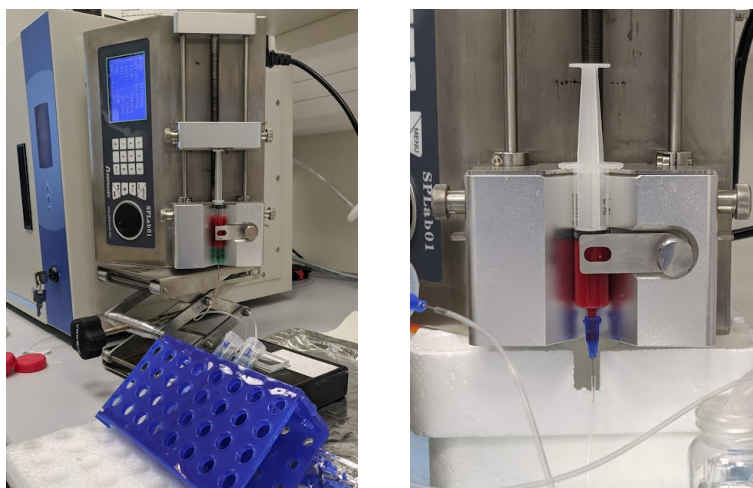


Figure 4.12 - 5 mL syringe containing the working fluid loaded into a syringe pump and connected to the biochip using tubing and a precision tip.

The prepared sample and buffer (PBS) were injected into the microfluidic devices at different flow rates, with the working fluid being pumped in either at 100 or 200  $\mu\text{L}/\text{min}$ , and with the buffer fluid being pushed into the device at either 800, 1000, or 1200  $\mu\text{L}/\text{min}$  in case the biochip had two inlets and two outlets, and at either 500, 600, 800, 1000, or 1200  $\mu\text{L}/\text{min}$  in case the biochip had two inlets and four outlets. After the sample pumping is finished and the cells are properly separated, exemplified in Figure 4.13, the buffer is kept being pumped into the system for a few minutes in order to clean the device and to remove any remaining sample fluid that may be contained therein.

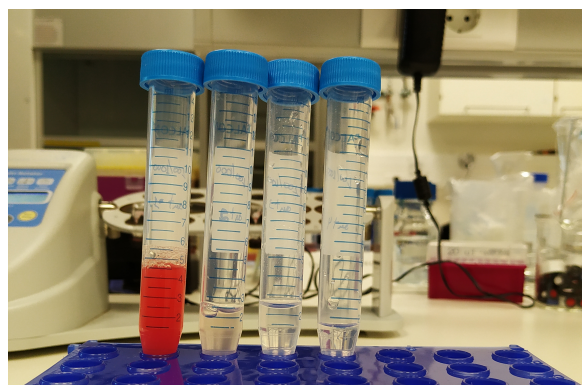


Figure 4.13 - Differentiated fluids collected in outlets 1 to 4 (from left to right, respectively) in one of the experimental runs performed with the four-outlet device.

#### 4.6 Cell Counting Process and Data Treatment

The fluid samples collected from the devices' outlets are then counted and evaluated. First, a centrifugation process at 1200 rpm for 50 minutes at room temperature was performed (Figure 4.14 (A)), with the resulting pellet (Figure 4.14 (B)), which contains the interest cancer cells, being re-suspended in PBS for sample evaluation under microscope. The re-suspended samples were seeded in a 96 well plate and, via fluorescence visualization using an electronic inverted fluorescence microscope, the isolated cells were characterized and counted (Figure 4.14 (C)). A control sample of the inlet was also performed.

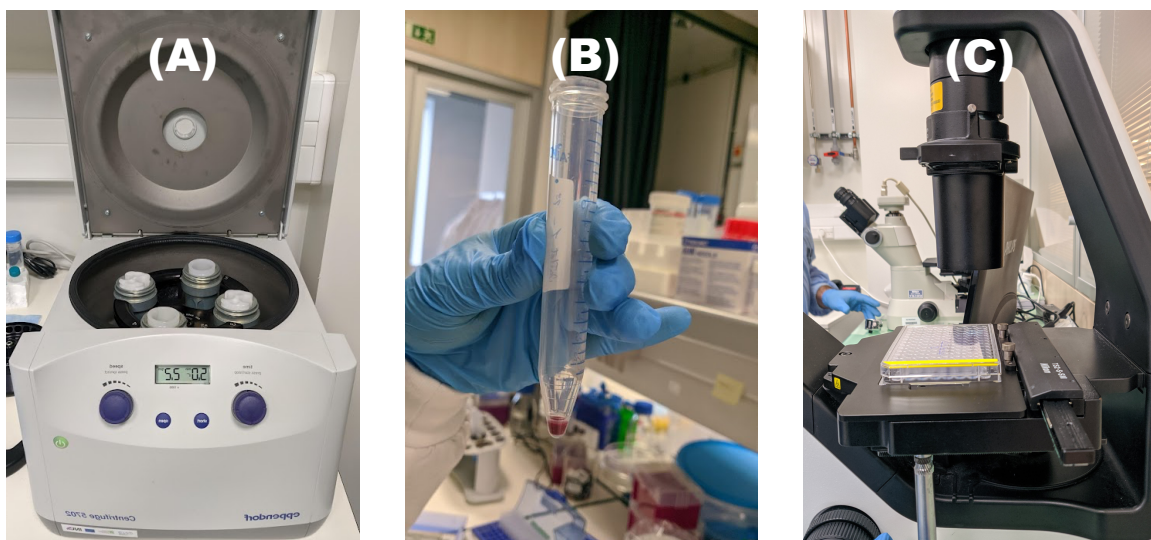


Figure 4.14 - Parts of the cell counting process, namely the centrifugation of the collected fluid samples (A), the pellet containing the interest cancer cells (B), and the characterization and counting of the isolated cells using an electronic inverted fluorescence microscope (C).

In order to evaluate the experimental efficiency of the microfluidic system, the results obtained and the data taken from the experimental trials has to be thoroughly analysed. As such, for the experiment described above, the isolation efficiency, i.e. recovery rate, and the depletion were quantified in accordance with Equations (18) e (19), respectively.

$$\text{Isolation efficiency (\%)} = \frac{n^{\circ} \text{ of isolated cells}}{n^{\circ} \text{ of cells in inlet}} \times 100 \quad (18)$$

$$\text{Depletion (\%)} = \frac{n^{\circ} \text{ of cells in inlet} - n^{\circ} \text{ of isolated cells}}{n^{\circ} \text{ of cells in inlet}} \times 100 \quad (19)$$

## 5. RESULTS AND DISCUSSION

This chapter summarises the key findings of this dissertation through numerical approaches and experimental assays. Some brief considerations about the proposed DFF devices properties and procedures are described, then the numerical and flow rates optimization process is detailed. The fabrication of the PDMS devices was also discussed, and the final microfluidic system proposed for the isolation of CTC and CAMLs was tested, with its results being presented and discussed.

### 5.1 DFF Devices Design

As defined previously two DFF devices were developed in order to perform rare blood cells separation. Both devices design consisting of a two-loop spiral microchannel, which has a width of 500  $\mu\text{m}$  and a depth of 170  $\mu\text{m}$ , in order to allow inertial focusing of the target cells (i.e., diameter over 20  $\mu\text{m}$ ) near the inner wall, while the remainder of the smaller untargeted cells are scattered and follow the streamline away from the inner wall.

The proposed geometries have been designed with two inlets for sample and buffer intake (with a width of 170  $\mu\text{m}$  and 500  $\mu\text{m}$ , respectively). Both devices differentiate between themselves at the region of the outlets. In the device with a two-outlet configuration, the outlet channel width is 350 and 150  $\mu\text{m}$ , for outlet 1 and 2 respectively, and in the device of four-outlet configuration the outlet channel width is 350, 210, 180 and 150  $\mu\text{m}$ , for outlet 1, 2, 3 and 4 respectively. In both devices, the working principle focuses the interest cells into the inner outlets, as a result of the channel dimensions, geometry design and flow rates ratio between the sample and buffer inlet. A description of the main dimensions was already presented in Table 3.1, section “Design of the DFF devices’ geometries”, chapter 3, for both DFF devices.

### 5.2 Numerical Simulations

With the devices’ geometry defined, it was numerically tested and flow rates optimization performed for both DFF devices. First a numerical flow rates optimization procedure was developed and, based on the results obtained, an experimental flow rates optimization procedure was also performed.

5.2.1 Numerical flow rates optimization

According to the work of Hou et al. [12], for a close design of DFF devices the optimal flow rate ratio between the sample fluid and the buffer fluid is one to nine, respectively [12]. As such, it was defined that for both devices models the sample inlet fluid would be tested at flow rates of 100 or 200  $\mu\text{L}/\text{min}$ , while the buffer inlet fluid would be tested at flow rates of 600, 800, 1000 and 1200  $\mu\text{L}/\text{min}$ . These numerical experiences were performed using the particle properties for RBCs, WBCs, large CTCs and CAMLs described in Table 3.2, section “Design of the DFF devices’ geometries”, chapter 3.

Regarding the model of the two-outlet device, a total isolation in outlet 2 of the particles with sizes over 20  $\mu\text{m}$  was achieved for the flow rates of 100/1000  $\mu\text{L}/\text{min}$  and 200/800  $\mu\text{L}/\text{min}$ , respectively sample/buffer. With that flow rates the cells with dimensions under 20  $\mu\text{m}$  are all depleted in outlet 1. In regards to the other combinations of sample and buffer flow rate, some of them resulted in a decrease in the isolation efficiency of the interest cells (200/600  $\mu\text{L}/\text{min}$  and 100/800  $\mu\text{L}/\text{min}$ ), and an increase of contamination with non-desired particles (< 20  $\mu\text{m}$ ) in the interest outlet was also verified for the flow rates of 100/1200  $\mu\text{L}/\text{min}$  and 200/1000  $\mu\text{L}/\text{min}$  (Figure 5.1). Thus, for the two-outlet device model, the flow rates of 100/1000  $\mu\text{L}/\text{min}$  and 200/800  $\mu\text{L}/\text{min}$  were considered the optimal values.

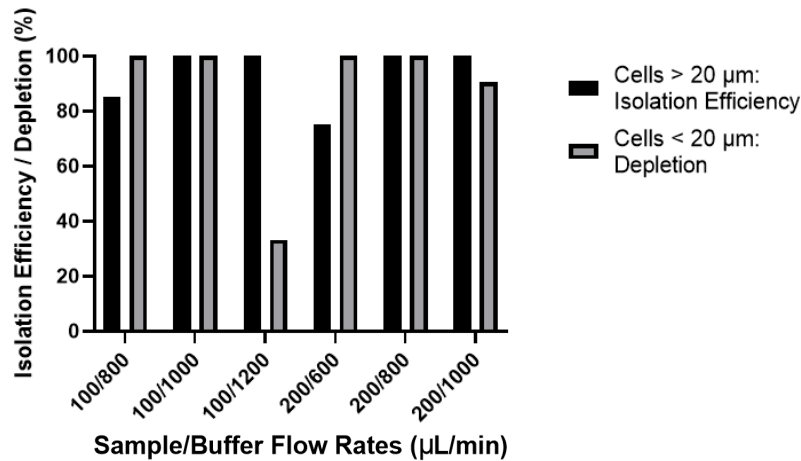


Figure 5.1 - Average numerical isolation efficiency of cells > 20  $\mu\text{m}$  and depletion of cells < 20  $\mu\text{m}$  obtained for the two-outlet device model using different flow rates of sample/buffer ratio.

In case of the four-outlet device model, only with the sample flow rate of 100  $\mu\text{L}/\text{min}$  and a buffer flow rate of 800  $\mu\text{L}/\text{min}$ , it was possible to achieve a proper isolation of the interest cells in the inner outlets (outlets 3 and 4, respectively CAMLs and CTCs) and a depletion of the other cells in the outer outlets (outlets 1 and 2). For all the other flow rate combinations (100/1000  $\mu\text{L}/\text{min}$ , 100/1200  $\mu\text{L}/\text{min}$ ,



200/600  $\mu\text{L}/\text{min}$ , 200/800  $\mu\text{L}/\text{min}$  and 200/1000  $\mu\text{L}/\text{min}$ ), a contamination of the inner outlets with particles with a size under 20  $\mu\text{m}$  was verified, with total contamination of the interest outlets being verified for the 100/1200  $\mu\text{L}/\text{min}$  flow rate ratio (Figure 5.2). Thus, the flow rates of 100/800  $\mu\text{L}/\text{min}$  were considered the optimal values for the four-outlet device model, and in Figure 5.3 it is possible to visualize the different particles separated over the four-outlet device model outlets.

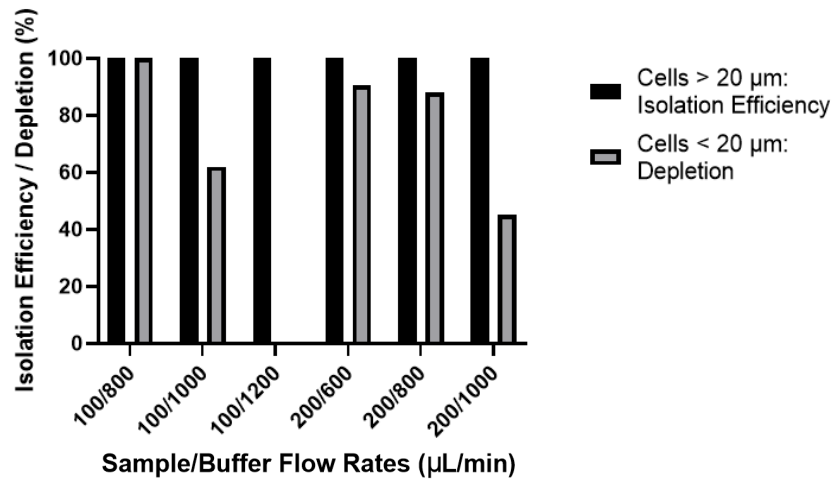


Figure 5.2 - Average numerical isolation efficiency of cells > 20  $\mu\text{m}$  and depletion of cells < 20  $\mu\text{m}$  obtained for the four-outlet device model using different flow rates of sample/buffer ratio.

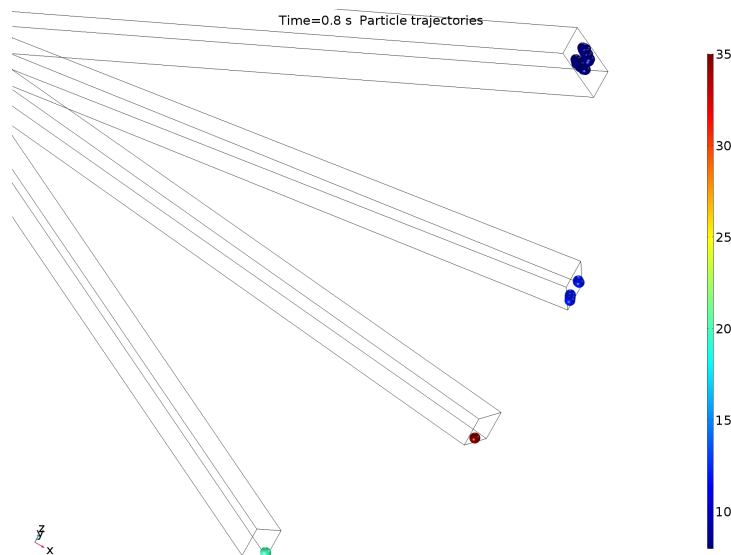


Figure 5.3 - Cells > 20  $\mu\text{m}$  (red and green, CAMLs and CTCs, respectively)  $\mu\text{m}$  isolated in the inner outlets of a four-outlet device after the execution of a numerical simulation on COMSOL using a flow rate ratio of 100/800  $\mu\text{L}/\text{min}$ .

The velocity magnitudes in the plane XY and in the plane YZ can be seen in Figure 5.4 for the two-outlet device and in Figure 5.5 for the four-outlet device. The highest velocities in the two-outlet device are registered in the outer outlet microchannel, while in the four-outlet device model it is observed throughout the centre of the device model main channel.

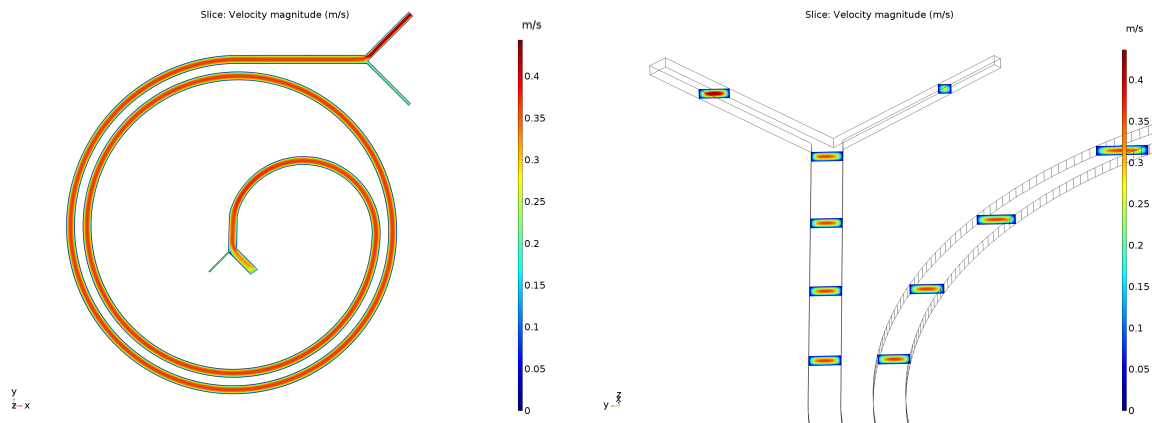


Figure 5.4 - Velocity magnitude graphs obtained in COMSOL for the XY and YZ planes of the two-outlet device.

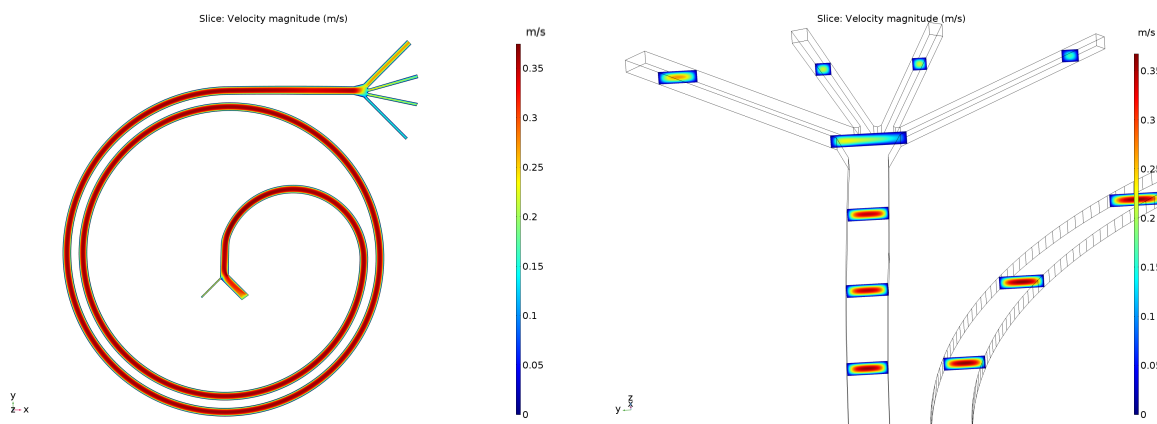


Figure 5.5 - Velocity magnitude graphs obtained in COMSOL for the XY and YZ planes of the four-outlet device model.

### 5.3 DFF Devices Fabrication and Working Principal

With the devices' geometry determined and optimized, it was then possible to proceed to the master mould fabrication, which subsequently led to the PDMS device replicas production. As described in the section "Microfluidic Devices Fabrication", chapter 4, the master mould of the devices was fabricated by photolithography and, in order to be able to reproduce the results obtained numerically achieve in the experimental trials, the efficiency that was obtained in the numerical simulations, it was

fundamental to verify if the design features dimensions of the fabricated PDMS wafers matched those of the proposed geometries defined on *AutoCAD*. Thus, the wafers with the designs patterned were measured by using a microscope, with especial attention paid to the PDMS replicas depth, as the correct depth of 170  $\mu\text{m}$  is a fundamental parameter in the separation process. All projected and real dimensions are virtually similar for both devices' replicas, as disclosed in Table 5.1, including the PDMS device channel depth.

Table 5.1 - Comparison between the design features dimensions of the fabricated wafers and the PDMS devices depth of the proposed geometries defined on *AutoCAD* for both devices.

Design Feature	Two-outlet Device		Four-outlet Device	
	Dimensions projected in the <i>AutoCAD</i> design ( $\mu\text{m}$ )	Pattern designs measurements ( $\mu\text{m}$ )	Dimensions projected in the <i>AutoCAD</i> design ( $\mu\text{m}$ )	Pattern designs measurements ( $\mu\text{m}$ )
Spiral channel width	500	499	500	499
Spiral channel depth	170	169.8	170	170.2
Buffer inlet channel width	500	500	500	499.2
Sample inlet channel width	75	74.8	75	74.5
Outlet 1 width	350	351	350	350
Outlet 2 width	150	149.5	210	209
Outlet 3 width	-	-	180	179
Outlet 4 width	-	-	150	149.8

Prior to the beginning of the experimental trials, simple tests with rigid polymethylmethacrylate (PMMA) particles were performed to ensure that the devices' working principal was occurring, i.e. isolating the interest cells to the desired outlets. In order to do so, a sample of PMMA microparticles suspended in dextran 40 (Dx 40) was processed in the devices (Figure 5.6). PMMA microparticles ( $\rho_{\text{PMMA}} = 1200 \text{ kg/m}^3$ ) with dimensions of 6  $\mu\text{m}$ , 10  $\mu\text{m}$ , 20  $\mu\text{m}$  and 60  $\mu\text{m}$  were used, with the concentration for the 6  $\mu\text{m}$ , 10  $\mu\text{m}$  and 20  $\mu\text{m}$  particles being 2% (w/v) and for the 60  $\mu\text{m}$  particles being 1% (w/v).

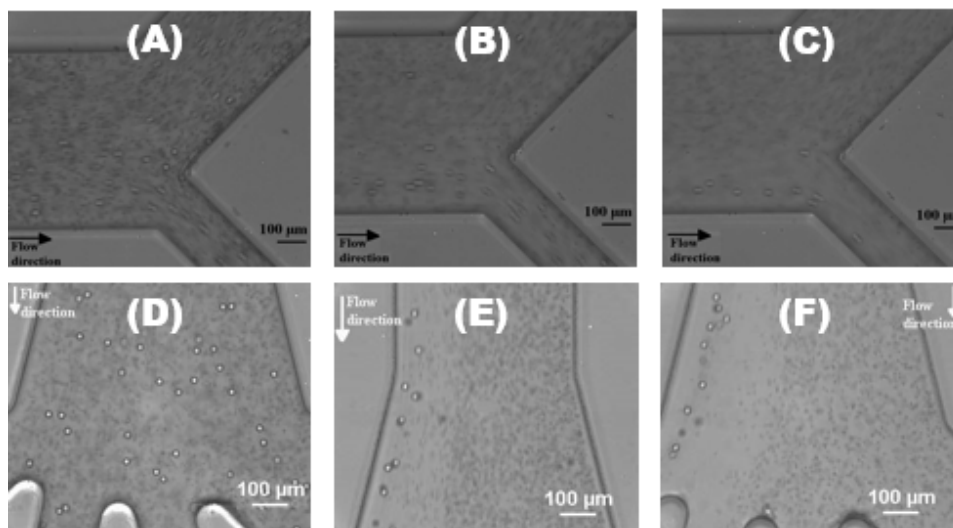


Figure 5.6 - Images obtained from the recorded videos from the DFF devices. A to C for the two-outlet device (A) stabilized and well distributed flow of the sample; B and C the larger particles been focus to the outlet 2. D to F the four-outlet device, D the flow of stabilized and well distributed sample; E and F observation of the focusing of the larger particles to the inner outlet. Objective lens of 20x.

The tests with the PMMA particles demonstrated that the larger ones are being focused close to the inner wall, while smaller particles were recirculated back to the outer wall. As a result, the PDMS devices' design was confirmed to efficiently conduct dean flow-focusing and, thus, could be utilized with biological samples.

#### 5.4 Experimental Flow Rates Optimization

With the results of the numerical flow rates optimization, the same flow rates were tested experimentally for an efficient cell separation process using the proposed DFF devices.

In regards to the particles that were used in the experimental procedures, with the purpose of mimicking the rare cancer cells characteristics, cancer cell lines and *in vitro* generated giant cells, both with size and shape properties close to the ones of CTCs and CAMLs were used as sample working fluid. Cell lines DU-145 and PC-3 were utilized as a substitute for the CTCs, while the giant cells were used as a substitute for the CAMLs. According to the measurements performed by using *ImageJ* software, the average cell size of DU-145 cells is  $15.2 \pm 3.0 \mu\text{m}$  (Figure 5.7 (A)). This means that these particles are under the defined devices' particle size threshold and, as such, it was not expected that these cells could be efficiently retrieved and separated in the devices' outlet 2 or 3 and 4. In spite of that, both devices were expected to properly separate and recover in the interest outlets the great majority of giant cells, sized  $34.8 \pm 7.9 \mu\text{m}$  (Figure 5.7 (B)), as well as most of the PC-3, sized  $22.1 \pm 5.0 \mu\text{m}$  (Figure 5.7 (C)).

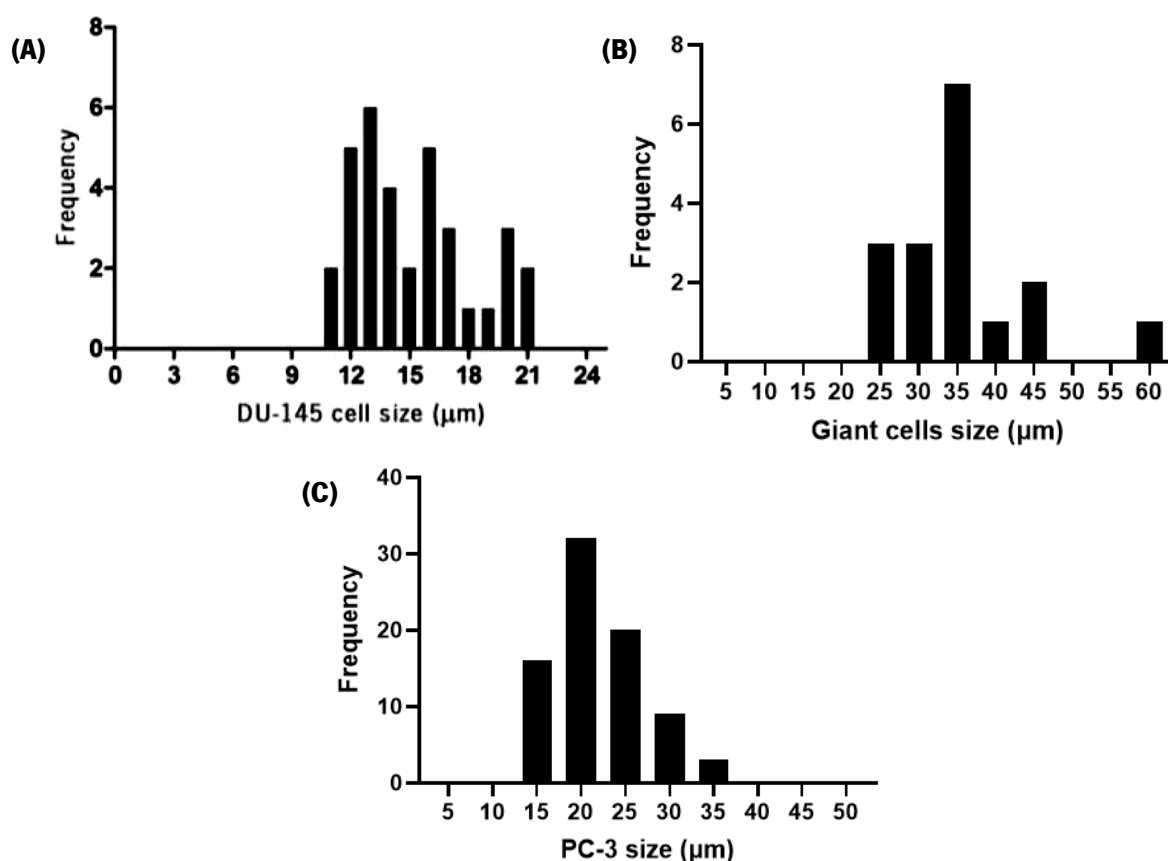


Figure 5.7 - Size distribution of (A) DU-145 cells (min = 11.008  $\mu\text{m}$ , max = 21.075  $\mu\text{m}$ , mean = 15.1974  $\mu\text{m}$ , SD = 2.954  $\mu\text{m}$ ), (B) giant cells (min = 23.766  $\mu\text{m}$ , max = 58.137  $\mu\text{m}$ , mean = 34.821  $\mu\text{m}$ , SD = 7.938  $\mu\text{m}$ ) and (C) PC-3 cells (min = 12.625  $\mu\text{m}$ , max = 22.093  $\mu\text{m}$ , mean = 15.1974  $\mu\text{m}$ , SD = 5.033  $\mu\text{m}$ ).

Thus, for the flow rates optimization, a cell suspension of *in vitro* generated giant cells and cell line DU-145 in diluted whole blood was used to evaluate the isolation efficiency of each PDMS device, and injected into the devices at flow rates of 100 or 200  $\mu\text{L}/\text{min}$ . The buffer or sheath fluid (PBS) flow rates injection would be 800, 1000 and 1200  $\mu\text{L}/\text{min}$  for the two-outlet device, while for the four-outlet device the flow rates tested would be of 600, 800, 1000  $\mu\text{L}/\text{min}$ , the same values used in the numerical simulations. This procedure corresponds to the set of experiments A that was introduced in section “Microfluidic Setup and Experimental Tests”, chapter 4, and is represented in Figure 4.5.

In regard to the two-outlet DFF device, with the sample fluid being pumped at 100  $\mu\text{L}/\text{min}$  and by changing the buffer fluid flow rate, the best separation efficiency results were achieved for the 1000  $\mu\text{L}/\text{min}$  (buffer), with a recovery efficiency of the giant cells of 92.80% and 11.90% for the DU-145 cells, which corresponds to a depletion of 88.10% (Figure 5.8). From these results, it's possible to verify that the separation efficiency was very low for the DU-145 cells, as these cells have smaller size in relation to the imposed threshold of 20  $\mu\text{m}$  and, thus, they were mostly discarded through the waste, outlet 1.

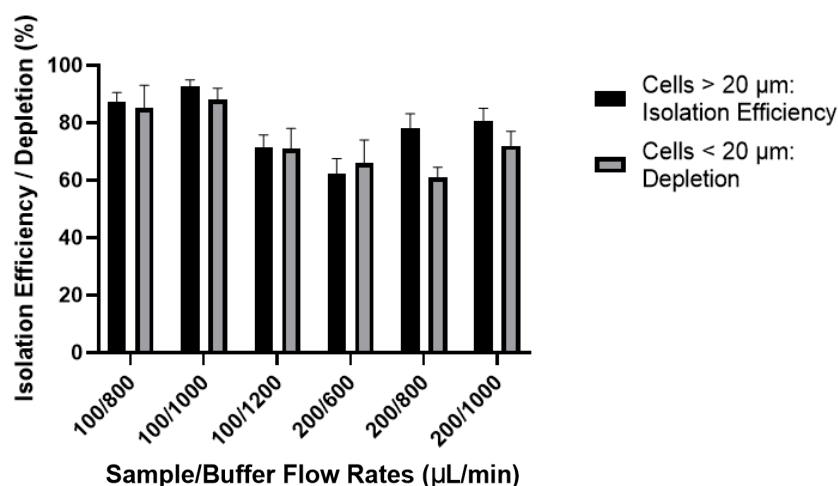


Figure 5.8 - Average isolation efficiency of cells > 20 µm (giant cells suspended into PBS) and depletion of cells < 20 µm (DU-145 cells suspended into PBS) obtained for the two-outlet device using different flow rates of sample/buffer ratio. Results are displayed as Mean + SD of 3 independent experiments.

A substantial decrease in cell recovery for particles with dimensions larger than the size cut-off is observed when the buffer flow rate was raised to 1200 µL. This may indicate the presence of an instable flow inside the devices, which causes instability in the cell focusing process. As a result, a decrease in the isolation of cells with dimensions above 20 µm was also verified, as well as an increase of DU-145 cells recovery through the outlet 2. If instead there is an increase of the sample fluid flow rate to 200 µL/min, there is a substantial increase in the recovery of cells under than 20 µm, which leads to an increasing of recovered sample contamination with other blood cells population (RBCs and WBCs). As such, taking into account that the best giant cells separation efficiency was obtained for the flow rates pairing of 100/1000 µL/min, then these are the optimum values for the two-outlet device. These results confirm the ones obtained numerically for the two-outlet device.

Similar conclusions were also reached for the four-outlet device, as again the optimum performance for the DFF device is achieved by employing a flow rate ratio of 100/1000 µL/min for sample and buffer, respectively. In this device, for an efficient separation process, the interest cells with dimensions above 20 µm (i.e., giant cells) should be collected in either outlet 2, 3 or 4, with the smaller, non-interest cells (i.e., DU-145) being collected in outlet 1. As observed in the Figure 5.9, 93.79% of the larger cells were retrieved in the interest outlets, while only 10.50% of the DU-145 particles reached these outlets, with 89.50% being depleted. Besides this, it should also be noted that raising the sample fluid flow rate to 200 µL/min, resulted in a decrease of separation efficiency of the large cells, with the particles size under 20 µm once again contaminating the interest outlets.

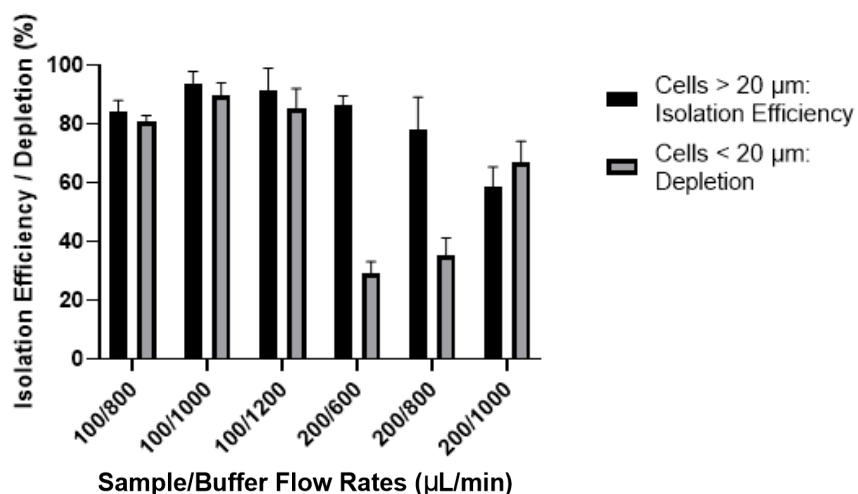


Figure 5.9 - Average isolation efficiency of cells > 20 µm (giant cells suspended into PBS) and depletion of cells < 20 µm (DU-145 cells suspended into PBS) obtained for the four-outlet device using different flow rates of sample/buffer ratio. Results are described as Mean + SD of 3 independent experiments.

Thus, in order to achieve the best interest cell isolation efficiency, flow rates of 100/1000 µL/min, respectively sample/buffer, are required for both devices proposed in this study. In case of the four-outlet device, numerically the best efficiency was obtained for the flow rates ratio of 100/800 µL/min. Numerically, that flow rate provides a clear separation of the CTC population through the outlet 4 from the CAMLs, which follow through the outlet 3. However, that perfect separation and isolation between both cells was not observed in any experimental assay. The explanation for this might be related to the cell-to-cell interactions. The number of cells used for the simulations represents just a fraction of the number of cells that constitute an experimental sample fluid, or else it would be necessary an enormous amount of computational power to run the simulations with a larger number of cells. As a result, the cellular interactions that can be verified in the experimental procedures cannot be replicated completely using the numerical models. Thus, considering that the cellular interactions influence the cells isolation results, a new set of experimental assays was performed, as described in the next section. Besides this, it was identified the need of obtaining recovered samples free of other blood cells population, as these contaminated the interest outlets. This led to the development of the strategy described in the next section.

## 5.5 Microfluidic System for Rare Cells Isolation

With the optimal flow rate for both devices determined, the performance of both microfluidic PDMS devices in isolating rare cancer cells was experimentally tested in order to determine the recovery rates of CTCs and CAMLs through a combination of both devices, two-outlet and four-outlet, in sequence.

As such, the prostate cancer cell line DU-145 and *in vitro* generated giant cells at a cell number of 100, 500, 1000 and 2000 were suspended in diluted whole blood from healthy individuals and processed through the proposed microfluidic system at the pre-determined ideal flow rate combination of 100/1000  $\mu\text{L}/\text{min}$ . The sample flows within the two-outlet device, with the recovered sample of outlet 2 being collected. Then it was centrifuged at 1200 rpm for five minutes, with the resulting pellet being reduced and re-suspended in 1000  $\mu\text{L}$  of PBS. The resulting cell suspension was then run through the four-outlet device and the different resulting fluids in each outlet were recovered and counted by observation using a fluorescence microscope. This procedure corresponds to the set of experiments B, represented in Figure 4.6, that was introduced in section “Microfluidic Setup and Experimental Tests”, chapter 4.

In the three sets of experiments performed, it was possible to verify that the DU-145 depletion rate stayed considerably high independently of the number of suspended cells used, depletion rates of 92%, 76%, 96% and 84% were obtained for the samples containing respectively 50, 100, 1000 and 2000 suspended cells (Figure 5.10 (A)). Thus, a high depletion of cells with sizes under 20  $\mu\text{m}$  was obtained with the proposed microfluidic system.

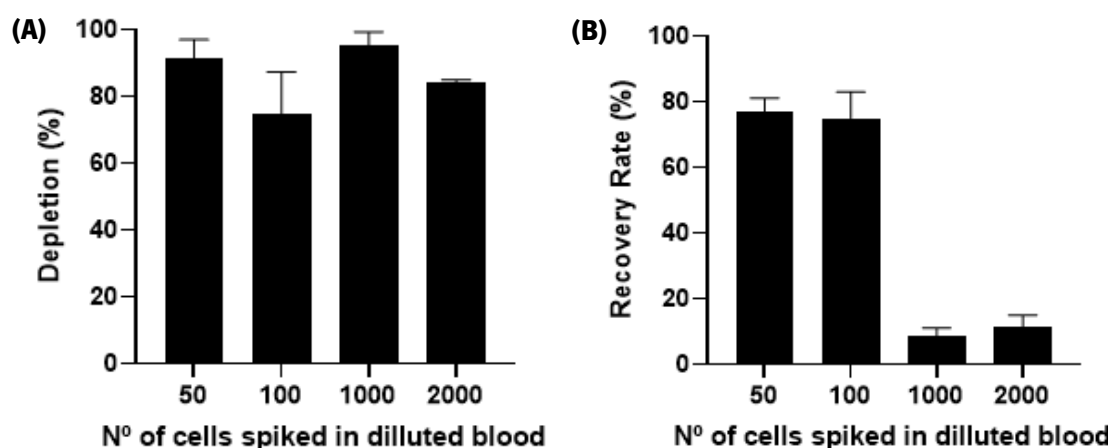


Figure 5.10 - Average depletion of cells < 20  $\mu\text{m}$  of three different experiments, where 50, 100, 1000 and 2000 DU-145 cells were suspended in diluted blood (A) and average recovery rate of cells > 20  $\mu\text{m}$  of three distinct experiments, where 50, 100, 1000 and 2000 giant cells were suspended in diluted blood. These were processed by the two-outlet device at flow rates of sample/buffer of 100/1000  $\mu\text{L}/\text{min}$ . The recovered outlet 2 fluid was then centrifuged, reduced to 1000  $\mu\text{L}$  and run in the four-outlet device with flow rates of sample/buffer of 100/1000  $\mu\text{L}/\text{min}$ . Results are described as Mean +SD of 3 independent experiments.

In regard to the giant cells, they were expected to be isolated from the rest of the sample cells since the majority of these cells has dimensions above the established size threshold (20  $\mu\text{m}$ ). Thus, when a sample with only suspended giant cells was run through the system, it was expected that these



cells would be isolated in the outlet 2 of the two-outlet device and, after the centrifugation process, separated into the outlets 3 and 4 of the four-outlet device.

Considering the results of the three sets of experiments performed, the average recovery rate of the giant cells processed through the PDMS microfluidic system when a low number of suspended cells was around 76% for both 50 and 100 cells (Figure 5.10 (B)). However, for a higher number of suspended cells (1000, 2000) the average recovery rate dropped abruptly, as just 10% of cells were successfully recovered in the outlets of the four-outlet device. This considerable reduction in the recovery efficiency may be attributed to the fact that the giant cells, with their varying lengths and irregular morphologies, tend to aggregate and promote cell-to-cell interactions. As a result, an entrapment may be formed in the devices' outlet areas, which may affect the focusing of the giant cells and lead to a decrease in recovery efficiency.

Samples with both DU-145 cells and *in vitro* generated giant cells were processed in the proposed system. As such, both cell populations circulated in the microfluidic system simultaneously. Considering the three sets of experiments performed, there were variations in the values of recovery efficiency of the giant cells and DU-145 depletion when compared to the tests performed with the suspended cells separately. This implies that the combination of DU-145 cells and giant cells may modify the equilibrium positions of cells, impacting the depletion of cells with sizes below 20  $\mu\text{m}$  and the recovery rates of cells with sizes above 20  $\mu\text{m}$ .

The average recovery rate of the giant cells was high when the sample contained a low number of suspended cells (72.67% for 50 cells and 83.33% for 100 cells), while for a higher number of suspended cells the average recovery rate dropped considerably (19.20% for 1000 cells and 12.80% for 2000 cells) (Figure 5.11). As for the DU-145 depletion rate, it increased as samples with a greater number of suspended cells were used, as depletion rates of 66.00%, 76.67%, 90.00% and 94.82% were obtained for the samples containing 50, 100, 1000 and 2000 spiked cells of each population, respectively (Figure 5.11).

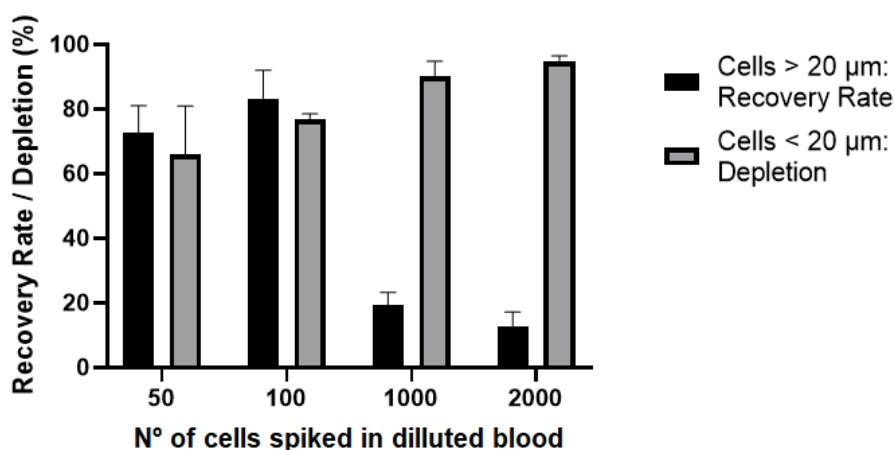


Figure 5.11 - Average recovery rate of cells > 20 µm and average depletion efficiency of cells < 20 µm of three different experiments, where 50, 100, 1000 and 2000 DU-145 cells and giant cells were suspended in diluted blood and processed by the two-outlet device at flow rates of sample/buffer of 100/1000 µL/min. The recovered outlet 2 fluid was then centrifuged, reduced to 1000 µL and run in the four-outlet device with flow rates of sample/buffer of 100/1000 µL/min. Results are described as Mean +SD of 3 independent experiments.

From all these results it is possible to conclude that the proposed microfluidic system – both devices in sequence – appears to be a viable choice for large, rare cancer cell separation. The efficiency of the interest output sample can be increased by processing it first in the two outlet-device at flow rates of 100/1000 µL/min, recovering the outlet 2 fluid, centrifuging and reducing it to 1000 µL, and then running it in the four-outlet device at flow rates of 100/1000 µL/min. With this strategy implemented, the desired cells were recovered and the contamination of the recovered samples with other blood cells was highly reduced. A final proof-of-concept experiment was then performed with this microfluidic system.

## 5.6 Proof-of-concept of the Microfluidic-based system

In order to determine if the proposed microfluidic system would perform well when using pathological samples of patients with prostate cancer, a different working fluid was tested. A new cell line was used, PC-3, as well as *in vitro* generated giant cells, were both suspended in diluted blood at a cell number of 100. The optimal flow rates were used and the outlets of the microfluidic system were evaluated by counting the cells collected in each outlet. This procedure correspond to the set of experiments C that was introduced in section “Microfluidic Setup and Experimental Tests”, chapter 4, and is represented in Figure 4.7.

When compared to the previously used DU-145 cells, the PC-3 cell line has characteristics more resemblant to the CTCs, mainly due to having larger diameters, and close cell deformability, and thus these cells will mimic perfectly the CTCs founded in the pathological samples [106]. As mentioned in section “Experimental Flow Rates Optimization”, chapter 5, the PC-3 cells diameter is  $22.1 \pm 5.0$  µm.

Considering the optimal flow rates of 100/1000  $\mu\text{L}/\text{min}$  for sample and buffer intake, respectively, and using a cell suspension analogous to the pathological samples, i.e. 100 PC-3 cells and 100 giant cells suspended in diluted whole blood, the sample was processed through the proposed microfluidic system.

Four independent experiments were performed, with the average recovery rate of PC-3 cells being 85.28%, while for the giant cells was 60.83% (Figure 5.12 (A)). From these results it is possible to conclude that the proposed microfluidic system is capable to achieve an efficient isolation of cells analogous to the ones found in pathological samples. Observing the cells isolation in each outlet of the four-outlet device (Figure 5.12 (B)), it was not possible to achieve a perfect separation between PC-3 and giant cells, contrary to what the numerical results suggested; however, the cell recover is high and in an almost pure sample.

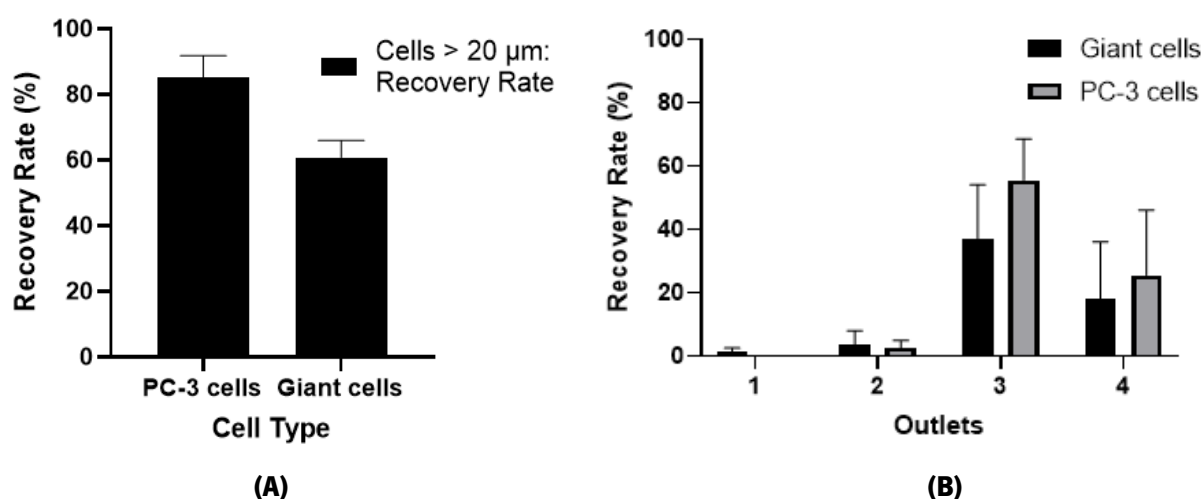


Figure 5.12 - Average recovery rate of cells > 20  $\mu\text{m}$  (A) and average recovery rate of PC-3 and giant cells per outlet of the four-outlet device (B) of four different experiments, where 100 cells of both PC-3 cells and giant cells were suspended in diluted blood and processed by the two-outlet device at flow rates of sample/buffer of 100/1000  $\mu\text{L}/\text{min}$ . The recovered outlet 2 fluid was then centrifuged, reduced to 1000  $\mu\text{L}$  and run in the four-outlet device with flow rates of sample/buffer of 100/1000  $\mu\text{L}/\text{min}$ . Results are described as Mean +SD of 3 independent experiments.

The numerical simulations results confirmed the ones obtained in the experimental procedures, as the experimental conditions were mimicked. However, the recovery rate obtained for both CTC-like particles and CAML-like particles was 100% (Figure 5.13), with the CAMLs being all collected in outlet 3, while all the CTCs were collected in outlet 4. Thus, the numerical models corroborate the efficient values obtained in the experimental procedures. The difference in the efficiency values obtained is attributed to the impossibility to recreate numerically cell-to-cell interactions, as well as to some small loss of interest cells that might have occurred in the centrifugation stage of the experimental methods.

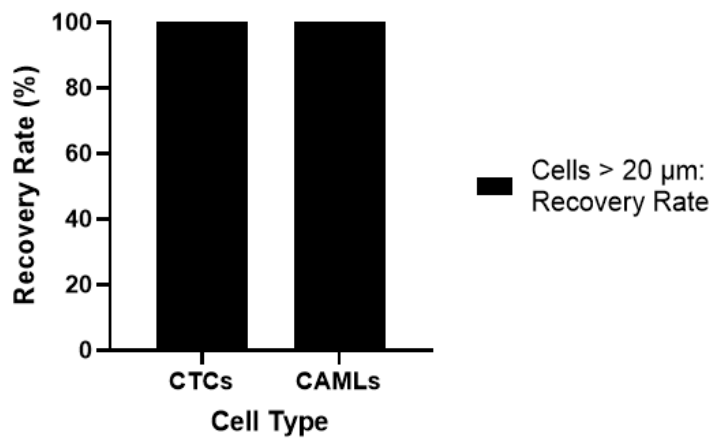


Figure 5.13 - Average recovery of cells  $> 20 \mu\text{m}$  obtained for the combination of the two-outlet device model with the four-outlet device model device at flow rates of 100/1000  $\mu\text{L}/\text{min}$  for the sample and buffer, respectively.

Thus, it is possible to conclude that the proposed microfluidic system composed of two DFF devices can be used for prostate cancer CTCs and CAMLs cells isolation, as a high recovery rate is achieved. Besides this, the numerical simulations demonstrated to be a useful tool in the development and optimization processes of the devices' geometries.

## 6. CONCLUSIONS AND FUTURE WORK

### 6.1 Conclusions

The work developed in this dissertation had the main purpose of microfabricating a microfluidic device for cell sorting capable of isolating both circulating tumour cells (CTCs) and giant cancer-associated macrophage-like cells (CAMLs). Such device would act as a non-invasive approach for detection, quantification and molecular profiling of circulating cancer-related cells, potentially enabling for earlier cancer detection and real-time patient monitoring.

These cell populations are rare in number ( $\sim 1$  to 10 CTCs and CAMLs/mL of whole blood), and are extremely difficult to isolate with efficiency and high yield by using conventional microfluidics approaches. Size-based inertial separation methods constitute an interesting approach, especially the Dean Flow Fractionation (DFF) configuration. This method allows for an efficient separation of the interest cells from the rest of the blood with high efficiency, sample throughput and high cell viability.

In this work, the DFF approach was adopted, with two inertial and size-based microfluidic devices for focusing and isolation of CTCs and CAMLs being developed. The devices geometries were defined in a way that the large cells are collected in the inner outlets of the devices, while the smaller ones, RBCs and WBCs are pushed to the outer outlets, as a consequence of the inertial forces in play. Both proposed devices are composed of two inlets, a channel depth of 170  $\mu\text{m}$  and have a size threshold for particle focusing of 20  $\mu\text{m}$ , with one of them having two outlets and the other four outlets. The devices geometries were developed using CAD models, being numerically optimized before the fabrication. The devices master moulds were obtained by photolithography technique, with PDMS being used for the fabrication of the microfluidic devices.

Both devices, two-outlet and four-outlet, were tested numerically and experimentally to assure their working principal. Numerically, it was determined that the optimal flow rates for the sample and buffer fluid were, respectively, either 100/1000  $\mu\text{L}/\text{min}$  or 200/800  $\mu\text{L}/\text{min}$  for the two-outlet device and 100/800  $\mu\text{L}/\text{min}$  for the four-outlet device. The optimal experimental isolation results were obtained using flow rates of 100 and 1000  $\mu\text{L}/\text{min}$  for the sample and buffer fluid, respectively, in both devices. The isolation efficiency of the two-outlet device for cells over 20  $\mu\text{m}$  is 92.80% and for the four-outlet device is 93.79%.

When the two devices were run in combination, with intermediate centrifugation, the results obtained experimentally revealed that, for the optimal flow rate ratio, recovery rate of the cells mimicking the CTCs is about 85.28% and for the cells mimicking the CAMLs is about 60.83%, with a high depletion

of non-interest cells also being achieved. The numerical simulations results corroborated the experimental tests. The different efficiency values obtained in the numerical and experimental procedures was attributed is attributed to the impossibility to recreate numerically cell-to-cell interactions, as well as to some the loss of interest cells that occurs in the centrifugation procedure of the experimental methods.

It is concluded that the developed devices and the microfluidic system proposed in this dissertation are viable of using in pathological samples of prostate cancer to isolate cancer-related cells, CTCs and CAMLs, for further downstream analysis and to obtain more insight about the pathology and its progression for metastatic stage.

## **6.2 Future Work**

Future research and work in this topic can be performed. As such, in order to optimize the proposed microfluidic system, the centrifugation procedure used to reduce the volume of the sample that will run in the in the four-outlet device, should be eliminated, and a more integrated system should be developed. There are two potential alternatives consisting in directly connect the interest outlet of the two-outlet device to the sample inlet of the four-outlet device using EVA tubing or by adopting a stacked configuration, in which the two-outlet device is stacked on top of the four-outlet device, with the interest outlet being connected to sample outlet of the second device. The last possibility would result in a considerable reduction of time necessary to perform the experimental runs, while also resulting in a more compact, and simple microfluidic system, especially if the stacked configuration is adopted.

Besides that, with the purpose of reducing RBCs contamination in the interest outlets, it should be investigated the viability of using lysed blood instead of diluted blood. This would result in a substantial decrease in the number of cells that are processed in the microfluidic system, which would cause a reduction in the cell-to-cell interactions that take place. As such, the focusing of interest cells would be less affected by interactions with the RBCs, and the recovered samples contamination would be reduced.

Lastly, for a final validation of the experimental results, the microfluidic system should be tested using pathological samples from prostate cancer

### REFERENCES

- [1] Z. T. F. Yu, K. M. Aw Yong, and J. Fu, "Microfluidic blood cell sorting: Now and beyond," *Small*, vol. 10, no. 9, Wiley-VCH Verlag, pp. 1687–1703, May 14, 2014. doi: 10.1002/smll.201302907.
- [2] A. Jemal, F. Bray, M. M. Center, J. Ferlay, E. Ward, and D. Forman, "Global cancer statistics," *CA: A Cancer Journal for Clinicians*, vol. 61, no. 2, pp. 69–90, Mar. 2011, doi: 10.3322/caac.20107.
- [3] M. C. S. Wong *et al.*, "Global Incidence and Mortality for Prostate Cancer: Analysis of Temporal Patterns and Trends in 36 Countries," *European Urology*, vol. 70, no. 5, pp. 862–874, Nov. 2016, doi: 10.1016/j.eururo.2016.05.043.
- [4] S. S. Malik, R. Batool, N. Masood, and A. Yasmin, "Risk factors for prostate cancer: A multifactorial case-control study," *Current Problems in Cancer*, vol. 42, no. 3, pp. 337–343, May 2018, doi: 10.1016/j.currprobcancer.2018.01.014.
- [5] P. H. Gann, A. Fought, R. Deaton, W. J. Catalona, and E. Vonesh, "Risk Factors for Prostate Cancer Detection After a Negative Biopsy: A Novel Multivariable Longitudinal Approach," *Journal of Clinical Oncology*, vol. 28, no. 10, pp. 1714–1720, Apr. 2010, doi: 10.1200/JCO.2008.20.3422.
- [6] S. Saini, "PSA and beyond: alternative prostate cancer biomarkers," *Cellular Oncology*, vol. 39, no. 2, pp. 97–106, Apr. 2016, doi: 10.1007/s13402-016-0268-6.
- [7] E. Diamond *et al.*, "Isolation and characterization of circulating tumor cells in prostate cancer," *Frontiers in Oncology*, vol. 2, 2012, doi: 10.3389/fonc.2012.00131.
- [8] H. Esmailsabzali, T. v. Beischlag, M. E. Cox, A. M. Parameswaran, and E. J. Park, "Detection and isolation of circulating tumor cells: Principles and methods," *Biotechnology Advances*, vol. 31, no. 7, pp. 1063–1084, Nov. 2013, doi: 10.1016/j.biotechadv.2013.08.016.
- [9] S. S. Ganguly, X. Li, and C. K. Miranti, "The Host Microenvironment Influences Prostate Cancer Invasion, Systemic Spread, Bone Colonization, and Osteoblastic Metastasis," *Frontiers in Oncology*, vol. 4, Dec. 2014, doi: 10.3389/fonc.2014.00364.

## References

---

- [10] L. Yu, S. R. Ng, Y. Xu, H. Dong, Y. J. Wang, and C. M. Li, "Advances of lab-on-a-chip in isolation, detection and post-processing of circulating tumour cells," *Lab on a Chip*, vol. 13, no. 16, p. 3163, 2013, doi: 10.1039/c3lc00052d.
- [11] H. Cho, J. Kim, H. Song, K. Y. Sohn, M. Jeon, and K.-H. Han, "Microfluidic technologies for circulating tumor cell isolation," *The Analyst*, vol. 143, no. 13, pp. 2936–2970, 2018, doi: 10.1039/C7AN01979C.
- [12] H. W. Hou *et al.*, "Isolation and retrieval of circulating tumor cells using centrifugal forces," *Scientific Reports*, vol. 3, no. 1, p. 1259, Dec. 2013, doi: 10.1038/srep01259.
- [13] H. Wu, J. Zhu, Y. Huang, D. Wu, and J. Sun, "Microfluidic-based single-cell study: Current status and future perspective," *Molecules*, vol. 23, no. 9. MDPI AG, Sep. 13, 2018. doi: 10.3390/molecules23092347.
- [14] R. Lima, T. Ishikawa, Y. Imai, and T. Yamaguchi, "Blood Flow Behavior in Microchannels: Past, Current and Future Trends," in *Single and Two-Phase Flows on Chemical and Biomedical Engineering*, R. Lima, T. Ishikawa, Y. Imai, and T. Yamaguchi, Eds. BENTHAM SCIENCE PUBLISHERS, 2012, pp. 513–547. doi: 10.2174/978160805295011201010513.
- [15] Z. Shen *et al.*, "Inversion of hematocrit partition at microfluidic bifurcations," *Microvascular Research*, vol. 105, pp. 40–46, May 2016, doi: 10.1016/j.mvr.2015.12.009.
- [16] W. F. Ganong, *Review of Medical Physiology*, 22nd ed. New York: Lange Medical Books/McGraw-Hill, 2005.
- [17] S. Tripathi, Y. V. B. Varun Kumar, A. Prabhakar, S. S. Joshi, and A. Agrawal, "Passive blood plasma separation at the microscale: A review of design principles and microdevices," *Journal of Micromechanics and Microengineering*, vol. 25, no. 8. Institute of Physics Publishing, Aug. 01, 2015. doi: 10.1088/0960-1317/25/8/083001.
- [18] K. Sriram, M. Intaglietta, and D. M. Tartakovsky, "Non-Newtonian Flow of Blood in Arterioles: Consequences for Wall Shear Stress Measurements," *Microcirculation*, vol. 21, no. 7, pp. 628–639, Oct. 2014, doi: 10.1111/micc.12141.
- [19] O. K. Baskurt and H. J. Meiselman, "Blood Rheology and Hemodynamics," *Seminars in Thrombosis and Hemostasis*, vol. 29, no. 5, pp. 435–450, 2003, doi: 10.1055/s-2003-44551.
- [20] L. Waite and J. Fine, *Applied Biofluid Mechanics*, 2nd ed. McGraw-Hill Education, 2017.



## References

---

- [21] D. A. Fedosov, B. Caswell, A. S. Popel, and G. E. Karniadakis, "Blood flow and cell-free layer in microvessels.," *Microcirculation (New York, N.Y. : 1994)*, vol. 17, no. 8, pp. 615–28, Nov. 2010, doi: 10.1111/j.1549-8719.2010.00056.x.
- [22] S.-H. Lim, W.-H. Kim, H. Lee, C.-Y. Lee, and C.-W. Park, "Flow Visualization of Blood Cell and Detection of Cell Depleted Layer Using a Confocal Laser Scanning Microscope," *Journal of the Korean Society of Visualization*, vol. 8, no. 1, pp. 46–52, Mar. 2010, doi: 10.5407/JKSV.2010.8.1.046.
- [23] A. R. Pries, T. W. Secomb, P. Gaehtgens, and J. F. Gross, "Blood flow in microvascular networks. Experiments and simulation.," *Circulation Research*, vol. 67, no. 4, pp. 826–834, Oct. 1990, doi: 10.1161/01.RES.67.4.826.
- [24] Y. Sugii, R. Okuda, K. Okamoto, and H. Madarame, "Velocity measurement of both red blood cells and plasma of *in vitro* blood flow using high-speed micro PIV technique," *Measurement Science and Technology*, vol. 16, no. 5, pp. 1126–1130, May 2005, doi: 10.1088/0957-0233/16/5/011.
- [25] H. L. Goldsmith and J. C. Marlow, "Flow behavior of erythrocytes. II. Particle motions in concentrated suspensions of ghost cells," *Journal of Colloid and Interface Science*, vol. 71, no. 2, pp. 383–407, Sep. 1979, doi: 10.1016/0021-9797(79)90248-0.
- [26] M. Cristofanilli *et al.*, "Circulating Tumor Cells, Disease Progression, and Survival in Metastatic Breast Cancer," *New England Journal of Medicine*, vol. 351, no. 8, pp. 781–791, Aug. 2004, doi: 10.1056/NEJMoa040766.
- [27] T. N. Seyfried and L. C. Huysentruyt, "On the origin of cancer metastasis.," *Critical reviews in oncogenesis*, vol. 18, no. 1–2, pp. 43–73, 2013, doi: 10.1615/critrevoncog.v18.i1-2.40.
- [28] A. Fabisiewicz and E. Grzybowska, "CTC clusters in cancer progression and metastasis," *Medical Oncology*, vol. 34, no. 1, p. 12, Jan. 2017, doi: 10.1007/s12032-016-0875-0.
- [29] T. Shibue and R. A. Weinberg, "Metastatic colonization: Settlement, adaptation and propagation of tumor cells in a foreign tissue environment," *Seminars in Cancer Biology*, vol. 21, no. 2, pp. 99–106, Apr. 2011, doi: 10.1016/j.semcancer.2010.12.003.
- [30] S.-H. Lu *et al.*, "Identifying cancer origin using circulating tumor cells," *Cancer Biology & Therapy*, vol. 17, no. 4, pp. 430–438, Apr. 2016, doi: 10.1080/15384047.2016.1141839.

## References

---

- [31] S. B. Coffelt, R. Hughes, and C. E. Lewis, "Tumor-associated macrophages: Effectors of angiogenesis and tumor progression," *Biochimica et Biophysica Acta (BBA) - Reviews on Cancer*, vol. 1796, no. 1, pp. 11–18, Aug. 2009, doi: 10.1016/j.bbcan.2009.02.004.
- [32] L. Yang and Y. Zhang, "Tumor-associated macrophages: from basic research to clinical application," *Journal of Hematology & Oncology*, vol. 10, no. 1, p. 58, Dec. 2017, doi: 10.1186/s13045-017-0430-2.
- [33] G. Solinas, G. Germano, A. Mantovani, and P. Allavena, "Tumor-associated macrophages (TAM) as major players of the cancer-related inflammation," *Journal of Leukocyte Biology*, vol. 86, no. 5, pp. 1065–1073, Nov. 2009, doi: 10.1189/jlb.0609385.
- [34] D. L. Adams *et al.*, "Circulating giant macrophages as a potential biomarker of solid tumors," *Proceedings of the National Academy of Sciences*, vol. 111, no. 9, pp. 3514–3519, Mar. 2014, doi: 10.1073/pnas.1320198111.
- [35] Z. Mu *et al.*, "Prognostic values of cancer associated macrophage-like cells (CAML) enumeration in metastatic breast cancer," *Breast Cancer Research and Treatment*, vol. 165, no. 3, pp. 733–741, Oct. 2017, doi: 10.1007/s10549-017-4372-8.
- [36] T. Chanmee, P. Ontong, K. Konno, and N. Itano, "Tumor-Associated Macrophages as Major Players in the Tumor Microenvironment," *Cancers*, vol. 6, no. 3, pp. 1670–1690, Aug. 2014, doi: 10.3390/cancers6031670.
- [37] D. L. Adams *et al.*, "Circulating Cancer-Associated Macrophage-Like Cells Differentiate Malignant Breast Cancer and Benign Breast Conditions," *Cancer Epidemiology Biomarkers & Prevention*, vol. 25, no. 7, pp. 1037–1042, Jul. 2016, doi: 10.1158/1055-9965.EPI-15-1221.
- [38] J. Mong and M.-H. Tan, "Size-Based Enrichment Technologies for Non-cancerous Tumor-Derived Cells in Blood," *Trends in Biotechnology*, vol. 36, no. 5, pp. 511–522, May 2018, doi: 10.1016/j.tibtech.2018.02.010.
- [39] K. Pantel, R. H. Brakenhoff, and B. Brandt, "Detection, clinical relevance and specific biological properties of disseminating tumour cells," *Nature Reviews Cancer*, vol. 8, no. 5, pp. 329–340, May 2008, doi: 10.1038/nrc2375.
- [40] M. E. brahimi Warkiani *et al.*, "Ultra-fast, label-free isolation of circulating tumor cells from blood using spiral microfluidics," *Nature protocols*, vol. 11, no. 1, pp. 134–148, Jan. 2016, doi: 10.1038/nprot.2016.003.

## References

---

- [41] N. Liu, C. Petchakup, H. M. Tay, K. H. H. Li, and H. W. Hou, "Spiral Inertial Microfluidics for Cell Separation and Biomedical Applications," 2019, pp. 99–150. doi: 10.1007/978-981-13-6229-3\_5.
- [42] G. Spizzo *et al.*, "High Ep-CAM Expression is Associated with Poor Prognosis in Node-positive Breast Cancer," *Breast Cancer Research and Treatment*, vol. 86, no. 3, pp. 207–213, Aug. 2004, doi: 10.1023/B:BREA.0000036787.59816.01.
- [43] C. v. Pecot *et al.*, "A Novel Platform for Detection of CK+ and CK– CTCs," *Cancer Discovery*, vol. 1, no. 7, pp. 580–586, Dec. 2011, doi: 10.1158/2159-8290.CD-11-0215.
- [44] H. K. Lin *et al.*, "Portable Filter-Based Microdevice for Detection and Characterization of Circulating Tumor Cells," *Clinical Cancer Research*, vol. 16, no. 20, pp. 5011–5018, Oct. 2010, doi: 10.1158/1078-0432.CCR-10-1105.
- [45] P. A. Theodoropoulos *et al.*, "Circulating tumor cells with a putative stem cell phenotype in peripheral blood of patients with breast cancer," *Cancer Letters*, vol. 288, no. 1, pp. 99–106, Feb. 2010, doi: 10.1016/j.canlet.2009.06.027.
- [46] B. Aktas, M. Tewes, T. Fehm, S. Hauch, R. Kimmig, and S. Kasimir-Bauer, "Stem cell and epithelial-mesenchymal transition markers are frequently overexpressed in circulating tumor cells of metastatic breast cancer patients," *Breast Cancer Research*, vol. 11, no. 4, p. R46, Aug. 2009, doi: 10.1186/bcr2333.
- [47] K.-A. Hyun, K. Kwon, H. Han, S.-I. Kim, and H.-I. Jung, "Microfluidic flow fractionation device for label-free isolation of circulating tumor cells (CTCs) from breast cancer patients," *Biosensors and Bioelectronics*, vol. 40, no. 1, pp. 206–212, Feb. 2013, doi: 10.1016/j.bios.2012.07.021.
- [48] S. J. Tan, R. L. Lakshmi, P. Chen, W.-T. Lim, L. Yobas, and C. T. Lim, "Versatile label free biochip for the detection of circulating tumor cells from peripheral blood in cancer patients," *Biosensors and Bioelectronics*, vol. 26, no. 4, pp. 1701–1705, Dec. 2010, doi: 10.1016/j.bios.2010.07.054.
- [49] M. E. Warkiani *et al.*, "Slanted spiral microfluidics for the ultra-fast, label-free isolation of circulating tumor cells," *Lab Chip*, vol. 14, no. 1, pp. 128–137, 2014, doi: 10.1039/C3LC50617G.
- [50] R. Gertler, R. Rosenberg, K. Fuehrer, M. Dahm, H. Nekarda, and J. R. Siewert, "Detection of Circulating Tumor Cells in Blood Using an Optimized Density Gradient Centrifugation," 2003, pp. 149–155. doi: 10.1007/978-3-642-59349-9\_13.

## References

---

- [51] S. C. Hur, N. K. Henderson-MacLennan, E. R. B. McCabe, and D. di Carlo, "Deformability-based cell classification and enrichment using inertial microfluidics," *Lab on a Chip*, vol. 11, no. 5, p. 912, 2011, doi: 10.1039/c0lc00595a.
- [52] H.-S. Moon *et al.*, "Continuous separation of breast cancer cells from blood samples using multi-orifice flow fractionation (MOFF) and dielectrophoresis (DEP)," *Lab on a Chip*, vol. 11, no. 6, p. 1118, 2011, doi: 10.1039/c0lc00345j.
- [53] S.-B. Huang *et al.*, "High-purity and label-free isolation of circulating tumor cells (CTCs) in a microfluidic platform by using optically-induced-dielectrophoretic (ODEP) force," *Lab on a Chip*, vol. 13, no. 7, p. 1371, 2013, doi: 10.1039/c3lc41256c.
- [54] I. Cima *et al.*, "Label-free isolation of circulating tumor cells in microfluidic devices: Current research and perspectives.," *Biomicrofluidics*, vol. 7, no. 1, p. 11810, 2013, doi: 10.1063/1.4780062.
- [55] A. van de Stolpe, K. Pantel, S. Sleijfer, L. W. Terstappen, and J. M. J. den Toonder, "Circulating Tumor Cell Isolation and Diagnostics: Toward Routine Clinical Use: Figure 1.," *Cancer Research*, vol. 71, no. 18, pp. 5955–5960, Sep. 2011, doi: 10.1158/0008-5472.CAN-11-1254.
- [56] G. M. Whitesides, "The origins and the future of microfluidics," *Nature*, vol. 442, no. 7101, pp. 368–373, Jul. 2006, doi: 10.1038/nature05058.
- [57] A. Manz, N. Graber, and H. M. Widmer, "Miniaturized total chemical analysis systems: A novel concept for chemical sensing," *Sensors and Actuators B: Chemical*, vol. 1, no. 1–6, pp. 244–248, Jan. 1990, doi: 10.1016/0925-4005(90)80209-I.
- [58] T. M. Squires and S. R. Quake, "Microfluidics: Fluid physics at the nanoliter scale," *Reviews of Modern Physics*, vol. 77, no. 3, pp. 977–1026, Oct. 2005, doi: 10.1103/RevModPhys.77.977.
- [59] E. K. Sackmann, A. L. Fulton, and D. J. Beebe, "The present and future role of microfluidics in biomedical research," *Nature*, vol. 507, no. 7491, pp. 181–189, Mar. 2014, doi: 10.1038/nature13118.
- [60] D. di Carlo, D. Irimia, R. G. Tompkins, and M. Toner, "Continuous inertial focusing, ordering, and separation of particles in microchannels," *Proceedings of the National Academy of Sciences*, vol. 104, no. 48, pp. 18892–18897, Nov. 2007, doi: 10.1073/pnas.0704958104.

## References

---

- [61] A. A. S. Bhagat, H. W. Hou, L. D. Li, C. T. Lim, and J. Han, "Pinched flow coupled shear-modulated inertial microfluidics for high-throughput rare blood cell separation," *Lab on a Chip*, vol. 11, no. 11, p. 1870, 2011, doi: 10.1039/c0lc00633e.
- [62] H. W. Hou, A. A. S. Bhagat, W. C. Lee, S. Huang, J. Han, and C. T. Lim, "Microfluidic Devices for Blood Fractionation," *Micromachines*, vol. 2, no. 3, pp. 319–343, Jul. 2011, doi: 10.3390/mi2030319.
- [63] A. P. Sudarsan and V. M. Ugaz, "Fluid mixing in planar spiral microchannels," *Lab Chip*, vol. 6, no. 1, pp. 74–82, 2006, doi: 10.1039/B511524H.
- [64] J. Wang, Y. Zhan, V. M. Ugaz, and C. Lu, "Vortex-assisted DNA delivery," *Lab on a Chip*, vol. 10, no. 16, p. 2057, 2010, doi: 10.1039/c004472e.
- [65] D. C. Yeo, C. Wiraja, Y. Zhou, H. M. Tay, C. Xu, and H. W. Hou, "Interference-free Micro/nanoparticle Cell Engineering by Use of High-Throughput Microfluidic Separation," *ACS Applied Materials & Interfaces*, vol. 7, no. 37, pp. 20855–20864, Sep. 2015, doi: 10.1021/acsami.5b06167.
- [66] C. M. Birch, H. W. Hou, J. Han, and J. C. Niles, "Identification of malaria parasite-infected red blood cell surface aptamers by inertial microfluidic SELEX (I-SELEX)," *Scientific Reports*, vol. 5, no. 1, p. 11347, Sep. 2015, doi: 10.1038/srep11347.
- [67] N. Aceto *et al.*, "Circulating Tumor Cell Clusters Are Oligoclonal Precursors of Breast Cancer Metastasis," *Cell*, vol. 158, no. 5, pp. 1110–1122, Aug. 2014, doi: 10.1016/j.cell.2014.07.013.
- [68] B. L. Khoo *et al.*, "Ultra-High Throughput Enrichment of Viable Circulating Tumor Cells," 2014, pp. 1–4. doi: 10.1007/978-3-319-02913-9\_1.
- [69] S.-E. Ong, "Fundamental principles and applications of microfluidic systems," *Frontiers in Bioscience*, vol. 13, no. 13, p. 2757, 2008, doi: 10.2741/2883.
- [70] K. B. Chandran, S. E. Rittgers, and A. P. Yoganathan, *Biofluid Mechanics*. CRC Press, 2006. doi: 10.1201/9781420007213.
- [71] N. Convery and N. Gadegaard, "30 years of microfluidics," *Micro and Nano Engineering*, vol. 2. Elsevier B.V., pp. 76–91, Mar. 01, 2019. doi: 10.1016/j.mne.2019.01.003.
- [72] K. Avila, D. Moxey, A. de Lozar, M. Avila, D. Barkley, and B. Hof, "The Onset of Turbulence in Pipe Flow," *Science*, vol. 333, no. 6039, pp. 192–196, Jul. 2011, doi: 10.1126/science.1203223.

## References

---

- [73] D. di Carlo, "Inertial microfluidics," *Lab on a Chip*, vol. 9, no. 21, p. 3038, 2009, doi: 10.1039/b912547g.
- [74] J. Seo, M. H. Lean, and A. Kole, "Membrane-free microfiltration by asymmetric inertial migration," *Applied Physics Letters*, vol. 91, no. 3, p. 033901, Jul. 2007, doi: 10.1063/1.2756272.
- [75] S. S. Kuntaegowdanahalli, A. A. S. Bhagat, G. Kumar, and I. Papautsky, "Inertial microfluidics for continuous particle separation in spiral microchannels," *Lab on a Chip*, vol. 9, no. 20, p. 2973, 2009, doi: 10.1039/b908271a.
- [76] E. S. ASMOLOV, "The inertial lift on a spherical particle in a plane Poiseuille flow at large channel Reynolds number," *Journal of Fluid Mechanics*, vol. 381, pp. 63–87, Feb. 1999, doi: 10.1017/S0022112098003474.
- [77] D. di Carlo, J. F. Edd, K. J. Humphry, H. A. Stone, and M. Toner, "Particle Segregation and Dynamics in Confined Flows," *Physical Review Letters*, vol. 102, no. 9, p. 094503, Mar. 2009, doi: 10.1103/PhysRevLett.102.094503.
- [78] W. R. Dean, "Fluid motion in a curved channel," *Philos Mag*, vol. 121, no. 787, pp. 673–695, Nov. 1928, doi: 10.1098/rspa.1928.0205.
- [79] J. M. Martel and M. Toner, "Inertial Focusing in Microfluidics," *Annual Review of Biomedical Engineering*, vol. 16, no. 1, pp. 371–396, Jul. 2014, doi: 10.1146/annurev-bioeng-121813-120704.
- [80] D. R. Gossett and D. di Carlo, "Particle Focusing Mechanisms in Curving Confined Flows," *Analytical Chemistry*, vol. 81, no. 20, pp. 8459–8465, Oct. 2009, doi: 10.1021/ac901306y.
- [81] J. Sun *et al.*, "Nanofiller Reinforced Biodegradable PLA/PHA Composites: Current Status and Future Trends," *Polymers*, vol. 10, no. 5, p. 505, May 2018, doi: 10.3390/polym10050505.
- [82] K. Ren, J. Zhou, and H. Wu, "Materials for Microfluidic Chip Fabrication," *Accounts of Chemical Research*, vol. 46, no. 11, pp. 2396–2406, Nov. 2013, doi: 10.1021/ar300314s.
- [83] H. Becker, "Polymer microfluidic devices," *Talanta*, vol. 56, no. 2, pp. 267–287, Feb. 2002, doi: 10.1016/S0039-9140(01)00594-X.

- [84] J. C. McDonald *et al.*, "Fabrication of microfluidic systems in poly(dimethylsiloxane)," *Electrophoresis*, vol. 21, no. 1, pp. 27–40, Jan. 2000, doi: 10.1002/(SICI)1522-2683(20000101)21:1<27::AID-ELPS27>3.0.CO;2-C.
- [85] H. Fallahi, J. Zhang, H. P. Phan, and N. T. Nguyen, "Flexible microfluidics: Fundamentals, recent developments, and applications," *Micromachines*, vol. 10, no. 12, MDPI AG, Dec. 01, 2019. doi: 10.3390/mi10120830.
- [86] S. J. Clarson, K. Dodgson, and J. A. Semlyen, "Studies of cyclic and linear poly(dimethylsiloxanes): 19. Glass transition temperatures and crystallization behaviour," *Polymer*, vol. 26, no. 6, pp. 930–934, Jun. 1985, doi: 10.1016/0032-3861(85)90140-5.
- [87] J. C. Lötters, W. Olthuis, P. H. Veltink, and P. Bergveld, "The mechanical properties of the rubber elastic polymer polydimethylsiloxane for sensor applications," *Journal of Micromechanics and Microengineering*, vol. 7, no. 3, pp. 145–147, Sep. 1997, doi: 10.1088/0960-1317/7/3/017.
- [88] M. Abkarian, M. Faivre, R. Horton, K. Smistrup, C. A. Best-Popescu, and H. A. Stone, "Cellular-scale hydrodynamics," *Biomedical Materials*, vol. 3, no. 3, p. 034011, Sep. 2008, doi: 10.1088/1748-6041/3/3/034011.
- [89] D. Bento *et al.*, "Deformation of Red Blood Cells, Air Bubbles, and Droplets in Microfluidic Devices: Flow Visualizations and Measurements," *Micromachines*, vol. 9, no. 4, p. 151, Mar. 2018, doi: 10.3390/mi9040151.
- [90] S. O. Catarino, R. O. Rodrigues, D. Pinho, J. M. Miranda, G. Minas, and R. Lima, "Blood Cells Separation and Sorting Techniques of Passive Microfluidic Devices: From Fabrication to Applications," *Micromachines*, vol. 10, no. 9, p. 593, Sep. 2019, doi: 10.3390/mi10090593.
- [91] A. Lamberti, S. L. Marasso, and M. Cocuzza, "PDMS membranes with tunable gas permeability for microfluidic applications," *RSC Adv.*, vol. 4, no. 106, pp. 61415–61419, 2014, doi: 10.1039/C4RA12934B.
- [92] B.-H. Ryu and D.-E. Kim, "Development of highly durable and low friction micro-structured PDMS coating based on bio-inspired surface design," *CIRP Annals*, vol. 64, no. 1, pp. 519–522, 2015, doi: 10.1016/j.cirp.2015.03.004.

## References

---

- [93] M. A. Unger, H.-P. Chou, T. Thorsen, A. Scherer, and S. R. Quake, "Monolithic Microfabricated Valves and Pumps by Multilayer Soft Lithography," *Science*, vol. 288, no. 5463, pp. 113–116, Apr. 2000, doi: 10.1126/science.288.5463.113.
- [94] E. Sollier, C. Murray, P. Maoddi, and D. di Carlo, "Rapid prototyping polymers for microfluidic devices and high pressure injections," *Lab on a Chip*, vol. 11, no. 22, p. 3752, 2011, doi: 10.1039/c1lc20514e.
- [95] X. Zhang and S. J. Haswell, "Materials Matter in Microfluidic Devices," *MRS Bulletin*, vol. 31, no. 2, pp. 95–99, Feb. 2006, doi: 10.1557/mrs2006.22.
- [96] G. S. Fiorini and D. T. Chiu, "Disposable microfluidic devices: fabrication, function, and application," *BioTechniques*, vol. 38, no. 3, pp. 429–446, Mar. 2005, doi: 10.2144/05383RV02.
- [97] A. del Campo and C. Greiner, "SU-8: a photoresist for high-aspect-ratio and 3D submicron lithography," *Journal of Micromechanics and Microengineering*, vol. 17, no. 6, pp. R81–R95, Jun. 2007, doi: 10.1088/0960-1317/17/6/R01.
- [98] A. J. Dy, A. Cosmanescu, J. Sluka, J. A. Glazier, D. Stupack, and D. Amarie, "Fabricating microfluidic valve master molds in SU-8 photoresist," *Journal of Micromechanics and Microengineering*, vol. 24, no. 5, p. 057001, May 2014, doi: 10.1088/0960-1317/24/5/057001.
- [99] V. Faustino, S. O. Catarino, R. Lima, and G. Minas, "Biomedical microfluidic devices by using low-cost fabrication techniques: A review," *Journal of Biomechanics*, vol. 49, no. 11, pp. 2280–2292, Jul. 2016, doi: 10.1016/j.jbiomech.2015.11.031.
- [100] S. Metz, S. Jiguet, A. Bertsch, and Ph. Renaud, "Polyimide and SU-8 microfluidic devices manufactured by heat-depolymerizable sacrificial material technique," *Lab on a Chip*, vol. 4, no. 2, p. 114, 2004, doi: 10.1039/b310866j.
- [101] H. Sato, H. Matsumura, S. Keino, and S. Shoji, "An all SU-8 microfluidic chip with built-in 3D fine microstructures," *Journal of Micromechanics and Microengineering*, vol. 16, no. 11, pp. 2318–2322, Nov. 2006, doi: 10.1088/0960-1317/16/11/010.
- [102] P. Abgrall, C. Lattes, V. Conédéra, X. Dollat, S. Colin, and A. M. Gué, "A novel fabrication method of flexible and monolithic 3D microfluidic structures using lamination of SU-8 films," *Journal of Micromechanics and Microengineering*, vol. 16, no. 1, pp. 113–121, Jan. 2006, doi: 10.1088/0960-1317/16/1/016.



## References

---

- [103] L. Xiong, P. Chen, and Q. Zhou, "Adhesion promotion between PDMS and glass by oxygen plasma pre-treatment," *Journal of Adhesion Science and Technology*, vol. 28, no. 11, pp. 1046–1054, Jun. 2014, doi: 10.1080/01694243.2014.883774.
- [104] F. Katzenberg, "Plasma-bonding of poly(dimethylsiloxane) to glass," *e-Polymers*, vol. 5, no. 1, Dec. 2005, doi: 10.1515/epoly.2005.5.1.638.
- [105] H. W. Hou *et al.*, "Rapid and label-free microfluidic neutrophil purification and phenotyping in diabetes mellitus," *Scientific Reports*, vol. 6, no. 1, p. 29410, Sep. 2016, doi: 10.1038/srep29410.
- [106] J. M. Hope *et al.*, "Circulating prostate cancer cells have differential resistance to fluid shear stress-induced cell death," *Journal of Cell Science*, vol. 134, no. 4, Feb. 2021, doi: 10.1242/jcs.251470.

## **APPENDIX A - PUBLICATIONS**

### Poster

Dias L., Lima R., Pinho D., 2021. Inertial and size based focusing of cancer related blood cells in a 4-outlet spiral microchannel: numerical approach. Euro NanoForum2021;

### Abstract

Dias L., Lima R., Pinho D., 2021. Inertial and size based focusing of cancer related blood cells in a 4-outlet spiral microchannel: numerical approach. Euro NanoForum2021.

### Oral Presentation

Dias L., Pinho D., Freitas P., 2020. Rare Cancer-Related Cells Isolation From Blood, INL Annual Research Symposium, November 24-27.

# APPENDIX B – POSTER SUBMITTED TO THE EURONANOFORM2021, 5-6 MAY 2021, BRAGA, PORTUGAL

## INERTIAL AND SIZE BASED FOCUSING OF CANCER RELATED BLOOD CELLS IN A 4-OUTLET SPIRAL MICROCHANNEL: NUMERICAL APPROACH



Luís Dias<sup>1</sup>, Rui Lima<sup>2</sup>, and Diana Pinho<sup>1</sup>

<sup>1</sup> INL - International Iberian Nanotechnology Laboratory, Av. Mestre José Veiga, Braga 4715-330, Portugal

<sup>2</sup> MERICs, Mechanical Engineering Department, University of Minho, Campus de Azurém, Guimarães 4800-058, Portugal



### Introduction

- With the goal of contributing to the development of a novel microfluidic system with high sensitivity for analysis of blood cancer clinical samples, an innovative inertial and size-based device for prostate cancer screening was designed.
- By using microfluidic devices based in passive methods (inertial and size based) to isolate the cancer-related cells, it is expected that Circulating Tumor Cells (CTCs) and Cancer-associated Macrophage-like Cells (CAMLs) [1] can be separated from the rest of the blood.
- A label-free isolation [2] method was chosen, as it allows an efficient inertial focusing of cells with high throughputs, while also make possible further isolated cell analysis.
- A device with spiral-shaped channel was designed, having 2 inlets (for sample and buffer inflow) and 4 outlets.
- The cells of interest cells, with a length of over 20 μm (CTCs and CAMLs) are captured in the inner outlets and separated from the other cells (e.g. Red Blood Cells, White Blood Cells).
- This system is being tested and validated by performing numerical simulations and experimental tests.

### Material and Methods

#### Microchannel geometry and Working principal

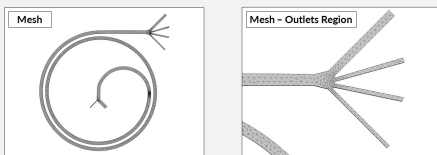
The working principle behind the spiral device is based on the action of inertial forces (the Lift and the Dean drag forces) on the particles that flow through the device.

When both of these forces reach an equilibrium, the smaller cells (> 20 μm) will be focused near the outer wall, exiting via the outer outlets (1 and 2), while the larger ones (< 20 μm) align close to the inner wall and exit via the inner outlets (3 and 4), and thus a size-based separation takes place.



#### Numerical approach

Prior to the experimental approaches, 3D models of the spiral device were created using COMSOL software and optimal working conditions (device geometry, flow rates and fluid viscosities) were computed, in order to achieve high isolation efficiency of particles (or cells).



#### Steady Incompressible Navier-Stokes Equations

$$\rho(\mathbf{u} \cdot \nabla \mathbf{u}) = -\nabla p + \mu \nabla^2 \cdot (\nabla \mathbf{u} + (\nabla \mathbf{u})^T)$$

$$\nabla \cdot \mathbf{u} = 0$$

#### Dean Drag Force Equation

$$F_D = 3\pi\mu U_{Dean} a_c$$

#### Inertial Lift Force Equation

$$F_L = C_L \rho G^2 a_c^3$$

#### Particles Properties

	RBCs	WBCs	CTCs	CAMLs	Total
N° of Cells @ Inlet	30	12	4	4	50
Cell Size (μm)	8	12	20	35	-

#### Discretization of fluids:

- A P3+P3 discretization was chosen (3<sup>rd</sup> order elements for the velocity components and 3<sup>rd</sup> order elements for the pressure field), as it allowed to obtain more accurate results, namely in what regards to the particles trajectories.

#### Mesh properties:

- Number of elements: 17289;
- Maximum element size: 236 μm;
- Maximum element size: 70.9 μm.

The mesh element size is based in the Coarser settings, due to the computational efforts.

#### Fluid flow dynamics physics:

- laminar flow solving;
- no slip wall condition;
- two inlets with different velocities (the sample and buffer) and four outlets.

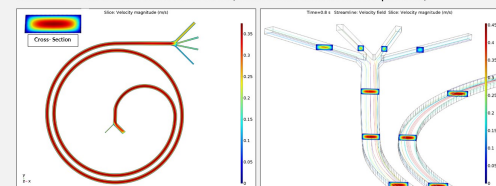
#### Particles tracing module:

- A Dean Drag Force ( $F_D$ );
- Two wall induced forces (one that acts on the sidewalls and other that acts on the upper and lower walls) - Lift Force ( $F_L$ ).

### Results and Discussion

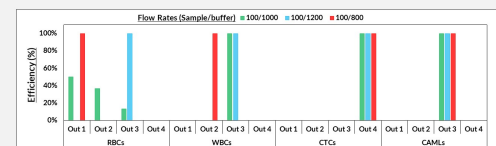
#### Velocity fields

The velocity fields that are present in the device's channels were computed, which is a fundamental step in order to determine the particles behavior and trajectories. The flow rates tested were 100/1000, 100/1200 and 100/800 μL/min,



#### Particles Separation

After having the laminar flow and the velocity field determined, the particles migrations can be computed. The particles trajectories, including understanding in which outlet it ends up, were determined and the efficiency was calculated.



The best results were obtained for the flow rates 100 and 800 μL/min (sample and sheath buffer inflow, respectively), as numerical data shows that the mean isolation efficiency of particles over 20 μm is above 90% under this conditions, with the CTCs and CAMLs being entirely separated from the other particles as they exit through the inner outlets (3 and 4). By looking at the particle trajectories images below, it can be observed that over the course of the channel the interest cells (green and red) get closer to the inner wall, as a result of the drag forces action, while the RBCs and WBCs (in blue) stay in the middle of the channel, or even closer to the outer wall, which in the end means that it exits through the non-interest outlets (1 and 2).

S - 100 μL/min B - 800 μL/min	RBCs		WBCs		CTCs		CAMLs		Total	
	N° Cells	Efficiency	N° Cells	Efficiency	N° Cells	Efficiency	N° Cells	Efficiency	N° Cells	Purity
Outlet 1	30	100%	0	-	0	-	0	-	30	0
Outlet 2	0	-	12	100%	0	-	0	-	12	0
Outlet 3	0	-	0	-	0	-	4	100%	4	100%
Outlet 4	0	-	0	-	4	100%	0	-	4	100%



### References

- [1] Adams, D.L., et al. Proceedings of the National Academy of Sciences 2014, 111, 3514-3519.
- [2] Rzhetsky, A. S., et al. Cancers 2020, 12(1): 81.

### Acknowledgements

The authors would like to thank the funding source for this research through the project POCI-01-0145-FEDER-031442, funded by Fundação para a Ciência e Tecnologia (FCT) and ERDF.



### Conclusions and Future Work

- In this work, we have developed an inertial and size-based device for prostate cancer screening. The results are very promising, especially the numerical ones.
- The best flow rates are 100 and 800 μL/min (sample and sheath buffer inflow respectively), with an efficiency above 90% and a total isolation by size, as the CTCs flow separately to the device's outlet 4 and the CAMLs follow isolated to the outlet 3.
- Experimental essays with spiked cancer cells in blood samples are currently ongoing in order to corroborate the numerical data.

**Inertial and size-based focusing of cancer-related blood cells in a 4-outlet  
spiral microchannel: numerical approach**

Luís Dias<sup>a</sup>, Rui Lima<sup>b</sup>, and Diana Pinho<sup>a</sup>

<sup>b</sup>*INL-International Iberian Nanotechnology Laboratory*

*Av. Mestre José Veiga, Braga 4715-330, Portugal*

<sup>b</sup>*MEtRICs, Mechanical Engineering Department*

*University of Minho, Campus de Azurém, Guimarães 4800-058, Portugal*

[a78689@alunos.uminho.pt](mailto:a78689@alunos.uminho.pt)

With the goal of contributing to the development of a novel microfluidic system with high sensitivity for analysis of blood cancer clinical samples, an innovative inertial and size-based device for prostate cancer screening was designed. It is expected that by using microfluidic devices based in passive methods (inertial and size based), to isolate the cancer-related cells, circulating tumour cells (CTCs) and cancer-associated macrophage-like cells (CAMLs)<sup>[1]</sup>, they can be separated from the rest of the blood. Thus, a label-free isolation<sup>[2]</sup> device with spiral-shaped and 4 outlets was designed. Prior to experimental approaches, 3D models of the spiral device were created in the COMSOL software and optimal working conditions - such as device geometry, flow rates and fluid viscosities - were computed, in order to achieved high isolation efficiency of particles (or cells). With the numerical approach, it is possible to determine the velocity fields in the device, as well as to trace the particle movement, including in which outlet it ends up. The best working flow rates obtained were 100  $\mu\text{L}/\text{min}$  and 1000  $\mu\text{L}/\text{min}$  for sample and sheath buffer inflow, respectively. Numerical data shows that the mean isolation efficiency of particles over 20  $\mu\text{m}$  is above 90%. Experimental assays with spiked cancer cells in blood samples are currently ongoing in order to corroborate the numerical data.

[1] Adams, D.L., et al. Proceedings of the National Academy of Sciences **2014**, 111, 3514-3519.

[2] Rzhavskiy, A. S., et al. Cancers **2020**, 12(1): 81.

**Acknowledgements**

The authors would like to thank the funding source for this research trough the project POCI-01-0145-FEDER-031442, funded by Fundação para a Ciência e Tecnologia (FCT) and ERDF.